12-15-2016

A Proposed Imaging System to Spatially and Temporally Monitor Unburned Hydrocarbons in Jet Engine Exhaust

Emily E. Berkson
eeb8871@rit.edu

A Proposed Imaging System to Spatially and Temporally Monitor Unburned Hydrocarbons in Jet Engine Exhaust

by

Emily E. Berkson

B.S. University of Arizona, 2013

A thesis submitted in partial fulfillment of the
requirements for the degree of Master of Science
in the Chester F. Carlson Center for Imaging Science
College of Science
Rochester Institute of Technology

December 15, 2016

Signature of the Author _____

Accepted by _____
Dr. Charles Bachmann, Coordinator, M.S. Degree Program

CHESTER F. CARLSON CENTER FOR IMAGING SCIENCE
COLLEGE OF SCIENCE
ROCHESTER INSTITUTE OF TECHNOLOGY
ROCHESTER, NEW YORK

CERTIFICATE OF APPROVAL

M.S. DEGREE THESIS

The M.S. Degree Thesis of Emily E. Berkson
has been examined and approved by the
thesis committee as satisfactory for the
thesis required for the
M.S. degree in Imaging Science

Dr. David W. Messinger, Thesis Advisor

Dr. Emmett Ientilucci

Dr. Carl Salvaggio

Date

A Proposed Imaging System to Spatially and Temporally Monitor Unburned Hydrocarbons in Jet Engine Exhaust

by

Emily E. Berkson

Submitted to the
Chester F. Carlson Center for Imaging Science
in partial fulfillment of the requirements
for the Master of Science Degree
at the Rochester Institute of Technology

Abstract

The local air quality surrounding airports is significantly impacted by ground-based airplane operations, such as landing, taxiing, idling, and takeoff. In recent years, studies performed across the country revealed that people living near major airports suffer from increased cancer risks and higher likelihoods of developing respiratory issues. Jet engine emissions have been monitored extensively by direct probing of the exhaust, but there are currently no inexpensive, portable, and unobtrusive methods with which to study exhaust plume dynamics. This study assesses the feasibility of designing a multispectral imaging system to track the spatial-temporal nature of a jet engine plume. Ideally, the imaging system will be both inexpensive and portable enough to be deployed at any airport. We begin by characterizing the phenomenology of jet engine emissions during ground operations and select unburned hydrocarbons (UHCs) as the basis for our plume tracking. A proposed LWIR imaging system layout and radiometric governing equation is developed to predict the camera's sensor-reaching radiance. We use two methods, the Ideal Gas Law and the Gaussian Plume Equation, to three-dimensionally model the UHC concentration within the plume, which, in turn, is used to predict the plume transmission as a function of downwind distance. Radiometric models are used to predict the sensor-reaching radiance of the camera, and two filter combinations are selected to maximize the plume detectability. Each filter combination uses one filter to monitor the background radiance and one filter to trace the plume radiance. They are located at located at 9.001/9.333 [μm] and 9.12/12.212

[μm]. The plume tracing filters are used to assess plume detectability, and we find that that a camera with an NEΔT of 0.05 [K] will be able to detect the plume up to 120 seconds after the engine has passed. We conclude by predicting what filter difference the camera will observe temporally, as plumes are continuously generated and dissipated. The effect of individual UHCs on total plume transmission was also examined, and a selection of narrowband filters for monitoring specific UHCs is proposed for future work. Results will help to prototype a system for deployment at the Greater Rochester International Airport. This work will make airport emissions inventories more accessible and allow for improved governing of emission caps and pollution bylaws.

Acknowledgements

- To my advisor, Dr. David W. Messinger, thank you for welcoming me to the department, taking me on as a student, and allowing me to work multiple internships during my time here. I would also like to express my amazement that despite being busy with a million and one director duties, you always knew exactly what stage my thesis was at and where we left off (even after I returned from three-month internships). Finally, I would like to extend my thanks to you for allowing me to travel and attend multiple conferences through the course of my degree.

- To my committee member, Dr. Emmett J. Ientilucci, thank you for spending an entire semester teaching me the necessary radiometry to complete this work, and for making yourself available for in-depth discussions whenever I had questions or confusion.

- To my committee member, Dr. Carl Salvaggio, thank you for welcoming me to the department as a Teaching Assistant back in Fall of 2014, teaching me Image Processing, and giving me an excuse to learn Python. I am also grateful to have given my both my first and last major presentations with you on my team.

- To my parents, thank you. From moving me around the country multiple times, coming to visit me in faraway places, proofreading numerous papers and projects, and being a constant source of encouragement, you have been here for me every step of the way. To mimic the sentiment from another CIS graduate thesis, it is nice that you also think I am pretty smart for making this.

- To my brother, thank you. Even though far away, you have supported me several times in this endeavor. Most notably, you were kind enough to create some of the figures in this thesis and in my defense presentation.

- To Anton, thank you for being a calming presence when I am panicking, and for asking the questions regarding my research that I had yet to think of. Thank you for making me laugh, and for the adventures we have shared.

- Last but not least, thank you to my classmates, past and present. To the classmates who helped me understand Fourier, introduced me to new board games, brought me to new restaurants in Rochester, and acted as a sounding board for my defense work, I am deeply grateful.

Contents

Forward **i**
Declaration . . . i
Approval . . . ii
Abstract . . . iv
Acknowledgements . . . vi
Table of Contents . . . viii
List of Figures . . . x
List of Tables . . . xi
Glossaries . . . xi
List of Acronyms . . . xi
List of Institutions . . . xiii
List of Symbols . . . xiv

1 Introduction **1**
1.1 Problem Statement and Objectives . . . 3
1.2 Layout . . . 3

2 Background **5**
2.1 Jet Engine Emissions . . . 5
2.1.1 Landing-Takeoff Cycle . . . 5
2.1.2 Emissions Inventory . . . 6
2.1.3 Monitored Pollutants . . . 7
2.1.4 Unburned Hydrocarbons . . . 9
2.2 Methods of Monitoring Exhaust Plumes . . . 11
2.2.1 Direct Probing . . . 11
2.2.2 Fourier Transform Infrared Spectroscopy . . . 12
2.2.3 Multispectral Imaging . . . 13

3 Literature Review **14**
3.1 1980s – 1990s Work on Monitoring UHCs . . . 14
3.2 UHC Studies of the 2000s . . . 15
3.2.1 NASA EXCAVATE Campaign . . . 17
3.2.2 NASA APEX Campaign . . . 18
3.2.3 Airport Cooperative Research Program Report 7 . . . 21
3.3 Recent Work Monitoring UHC Emissions . . . 23
3.4 Gas Detection with Multispectral Imaging . . . 24

4 Proposed Imaging System **26**
4.1 Gaseous Effluent Model . . . 26
4.2 Imaging System Design . . . 29
4.3 System Governing Equation . . . 30

5 Pollutant Phenomenology **34**

6 Concentration Modeling Methods **48**
6.1 Ideal Gas Law . . . 48
6.2 Gaussian Plume Model . . . 53

7 Results **61**
7.1 Concentration Model . . . 61
7.2 Plume Transmission . . . 65
7.3 Non-Plume Parameters . . . 68
7.4 Plume Radiance and Filter Selection . . . 72
7.5 Temporal Modeling . . . 81

8 Future Work Outlook **85**
8.1 Observations to Information . . . 85
8.2 Tracking Individual Hydrocarbons . . . 88
8.3 System Design Modifications . . . 93

9 Conclusions **94**

Bibliography **97**

List of Figures

2.1 Landing Takeoff Cycle . . . 6
2.2 Emission Indices vs. Engine Thrust . . . 10

4.1 Gaseous Effluent Model . . . 27
4.2 Proposed Imaging System Design . . . 31

5.1 Carbon Monoxide Absorption Spectrum . . . 36
5.2 Carbon Dioxide Absorption Spectrum . . . 36
5.3 Nitrous Oxide Absorption Spectrum . . . 37
5.4 Nitrogen Dioxide Absorption Spectrum . . . 37
5.5 Formaldehyde Absorption Spectrum . . . 38
5.6 Acetaldehyde Absorption Spectrum . . . 39
5.7 Ethylene Absorption Spectrum . . . 39
5.8 Propene Absorption Spectrum . . . 40
5.9 Butene-1 Absorption Spectrum . . . 40
5.10 Butene-2 Absorption Spectrum . . . 41
5.11 Acrolein Absorption Spectrum . . . 41
5.12 Pentene Absorption Spectrum . . . 42
5.13 Benzene Absorption Spectrum . . . 42
5.14 Toluene Absorption Spectrum . . . 43
5.15 Styrene Absorption Spectrum . . . 43
5.16 Naphthalene Absorption Spectrum . . . 44
5.17 Methanol Absorption Spectrum . . . 44
5.18 Phenol Absorption Spectrum . . . 45
5.19 Acetone Absorption Spectrum . . . 45
5.20 Propanal Absorption Spectrum . . . 46
5.21 Glyoxal Absorption Spectrum . . . 46
5.22 Acetic Acid Absorption Spectrum . . . 47
5.23 P-Xylene Absorption Spectrum . . . 47

6.1 Axes Definitions for 3-D Plume Modeling . . . 49
6.2 Modeled Plume Width (Idle) . . . 51
6.3 Spatially Modeled UHC Concentration (Idle) . . . 52
6.4 Temporally Modeled UHC Concentration (Idle) . . . 52
6.5 Modeled Plume Temperature (Idle) . . . 57
6.6 Top-Down View of Idle Plume Concentration . . . 58
6.7 Side View of Idle Plume Concentration-Path-Length . . . 59
6.8 3-D Idle Plume Concentration . . . 60

7.1 Modeled Plume Concentration-Path-Length with Gaussian Plume Equation . . . 63
7.2 Temporally Modeled Plume Concentration-Path-Length . . . 64
7.3 Plume Transmission at 15 m Downwind . . . 66
7.4 Plume Transmission at 264 m Downwind . . . 66
7.5 Plume Transmission at 600 m Downwind . . . 67

7.6 Plume Transmission at 750 m Downwind . . . 67
7.7 Background (Sky) and Reflective Plate Radiance . . . 69
7.8 Atmospheric Transmission and Reflective Plate Emissivity . . . 70
7.9 Ground-Based Transmission at 5, 10, 50, and 100 m Distances . . . 71
7.10 Plume and Background Radiance at 15 m Downwind . . . 72
7.11 Plume and Background Radiance at 264 m Downwind . . . 73
7.12 Plume and Background Radiance at 600 m Downwind . . . 73
7.13 Plume and Background Radiance at 750m Downwind . . . 74
7.14 Profiles of On-Hand Filters from 8 – 14 μm . . . 75
7.15 Magnified View of Filter Profiles from 8 – 10 μm . . . 77
7.16 Difference Between Plume and Background Radiance at 264 m . . . 77
7.17 On-Hand Filters for Plume Tracking . . . 78
7.18 Ideal Filters for Plume Tracking . . . 79
7.19 Plume-Background Difference for the On-hand Plume Tracing Filter . . . 80
7.20 Plume-Background Difference for the Ideal Plume Tracing Filter . . . 81
7.21 Temporal Predictions of Plume Tracking with On-Hand Filters . . . 83
7.22 Temporal Predictions of Plume Tracking with Ideal Filters . . . 84

8.1 Rochester International Airport . . . 86
8.2 Effect of Formaldehyde on Plume Transmission . . . 89
8.3 Effect of Acetaldehyde on Plume Transmission . . . 90
8.4 Effect of Ethylene on Plume Transmission . . . 90
8.5 Effect of Propene on Plume Transmission . . . 91
8.6 Effect of Naphthalene on Plume Transmission . . . 91
8.7 Effect of Methanol on Plume Transmission . . . 92
8.8 Effect of Acetic Acid on Plume Transmission . . . 92

List of Tables

2.1 Landing-Takeoff Cycle by Engine Mode 6
2.2 Engine Productions Used to Measure Pollutant Emission Indices 9

3.1 UHC Importance Rankings 22

7.1 Hydrocarbons Included in Plume Models, Emission Indices, and Molar Masses 62
7.2 Characteristics of the On-Hand Filters 76

8.1 Filter Locations for Individual Hydrocarbon Tracking 89

List of Acronyms

CPL	concentration-path-length [ppmm]. 50–52, 56, 59, 62–66, 72, 74, 82, 87
EI	pollutant emission index [g/kg]. 7–10, 14–20, 23, 24, 49, 55, 61, 62, 87, 88, 94
FF	engine fuel flow [kg/s]. 7–9, 49, 55
TIM	time-in-mode [min]. 7
APEX	Aircraft Particle Emissions eXperiment. 18–22, 61
B737	Boeing-737 aircraft. 3, 4, 18, 49, 50, 55, 61, 85, 94
CWL	center wavelength [μm]. 72–74, 76–79, 89, 95
EXCAVATE	EXperiment to Characterize Aircraft Volatile Aerosol and Trace-species Emissions. 17, 18, 20, 22
FOV	field-of-view [°]. 24, 25, 93
FTIR	Fourier transform infrared spectroscopy. 12, 34
FWHM	full-width half-max [μm]. 75, 76, 78, 79
GC	gas chromatography. 11, 12, 15–17
HAP	hazardous air pollutants. 10, 21–23
HCHO	formaldehyde. 19, 20
LTO	landing/takeoff cycle. 3, 5–7, 9–11, 23, 94
LWIR	longwave infrared. 9, 12, 13, 24–26, 35, 38, 94
MODTRAN	MODerate resolution atmospheric TRANsmission. 68, 70, 87
MWIR	midwave infrared. 9, 12, 35
NEΔT	noise equivalent temperature. 25, 61, 79–81, 95
NER	noise equivalent radiance. 79–81
NMHC	non-methane hydrocarbon. 17, 18
ppm	parts-per-million (concentration). 49, 50, 56, 62, 65
ppmm	parts-per-million-meter (absorption). 56, 65
PTR-MS	proton transfer reaction - mass spectrometry. 12, 15, 19, 20
TILDAS	tunable diode laser differential absorption spectroscopy. 12, 13, 15, 19

UHC unburned hydrocarbons. 3, 4, 8–12, 14, 15, 17–23, 33–35, 38, 48–50, 56, 61–63, 65, 75, 82, 85, 87–92, 94–96

VOC volatile organic compounds. 9, 12, 16, 81, 82

List of Institutions

ACRP Airport Cooperative Research Program. 21, 22

EPA Environmental Protection Agency. 7, 8, 18

FAA Federal Aviation Administration. 18, 22
FLIR FLIR Systems, Inc.. 13, 79

ICAO International Civil Aviation Organization. 7–10, 15–18, 20, 22, 23, 34, 49

NASA National Aeronautics and Space Administration. 15, 17–19, 23, 61
NIST National Institute of Standards and Technology. 34

PNNL Pacific Northwest National Laboratory. 34, 35, 68, 69, 87, 95

List of Symbols

$B_\lambda(T, \lambda)$	blackbody radiance. 28, 32, 68
$L(\lambda)$	wavelength-dependent source radiance. 27
M	molar mass. 49, 56, 62
N_a	Avogadro's number (6.022×10^{23} [1/mol]). 49
Q	transition probability density. 53, 54
R	Ideal Gas Constant (8.314 [J·mol^{-1}K^{-1}]). 50
T	temperature. 27, 50, 68, 69
V	volume. 50, 56
$\alpha(\lambda)$	absorption profile [ppmm^{-1}]. 65
η	pollutant concentration [ppm]. 50, 56, 65
λ	wavelength. 68
ρ	reflectance. 27
σ	filter profile standard deviation [μm]. 75
τ	transmission. 27, 87
ε	emissivity. 28
c	speed of light (2.998×10^8 [m/s]). 68
h	Planck constant (6.626×10^{-34} [J·s]). 68
k_B	Boltzmann constant (1.381×10^{-23} [J/K]). 68
q	pollutant emission rate. 54, 55, 57
z	path length [m]. 65
P	Atmospheric pressure. 50

Chapter 1

Introduction

In recent years, communities surrounding airports have become increasingly concerned about the impact of aviation emissions on local air quality. Major cities across the United States and London have been featured in news publications drawing attention to the adverse health effects associated with living near an airport.

As early as 2000, the city of Park Ridge, IL commissioned the Environ Corporation to perform a study assessing the health risks caused by living near Chicago O'Hare International Airport. The Environ study found that hypothetical lifetime cancer risks at the airport fence line were five times higher than background levels[1]. The *Chicago Tribune* reported on this as future studies were being proposed[2]. A counterstudy performed by the Environmental Protection Agency of Illinois determined that while airport-related emissions do affect the air quality in local communities, the pollutant concentration levels were no higher than in other urban areas around the country[3]. This debate was sparked by talk of further expanding O'Hare.

In 2010, the *National Geographic* reported on a study from the Massachusetts Institute of Technology that found people are more likely to die from plane exhaust than in a plane crash[4,5]. Specifically, ten times more people die from jet engine emissions than in plane crashes. This study was the first to consider cruise emissions in addition to local emissions.

Los Angeles and Boston appeared in news articles regarding local airport emissions in May 2014. The *Los Angeles Times* detailed the research of a University of Southern California/University of Washington

team that measured particulate emissions downwind of Los Angeles International Airport[6]. Pollutant concentration levels were found to be four times higher than the ambient air up to ten kilometers away from the airport[7]. The *Boston Globe* publicized a state report with findings that children growing up in neighborhoods bordering Logan International Airport are three to four times more likely to develop respiratory issues compared to children living further away[8,9].

London Heathrow has been debating adding a third runway for several years, which environmental activists are protesting. The final decision has been delayed multiple times by the prime minister, most recently again until the summer of 2016[10].

These concerns are not likely to be ameliorated anytime soon. Modern aircraft are, on average, 80% more fuel efficient than they were in the 1960s[11], and emission standards are continuously lowered to encourage further improvements. Better fuel efficiency is achieved by designing lighter aircraft, improving flight aerodynamics, and increasing engine performance. However, aviation emissions are still increasing due to the rapid industry growth[12]. In 2012, the transportation sector accounted for 28% of greenhouse gas emissions in the United States[13]. 12% of those emissions were from aviation, which accounted for 3.36% of total CO_2 emissions in the US. Further, air traffic and the number of air passengers continues to increase by the year. Between 1970 and 2010, the number of travelers increased ten-fold, from 310 million to 3.2 billion passengers each year[14]. Boeing predicts that global air travel will continue to increase by 5% each year until 2027[15]. This demand for growth will likely offset improvements in engine efficiency and fuel consumption, allowing further increases in emissions[16].

The first step in improving air quality in the communities surrounding airports is to better understand the dynamics of jet engine emissions. Engine emission rates are poorly understood, and developing an emission inventory for an airport is a difficult task (see § 2.1.2). There are a variety of commercial sensors capable of monitoring gaseous emissions but their prohibitive costs and interference with daily operations makes them impractical for large-scale deployment.

1.1 Problem Statement and Objectives

There are currently no inexpensive, portable, and unobtrusive sensors available to monitor the spatial and temporal distribution of jet engine exhaust plumes. The objectives of this study are to:

1. Characterize the phenomenology of common gases found in jet engine exhaust.
   (a) Identify gases present in common aircraft engine plumes, and determine their spectral features.
   (b) Determine emission rates for individual exhaust constituents.
2. Assess the feasibility of designing an inexpensive, portable, and unobtrusive multispectral imaging system to track the spatial and temporal nature of engine exhaust plumes.
   (a) Propose a system design that will maximize the detectability of a typical Boeing 737 (B737) engine exhaust plume.
   (b) Develop a governing equation to determine the sensor-reaching radiance of the imaging system.
   (c) Model the pollutant concentrations within the plume, and predict the plume transmission.
   (d) Predict the sensor-reaching radiance, and select filters to maximize plume detectability.
3. Assess the potential for using the proposed multispectral imaging system to quantify pollutant emissions.

1.2 Layout

This thesis contains nine chapters. The first, and current chapter (1) introduces the problem and declares the thesis objectives.

The second chapter (2) provides background on what is currently known about jet engine emissions. It introduces the landing/takeoff (LTO) cycle, common pollutants found within engine exhaust (*Objective 1a*), and briefly describes the pollutants of interest, unburned hydrocarbons (UHCs). The background also describes common methods of quantifying gaseous emissions.

Chapter 3 is a literature review, presenting previously published work on monitoring and quantifying engine pollutants. Special focus is placed on papers discussing the tracking of UHCs, and what is already known about this subset of pollutants. The chapter concludes by discussing several multispectral infrared imaging systems that have been developed for scenarios comparable to observing aircraft exhaust.

The fourth chapter (4) details the proposed imaging system, from its layout and required components to a description of the system radiometry (*Objective 2a*). It concludes by presenting the radiometric governing equation of the imaging system and discussing how each parameter is measured (*Objective 2b*).

Chapter 5 further addresses *Objective 1a* by providing spectral profiles for the UHCs of interest in this study. A small study is done to ensure that the effects of pressure broadening on the observed spectral features will be minimal.

We address *Objective 2c* in Chapter 6, which presents two different methods of modeling the pollutant concentrations in the plume. The first method tested the Ideal Gas Law to estimate the amount of emitted UHCs. While each parameter in the Ideal Gas Law was relatively well-modeled, the Ideal Gas Law is for an enclosed system and an exhaust plume does not meet that requirement. The second method tested was the Gaussian Plume Equation. This method was used for the rest of the work.

Objective 2c is further addressed in Chapter 7, along with *Objective 1b*, which presents the expected concentration profile of hydrocarbons downwind of a typical B737 engine, and spectral profiles of the plume transmission at varying downwind distances. Chapter 7 also selects plume tracing filters and presents the predictions of sensor-reaching radiance for the proposed imaging system (*Objective 2d*). These predictions are used to assess the plume detectability as a function of time and downwind distance. The chapter concludes with temporal models of multiple aircraft taxiing past the imaging system.

Chapter 8 describes future work that can be done on this problem, and includes an assessment of the potential for quantifying gaseous emissions with the proposed imaging system (*Objective 3*).

Finally, Chapter 9 summarizes the work presented and concludes the thesis.

Chapter 2

Background

To better formulate the problem an overview of the landing/takeoff (LTO) cycle is provided, followed by a description of the specific pollutants present in exhaust. The chapter concludes with a discussion of existing methods used to track and quantify jet engine plumes emissions.

2.1 Jet Engine Emissions

2.1.1 Landing-Takeoff Cycle

The LTO cycle is the entirety of aircraft operations that occur below 915 [m] (3000 [ft])[17]. This is the atmospheric mixing height, or inversion layer, below which emissions will have the greatest impact on local air quality. The cycle consists of the takeoff, climb out, approach, and taxi/idle phases of a flight (Figure 2.1). The entire LTO cycle takes about 33 minutes, with the majority of time being spent taxiing or idling (Table 2.1)[17].

The cruising phase of flights will not be considered in this work, as it will not be directly observable with a ground-based imaging system, and wind currents will add a layer of complexity in determining which communities are truly affected by the emissions. However, the cruise cycle may still have significant impact on the air quality of communities distantly located from airports[4].

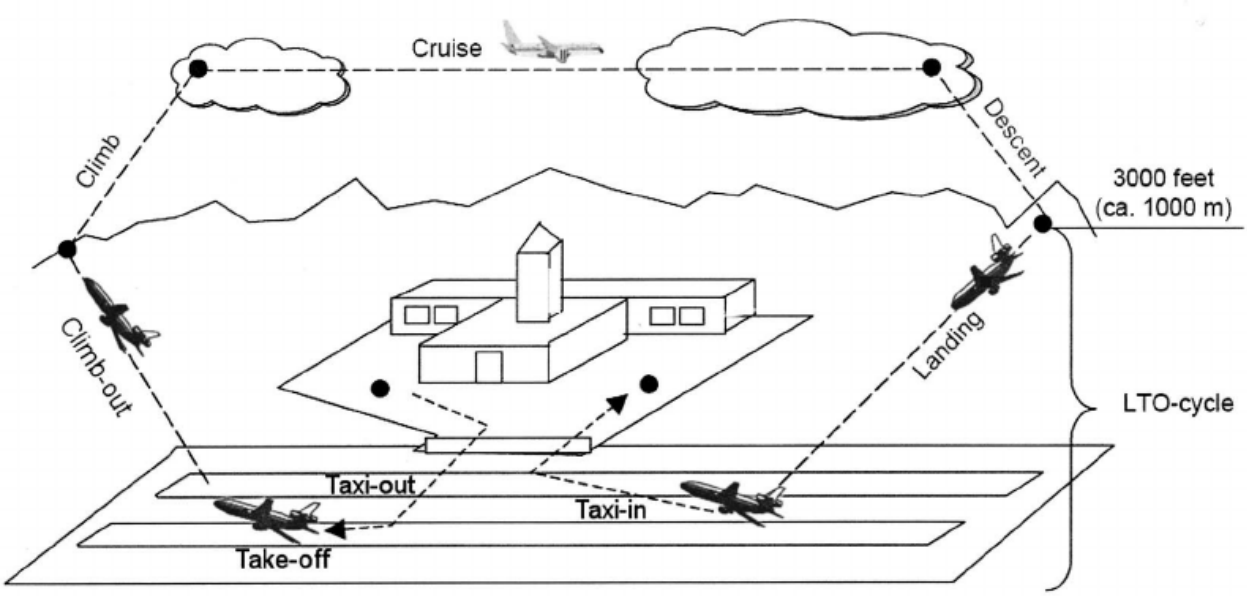

Figure 2.1: A diagram of the LTO cycle, including the taxi/idle phase, the takeoff, climb out, and landing. A typical LTO cycle takes about 33 minutes.

2.1.2 Emissions Inventory

A complete air quality assessment requires an emissions inventory and a dispersion model. The following sections discuss how to obtain an emissions inventory, and future chapters discuss the pollutant dispersion model (Chapter 6). There are multiple ways of calculating an emissions inventory, varying in level of complexity and required information. Each method employs a bottom-up approach, starting with the calculation of emissions mass. The different approaches can be divided into simple, advanced, and sophisticated[17]. Only basic knowledge is required for the simple approach, and the necessary data, such as typical engine emissions

Table 2.1: LTO cycle by mode. LTO occurs below 3000 feet and typically lasts for 33 minutes[17].

Mode	Time in Mode (minutes)		% Maximum Engine Thrust
Take-off	0.7		100
Climb out	2.2		85
Approach	4.0		30
Taxi/Idle	26	7.0 (in) 19.0 (out)	7

and engine fuel flow (FF) rates, are easy to access. The methodology is straight forward but the resulting confidence is low. On the other hand, the sophisticated approach requires in-depth knowledge and cooperation between multiple agencies. Rather than readily available publicized data, the sophisticated approach makes use of actual engine/aircraft operational data, which gives a much higher confidence in the inventory result.

This work begins with the simple approach, which is made by knowing the pollutant emission index (EI), defined as the grams of pollutant emitted per kilogram of fuel burned [g/kg]; the engine FF [kg/s]; the time-in-mode (TIM) in minutes; and the number of engines on the aircraft (NE). Three of these parameters (EI, FF, and TIM) will change based on the pollutant species or the phase of the LTO cycle, so even the simplest method of calculating an emissions inventory is a multi-step process.

Allowing i to be the pollutant, j to be the engine specification, and k to be the LTO mode, the total mass of pollutant M_{ij} emitted over one phase of an LTO cycle is:

$$M_{ij} = \sum (TIM_{jk} \times 60) \times (FF_{jk}) \times (EI_{ijk}) \times (NE_j). \tag{2.1}$$

This approach uses the standard TIM values from Table 2.1, and publicized values of EI and FF, on a per engine basis (see § 2.1.3). In a true operational scenario, aircraft may have longer taxi/idle times due to a busy airport schedule. Operational thrust levels, and thus fuel flows, may be different as well. Thus while the simple approach will not be of use for developing air quality standards and monitoring airport emissions, it provides a basic starting approach with which to create radiometric models of exhaust plumes.

2.1.3 Monitored Pollutants

Both the United States and the United Kingdom began developing broad regulations to control air pollution in the 1950s and 60s. The UK established a Clean Air Act in 1956, and the US followed suit in 1963. The US Clean Air Act let to the establishment of the Environmental Protection Agency (EPA) in 1970, and the National Ambient Air Quality Standards (NAAQS) of 1971. As the aviation industry grew, so did international concern over monitoring aircraft emissions to protect the environment and public health.

In 1944 the International Civil Aviation Organization (ICAO) was established as a specialized agency

by the United Nations. The ICAO is in charge of developing international emission standards for aircraft with rated outputs greater than 26.7 [kN][18]. Current emission standards are set for NO_x, CO, unburned hydrocarbons (UHCs), and smoke number, with an additional standard for CO_2 being developed (*Objective 1a*)[18,19].

In order to be certified, new engine models must undergo testing to demonstrate that they meet ICAO standards. Once certified, subsequent productions of the same model can enter the market without further testing. Extensive data is collected by the ICAO including the FFs and EIs of engines at the four thrust levels from Table 2.1. Comprehensive testing results are published in the ICAO Emissions Databank[20], which currently includes 517 certified engines.

A typical airport emissions inventory will include five major categories of pollutants[17]:

1. nitrogen oxides (NO_x),
2. UHCs,
3. carbon monoxide (CO),
4. particulate matter (PM), and
5. sulphur oxides (SO_x).

Emissions of the first four listed pollutants can be predicted with the information published in the ICAO Databank. While there are no standards set for SO_x emissions and no published EIs per engine, they are still expected to have a significant impact on local air quality; thus they are generally included in emissions inventories.

The ICAO regularly updates emission standards to reflect technology improvements. The agency has 191 member States which agree to enforce ICAO emissions standards, or provide written reasoning for not doing so. In the United States, the EPA adjusts national regulations to match those of ICAO[21].

There are multiple concerns with using the published EIs and FFs to obtain an estimate of total emissions. Firstly, manufacturers are not required to update EIs as engines age or undergo maintenance. This problem is mostly self-resolved though, as it is in the best interest of airlines to maintain high engine

Table 2.2: Number of engine productions used to measure pollutant *EI*s. One or two productions were used to determine *EI*s for 74% of engine models.

Engine Productions Tested	Percentage
1	53
2	21
3	18
> 4	8

performance as a cost-saving measure. More interesting is the fact that the many engines enter the market based on the test results of a single engine (Table 2.2). 74% of engine *EIs* are based on the testing of only one or two engines, so the variability of mass production is poorly understood. Lastly, operational thrust levels are frequently different from ICAO standards, which further complicates the task of inventorying emissions.

Although individual *EIs* for specific engines may be unreliable, we can still achieve a general understanding of how the *EIs* depend on engine thrust, or *FF*. Figure 2.2 shows the average *EI* of the 517 engines for each monitored pollutant, and how they relate to the engine thrust. Note that smoke number is a dimensionless quantity.

Emission levels of nitrous oxides and smoke number are inversely related to carbon monoxide and UHC emissions, making it difficult to adjust engine power in such a way that lowers all emissions. In terms of plume detectability, an imaging system would perform best when observing pollutants where the *EI* is greatest. For instance, nitrous oxides would be best observed during the takeoff phase of LTO, while CO would be best detected during the taxi/idle. Prominent spectral absorption features of NO_x and CO are only observed the midwave infrared (MWIR) however, where no inexpensive commercial cameras are currently available. Although UHCs have relatively low *EIs*, they have very strong absorption features in the longwave infrared (LWIR), making them a suitable target for plume tracking (see Chapter 5).

2.1.4 Unburned Hydrocarbons

UHCs are a result of incomplete combustion in the engine and are also referred to as volatile organic compounds (VOCs). Reactions between UHCs and nitrous oxides form tropospheric ozone, one of the

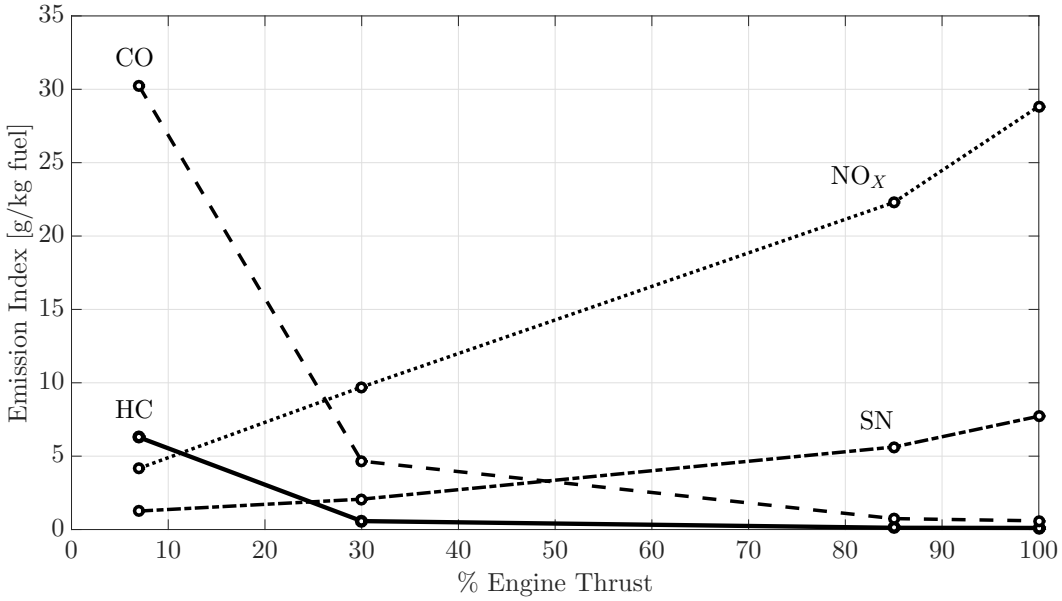

Figure 2.2: Average *EI* for the four ICAO monitored pollutants during each stage of LTO. Smoke number is dimensionless.

primary constituents of urban smog[22]. Some UHCs are more reactive than others; for instance, formaldehyde will produce almost two orders of magnitude more ozone than ethane[23]. Thus an adequate method for monitoring UHC emissions could be useful in reducing airport-generated smog.

A subset of the UHCs present in aircraft exhaust are considered hazardous air pollutants (HAPs), defined as chemicals which may cause cancer or birth defects[24]. Examples of HAPs present in exhaust include[17]:

- acetaldehyde,
- acrolein,
- benzene,
- formaldehyde,
- naphthalene,
- propionaldehyde,
- toluene, and
- xylene.

These HAPs are included in some inventories, but individual UHC *EIs* are not well-studied, so predictions of specific HAP emissions will be produced at a lower confidence. Further, any inventories of overall UHC

emissions will only be as good as the constituents included. Error will be introduced when individual UHCs are excluded from the calculation.

Further information about UHCs is provided in Chapters 3 and 5.

2.2 Methods of Monitoring Exhaust Plumes

Multiple methods have been employed to monitor engine emissions of aircraft during the LTO cycle. In the following subsections we discuss the advantages and disadvantages of each of these techniques, providing useful background for Chapter 3.

2.2.1 Direct Probing

Probing exhaust plumes is one of the most direct methods of monitoring emissions. Plume samples are captured in canisters and transported to a laboratory, or transferred to an on-site processing center, where they are studied in further detail.

Studies that directly probe the exhaust from an aircraft engine are generally conducted in test facilities. This allows the scientists to modify more parameters in their experiment, such as the engine model, thrust and fuel type. Studies can also take place near the taxiways or runways. However, direct probes are impossible to place directly behind the engine exit during daily airport operations, and thus ineffective for continuous, direct monitoring of plumes.

Researchers use a variety of techniques to analyze gas samples, detailed next.

2.2.1.1 Gas Chromatography

Gas chromatography (GC) separates chemical constituents based on their different rates of passage through a gas stream. It takes several minutes, but allows accurate identification and quantification of individual pollutants within the collected gas. This is especially useful for measuring UHC emission ratios.

2.2.1.2 PTR-MS

Similar to GC, proton transfer reaction - mass spectrometry (PTR-MS) also requires direct probing of a gas, but PTR-MS results can be obtained in milliseconds. Rather than chromatographic separation, PTR-MS measures the individual mass-to-charge ratios within a sample to determine the chemical composition of a gas. This technique was developed, in major part, with the goal of monitoring of UHCs/VOCs. PTR-MS systems are also simple and compact, allowing them to be used in portable laboratories for on-field measurements. They are impractical for large-scale deployments though, as a basic system can cost up to $300,000[25].

2.2.2 Fourier Transform Infrared Spectroscopy

MWIR and LWIR emissions can also be monitored by Fourier transform infrared spectroscopy (FTIR). Unlike other spectral methods, presented later, FTIR spectroscopy captures the entire infrared spectrum of the observable gas. The target is illuminated with a polychromatic infrared source and a Michelson interferometer is used to block wavelengths individually. The result is an interferogram that can be converted into a full spectrum by a Fourier transform. Since the polychromatic source spectrum has been modified by the gas, radiative transfer models can predict the concentrations of individual species.

This technique does not suffer from the same problem as direct probing, because it can be placed to the side of the runway and not interfere with airplane operations. However, spectroscopy instruments are also quite expensive.

2.2.2.1 TILDAS

Like FTIR spectroscopy, tunable diode laser differential absorption spectroscopy (TILDAS) systems are portable and can be operated unobtrusively. Rather than measuring the entire infrared spectrum, a tunable diode laser is set to a wavelength coincident with an absorption feature in the gas of interest. The change in transmitted radiation as the laser illumination propagates through the gas allows for detection and quantification. This technique can be employed across sample paths greater than 2 [km], but many studies related to aircraft exhaust will use the technique in the laboratory on a directly probed sample[26]. Common gases

of interest are methane, carbon monoxide, and nitrous oxide.

2.2.3 Multispectral Imaging

Finally, multispectral imaging systems have been designed to monitor specific gaseous emissions. Similar to TILDAS, a camera can observe specific gases with a properly selected narrowband filter that overlaps the gaseous absorption features. This technique has been deployed to observe factory operations and detect gas leaks. While the previous examples have only provided single point or line-of-sight concentration measures, a filtered imaging system has the capability to monitor large swaths of area at high temporal resolution. These imaging systems are also unobtrusive to airport operations. Furthermore, multispectral imaging is relatively inexpensive compared to the other methods. A LWIR camera from DRS and FLIR Systems, Inc. (FLIR) are in the range of $3000, while filters can be purchased for under $1000[27,28].

Chapter 3

Literature Review

Engine pollutant emission indices (EIs) are determined on a per-engine-model basis, and subsequent production variability is not well monitored (§ 2.1.2). A capability to determine EIs for individual engine productions would be helpful in creating airport emission inventories and in determining the exposure levels of airport workers and local communities to harmful pollutants. Research into measuring engine-specific EIs began in the 1980s and continues to the present-day, using a variety of the methods presented in §2.2. In this chapter we present the current status of research on EI determination, specifically related to unburned hydrocarbons (UHCs), and conclude by describing multispectral imaging methods for gas detection.

3.1 1980s – 1990s Work on Monitoring UHCs

Spicer *et al.* determined engine EIs for speciated and total UHCs, CO, CO_2, NO, and NO_2 as early as 1984[29]. Two different aircraft turbine engines were tested at a variety of thrust levels, using the direct probing method described in §2.2.1. This led to a chemical speciation of the UHCs found in jet engine exhaust. Other studies had attempted this in the past, but the Spicer *et al.* work is still relevant as a comparison case for measurements made more recently[30]. Throughout the 1980s, Spicer *et al.* determined EIs for ten different turbine engines[31–33].

In 1992, Spicer *et al.* presented results from testing F101 and F110 bypass turbine engines at a variety

of thrust levels, including idle. Measurements were taken indoors at the Production Engine Test Facility in Tinker AFB, Oklahoma City, OK[34]. Gas chromatography (GC) methods were used to analyze the measurements taken from a 12-port sampling probe that was placed 0.3 – 0.6 [m] behind the engine exhaust nozzle (§2.2.1). The analysis scheme accounted for 70 – 100% of organic carbon emissions, although some species were not individually resolved. This indicates the results being useful for future environmental impact assessments. Spicer *et al.* also confirmed that UHC emissions increase at lower thrust levels, and noted that methane is normally excluded from UHC measurements, as exhaust methane is likely due to atmospheric methane used for combustion (i.e. it is not created by the engine). Work on individual engines continued through the 1990s, and in 1994, Spicer *et al.* noted that low molecular weight UHC species found in engine exhaust are likely due to combustor reactions rather than unburned fuel[35]. The 1994 work also found significantly increased methane emissions compared to the previous Spicer *et al.* work, leaving the status of methane emissions in aircraft exhaust uncertain.

3.2 UHC Studies of the 2000s

A multitude of work studying UHC speciation was performed in the 2000s, including two major National Aeronautics and Space Administration (NASA) campaigns, EXCAVATE and APEX I-III (§3.2.1 – 3.2.2).

In 2006, Herndon *et al.* used proton transfer reaction - mass spectrometry (PTR-MS) and tunable diode laser differential absorption spectroscopy (TILDAS) (§2.2) to obtain speciated UHC *EI* measurements of 45 advected aircraft plumes from Boston Logan International Airport[36]. Unlike the previous studies of Spicer *et al.*, these measurements were performed on operational aircraft. However, specific engine models were unknown, and only predicted based on aircraft type. Herndon *et al.* used individual UHC measurements to determine a total UHC *EI* of 2.9 [g/kg][36]. Compared to International Civil Aviation Organization (ICAO) *EIs* for similar engine types (the 25% to 75% percentile *EIs* are 3.8 – 5.1 [g/kg]), this indicates that 50 – 70% of total UHC emissions were detected. A similar comparison was made with the European Environment Agency's EMEP COMAIRE program (not discussed here), suggesting that only 40% of total UHC emissions were detected[37]. Using the 40% estimate, Herndon *et al.* estimate a total UHC *EI* of 7.2 [g/kg], compared to the Spicer *et al.* estimate of 9.1 [g/kg][36]. These are significantly higher than the ICAO range of 3.8

– 5.1 [g/kg]. The difference is attributed to operational idle thrust being 3% lower than ICAO tabulated measurements, indicating that emissions may be 40 – 90% higher than expected.

Schürmann *et al.* presented volatile organic compounds (VOCs) mixing ratios obtained from aircraft at Zurich Airport in Switzerland in 2007. The difference in speciations for engine exhaust during taxiing and during kerosene refueling was examined using direct probing and GC methods. Tremendous levels of highly reactive ethene and propene were emitted during the taxi and idle phases compared to airport background levels, and similar to previous studies, the measured EIs were found to be up to two times higher than published ICAO values[38]. Finally, Schürmann *et al.* highlighted the benzene:toluene ratio as a method to discriminate refueling from exhaust emissions.

This was followed in 2008 by Agrawal *et al.* performing the first on-wing investigation of aircraft engine emissions at the Ground Runup Enclosure at Oakland International Airport[39]. Direct probing was used to study the emissions of four CFM-56 engines, similar to the engine studied in this work. Samples were captured at one meter downwind to match the standards of ICAO testing. Formaldehyde and acetaldehyde were found to be the most dominant carbonyl species in aircraft exhaust. The measured formaldehyde EI was low compared to Spicer *et al.*, but this was attributed to a significant difference in ambient temperatures[34].

Herndon *et al.* continued work in 2008 with a study of in-use aircraft emissions at the Hartsfield-Jackson Atlanta International Airport. The study observed over 350 exhaust plumes, and while mainly focused on take-offs, results were obtained for idle plumes as well. A major goal of the study was to study aged, diluted plumes. Two sampling laboratories, the Aerodyne Mobile Laboratory and UMRCOE Mobile Diagnostic Facility, were used for measurements, and were typically situated 100+ [m] away from the runways and taxiways[40]. Delta Airlines gave extensive support to this campaign, particularly with identifying the specific engines associated with aircraft tail numbers. The result is the first study which measured formaldehyde and carbon monoxide simultaneously in wind advected plumes. The formaldehyde EI obtained in this work agreed well with previous studies[36].

3.2.1 NASA EXCAVATE Campaign

The NASA EXperiment to Characterize Aircraft Volatile Aerosol and Trace-species Emissions (EXCAVATE) was conducted in winter 2002 and results were published by Anderson *et al.* in 2006[41]. Testing was performed at the NASA Langley Research Center's aircraft run-up facility in Virginia, when automobile traffic was light and airport operations were minimal. Direct probing at 10 [m] downwind was used to study emissions of a Boeing 757 (Rolls Royce engine RB211-535E4) with different fuels (high sulfur and low sulfur content) at a variety of thrust levels (idle, approach, low cruise, and high cruise)[41]. Unlike previous studies, idle measurements were taken at the ICAO-defined 7% thrust level, and not the typical 4% operational thrust. Eight samples of engine emissions (one per thrust level and fuel type combination) were captured, along with three samples of background air. Samples were processed at the University of California at Irvine with GC methods. Resultant concentration data were combined with engine CO_2 emission measurements to determine EIs for each species under study.

Anderson *et al.* found that the difference in methane concentrations between exhaust and background measurements was less than the 2σ uncertainty for all samples, furthering the original conclusion of Spicer *et al.* that methane is not a significant component in engine exhaust. In fact, negative EIs were found for methane emissions at higher thrust levels, indicating that the engine will in some cases burn methane out of the atmosphere. 27 total non-methane hydrocarbons (NMHCs) were also studied, excluding oxygenated compounds such as formaldehyde. Results showed that at idle power, more than 80% of UHC emissions are from species with $2-4$ carbon atoms[41]. As engine power increases however, nearly all NMHC emissions are from species with 4+ carbon atoms.

The study also found that while total UHC emissions decrease with increasing engine power, different functional groups of UHCs exhibit different trends with engine thrust. At low thrust levels, alkenes and alkynes make up more than 80% of the NMHC emissions, whereas at high thrust levels (60%), these groups only contribute to 20% of total NMHC emissions[41]. Total NMHC emissions were found to be a factor of 200 less at 61% thrust (climb-out power), compared to idle power. Anderson *et al.* found relatively good agreement between their measured NMHC EIs and the published ICAO values at idle, noting that minor differences were due to their exclusion of oxygenated UHCs and the fact that ICAO data is not corrected for

background levels (both causing the Anderson *et al.* measurements to trend lower). Finally, the study found differences in NMHC *EIs* from different fuel types, but attributed this to their sampling process rather than true differences in fuel impacts.

A major conclusion of the EXCAVATE work was that *EIs* would be more accurately measured with background levels taken into consideration, a practice the ICAO does not currently implement.

3.2.2 NASA APEX Campaign

The Aircraft Particle Emissions eXperiment (APEX) was a three-part collaborative effort between NASA, the Environmental Protection Agency's (EPA's) National Risk Management Research Laboratory, and a multitude of other organizations such as the Federal Aviation Administration (FAA), the US. Air Force's Arnold Engineering Development Center, the California Air Resources Board, General Electric, Pratt & Whitney, Rolls-Royce, three commercial airlines, two international airports, the Missouri University of Science and Technology Center of Excellence, the University of California-Riverside, and Aerodyne Research, Inc[42]. Organized in 2003, the main focus of the experiment was to update and improve *EIs* for engine-produced fine particulate matter (PM) and to assess the effect of fuel properties and engine operating conditions on PM formation. However, a multitude of results were obtained regarding UHCs as well, making the APEX campaign an important source of information for this work.

During each of the three experiments the EPA probed exhaust plumes 30 [m] downwind of the engine exit. In total, ten common engines used in commercial aircraft were tested during the APEX campaign, and 24 tests were conducted:

1. In APEX-1, performed at Edwards AFB in California, nine tests were conducted on a CFM56-2C1 engine mounted on a DC-8 airframe. The primary goal was to investigate the different effects of three fuel types on emissions at varying power settings.

2. There were four APEX-2 tests performed at Oakland International Airport in California. In this stage, typical operational jet fuel was used on a variety of CFM56 engines mounted on a Boeing 737 (B737). Results further characterized PM emissions and fuel type effects from the very common CFM56 engines.

3. APEX-3 consisted of eleven tests, and also furthered the understanding of PM emissions on common engine types. Testing was done at the NASA Glenn Research Center at the Cleveland-Hopkins International Airport. Two of the tests were conducted on CFM56-3B1 engines, and the remaining tests were conducted on the General Electric CJ610-8ATJ (used on a Lear Model 25), the Rolls Royce AE3007A1E and AE3007A1P (used on the Embraer ERJ145), the Pratt & Whitney PW4158 (used on the Airbus A300), and a Rolls Royce RB211-535E4-B (used on a B757)[42].

In 2007, Yelvington *et al.* reported on APEX-1 measurements taken with the Aerodyne Mobile Laboratory in April 2004. Formaldehyde and ethylene were measured with TILDAS and other major UHC species with PTR-MS[43]. Samples were taken at 1, 10, and 30 [m] downwind from the engine exit. Results confirmed that as expected, fuel type did not have a significant difference on UHC EIs. EIs were also not significantly affected by downstream distance. However, several new observations were made regarding UHC speciation:

- The ambient temperature was discovered to have a large effect on UHC EIs, where lower ambient temperatures produce higher EIs. The effect of ambient temperature was so pronounced that it obscured any effects related to fuel type or downstream distance. Yelvington *et al.* hypothesized that this was due to the direct relationship between ambient temperature and the combustor-inlet temperature. As the combustor-inlet temperature increases, so does combustion efficiency. The efficiency then decreases with lower ambient temperatures, leading to higher UHC EIs. The only aspect shown to have a larger effect on EIs than ambient temperature was the engine fuel flow.

- The effect of crosswinds on measurements taken at the 1 [m] probe was negligible, indicating that these measurements provided information on engine variability. A time series of one-second measurements taken over three minutes showed that the emission peaks of CO_2 and formaldehyde (HCHO) were anticorrelated, and the HCHO concentration varied by about 10%[43]. This caused a 10% variability in the HCHO EI, which the authors attributed to engine dynamics. They noted that this was the first time such a fluctuation has been observed, and suggested that the engine combustion efficiency may vary significantly over short time periods.

- Finally, the quick response time of the PTR-MS and TILDAS instruments allowed measurements to

be taken in between the thrust settings under study. Specifically, concentration measurements were obtained as the engines transitioned from the ICAO 7% thrust idle to the operational idle of 4% thrust. Yelvington *et al.* observed that the emission ratios (a precursor to *EI* measurements) of UHCs during the transient stage were nearly double the higher ratios at 4% thrust. This suggested that transitioning between thrust levels may lead to significant increases in UHC emissions.

Knighton *et al.* also reported on the PTR-MS measurements obtained in APEX-1[43]. Similar conclusions were reached regarding the fuel type and downwind distance having little to no effect on UHC emissions, but they also noted a strong linear correlation between HCHO *EIs* and *EIs* of other UHCs, suggesting that UHC emissions scale together. This suggested that UHC speciation does not significantly change as a result of fuel type or engine power, and seemingly contradicts the observations of Anderson *et al.* in the EXCAVATE campaign[41]. However, Anderson *et al.* observed the UHC speciation over a large variation in thrust level (4 – 60%), compared to the Knighton *et al.* work which observed the speciation from 4 – 7%. Knighton *et al.* concluded by tentatively identifying two new compounds present in the engine exhaust: methanol and acetic acid.

In 2009, Herndon *et al.* reported on APEX-2 measurements which were obtained at Oakland International Airport in August 2005[45]. The APEX-2 measurements further confirmed that UHC *EIs* can be consistently scaled relative to the HCHO *EI*, and determined HCHO emissions to be approximately 0.35 – 0.5 of total ICAO-measured UHC emissions. APEX-2 predicted that operational idle emissions were 1.5 – 2.2 times greater than the ICAO-defined idle, which is in slight contrast to the APEX-1 prediction that emissions are 3 – 4 times greater. This was potentially attributed to different experiment designs and further research was recommended. Herndon *et al.* concluded by predicting that UHC emissions determined with ICAO-defined *EIs* will be 16 – 45% underestimated.

Knighton *et al.* summarized the findings of Spicer *et al.* along with the EXCAVATE and APEX campaigns. At this point in the history of UHC speciation profiles, the Spicer *et al.* of 1984 work was more than two decades old. The goal of Knighton *et al.* was to present a final UHC speciation profile, which was made easier by the fact that both the Spicer *et al.* and APEX work studied a high bypass turbofan CFM56 engine[30]. The Spicer *et al.* work measured that 17 species accounted for 95% of the total UHC emissions:

- ethylene*
- formaldehyde*
- acetylene
- propene*
- acetaldehyde*
- acrolein*
- 1-butene*
- glyoxal*
- 1,3-butadiene
- benzene*
- methylglyoxal
- ethane
- propanal*
- butanal/crotanaldehyde
- 1-pentene*
- 1-hexene
- toluene*

Of these 17 compounds, 11 (indicated with a *) are represented in our UHC concentration model, which used species where direct comparisons could be made between Spicer *et al.* and the APEX results. A number of other species were included in our model as well, contributing to 1% or less of the total UHC emissions. The largest uncertainties in our model will come from the missing species of acetylene, 1,3-butadiene, methylglyoxal, ethane, butanal/crotanaldehyde, and 1-hexene. Knighton *et al.* noted that the overlapping Spicer *et al.* and APEX measurements all agreed to within one standard deviation except for the combination of acetone, propanal, and glyoxal, which agreed to within two standard deviations, and phenol, which was a significant outlier[30]. It was also noted that the relative UHC speciation does not vary at low thrust levels, up to 15%, where detection limits prevent further study. Regarding the current study focus, the UHC speciation at these higher engine powers will have limited impact on the local air quality surrounding airports. Knighton *et al.* concluded by referencing the need to determine which UHCs require further refinement in speciation profiles.

3.2.3 Airport Cooperative Research Program Report 7

In 2008 the Transportation Research Board published the Airport Cooperative Research Program (ACRP) Report 7: Aircraft and Airport-Related Hazardous Air Pollutants: Research Needs and Analysis[46]. This work focused specifically on hazardous air pollutants (HAPs) and thus some UHCs were not considered. The main findings of the ACRP report related to engine UHC emissions were:

1. The predominant source of HAP emissions at an airport is due to the taxi/idle phase of aircraft

Table 3.1: Relative importance of UHCs ranked by toxicity and emission levels.

ACRP Review	FAA 2003	*ORD 2005
Acrolein	Formaldehyde	Acrolein
Formaldehyde	Acetaldehyde	1,3-Butadiene
1,3-Butadiene	Benzene	Formaldehyde
Naphthalene	Toluene	Benzene
Benzene	Acrolein	Acetaldehyde
Acetaldehyde	1,3-Butadiene	Naphthalene
Ethylbenzene	Xylene	Toluene
	Lead	
	Naphthalene	
	Propanal	

*O'Hare Modernization Environmental Impact Statement

engines. Thrust levels (7% ICAO idle vs. 4% operational idle) and ambient temperatures can modify HAP emissions by more than a factor of two[46];

2. The relative importance of HAP emissions can be ranked based on their toxicity and the quantity of their emissions; and

3. The speciation work of Spicer *et al.* is regarded as accurate compared to the more recent work of the EXCAVATE and APEX campaigns.

Regarding Point 2 above, there are multiple rankings of the relative importance of individual HAP emissions, detailed in Table 3.1. Most of these HAPs are included in our speciation profile, with a notable exception being 1,3-Butadiene, where no comparison value was available between Spicer *et al.* and the APEX campaign[30]. Unlike the FAA and ORD rankings, toluene and xylene were omitted from the ACRP ranking; while emitted in large quantities, their toxicity risk is relatively low.

The ACRP review concluded by defining four problem statements for future research, three of which were related to aircraft HAP emissions:

1. The effect of ambient temperature on HAP emissions from idling aircraft must be further studied. Current studies only exist for ambient temperatures in the range from $8 - 35°$ [C]. Ambient temperatures significantly outside this range could result in uncertainties up to a factor of two regarding HAP emissions[46].

2. Operational thrust levels must be further characterized. *EIs* for UHCs at thrust levels below the ICAO-defined 7% idle may be twice as high as the certification value[46]. Further, *EIs* increase or decrease nonlinearly at different thrust levels, making operational predictions difficult[43].

3. HAP emissions need to be better characterized for general aviation aircraft. Measurements should be made for at multiple airports for a wide variety of in-service aircraft.

Each of the three research goals is accompanied with a brief description of future work, suggestion for funding levels, and points-of-contact.

3.3 Recent Work Monitoring UHC Emissions

In more recent work, Santoni *et al.* studied nitrous oxide and methane emissions on the NASA DC-8 aircraft during the first Alternative Aviation Fuel Experiment (AAFEX-I) in 2009[47]. The study examined methane emissions from three different fuel types: JP-8 (the most commonly used jet fuel throughout the world), and two Fischer – Tropsch fuels derived from natural gas feedstock and gasified coal feedstock. Results suggested that methane emissions from jet engines using different fuel types were indistinguishable. Santoni *et al.* also noted that engine history impacted methane emissions: engines starting from cold states released significantly more methane than engines that had previously operated at higher thrusts for extended periods of time. AAFEX-I results more closely resembled those of the 1994 Spicer *et al.* study which found higher levels of methane emissions, although the total methane emissions throughout the landing/takeoff (LTO) cycle are minimal[47]. The study concluded that alternative fuels will have little to no impact on methane emissions.

In 2013, Cain *et al.* studied the effect of fuel composition on gaseous and PM emissions from an Allison T63-A-700 engine operated at four different power settings[48]. Two fully formulated fuels, including the common JP-8, and four surrogate mixtures were tested in this study. The surrogate mixtures were representative of current and future alternative fuels. Samples were captured via direct probing and processing occurred in the Air Force Research Laboratory's Turbine Engine Research Transportable Emissions Laboratory. The fuel flow rate required to reach desired levels of thrust was similar for all fuel types, as were the major gaseous

emission levels (CO_x and NO_x). Aromatic hydrocarbon emissions however, specifically benzene and toluene, did show a dependency on fuel type. Cain *et al.* also examined the linear correlation between hydrocarbons and ethylene, similar to the Knighton *et al.* work of 2007[44]. (Knighton *et al.* compared hydrocarbon *EIs* to formaldehyde, but Cain *et al.* did not measure formaldehyde; thus the next most prominent hydrocarbon, ethylene, was used for comparison). Cain *et al.* found that the slopes were different depending on fuel type,which indicated that the decomposition and specific reaction pathways for hydrocarbons varied with different fuels.

3.4 Gas Detection with Multispectral Imaging

There has also been extensive research on multispectral IR imaging of gases. These studies were not specific to jet engine emissions, but they are a valuable source of information regarding the efficacy of our proposal.

General Monitors developed the Second Sight®TC infrared imaging system to improve plant safety[49]. The white paper cites three major benefits to infrared imaging when compared to traditional gas detection methods:

1. IR gas imaging provides wide-area coverage of entire of plants, or in our case airport taxiways. A typical device can image areas of 1 [km] in length by 0.5 [km] in length, with a field-of-view (FOV) of $15° - 60°$[49]. This method provides high spatial resolution that point samples are incapable of offering.

2. In addition to the high spatial resolution offered by IR imaging, a wealth of other information is offered as well. High temporal sampling can be achieved, and in combination with the spatial resolution, dispersion directions and emissions sources can be accurately identified.

3. Finally, IR imaging does not suffer from the major sources of false alarms that affect other methods of gas detection. In particular, the IR region is only minimally affected by water absorption and other significant atmospheric constituents[49].

The Second Sight®TC system uses a 384×272-pixel uncooled microbolometer IR focal play array designed for the longwave infrared (LWIR) region[49]. Although not designed specifically for jet engine exhaust

imaging, the imaging system targets hydrocarbons in the LWIR, similar to the proposed system in this document. This working system provides validity for the current proposal.

The imaging system comes with a six-filter wheel, which holds reference (background) and active (later referred to as "plume tracer") filters. Filters are selected to monitor individual hydrocarbons based on the location of their absorption features in the infrared. Care must be taken to ensure that filters are not placed where absorption features overlap, as the camera would then measure the levels of blended gases. Thus the difficulty of the problem will scale with how many unique hydrocarbon species are likely to be in the gaseous plumes. More species will lead to greater potential for absorption feature overlaps, whereas fewer species will allow for easier targeting.

The Second Sight®TC system also boasts the capability to quantify hydrocarbon emissions from plants; this study attempts to enable this for jet engine emissions.

In 2008, Kastek *et al.* presented multiple infrared imaging systems used for monitoring methane emissions. In one case an Agema THV900LW camera was equipped with filters overlapping the absorption features of methane and ammonia[50]. A second proposed method equipped a camera with a Fabry-Perot interferometer, which served as a tunable optical filter. The final modeled imaging system used a UL 03 08 1 microbolometer array and a Umicore Gasir Standard Lens 60 [mm] F/1.1[51]. The system had a FOV of 18.5° and a transmission greater than 92% in the LWIR. Computer simulations, similar to the ones presented later in this study, were run to predict the detection capabilities of an infrared camera. The radiance path from the background to the camera is much the same as the path presented next (Chapter 4)[51]. The noise equivalent change (delta) in temperature (NEΔT) is predicted based on the simulations; the current work examines plume detectability for different NEΔTs. The work of Kastek *et al.* gives further validity to the proposed imaging system in this work.

Similar to the work of Kastek *et al.*, the next chapter describes the radiometry of a LWIR imaging system designed to detect and monitor jet engine plumes.

Chapter 4

Proposed Imaging System

The information necessary to understand jet engine emissions and relevant previous studies was presented in the background and literature review (Chapters 2-3). This laid the groundwork to design an imaging system based on *Objective 2*. In the following chapter, the radiometric processes that create a gaseous effluent model for a sensor positioned overhead (§4.1) are introduced, a modified system design for a ground-based sensor (§4.2) is proposed, and the governing equation for the sensor-reaching radiance of our proposed imaging system is formed (§4.3).

4.1 Gaseous Effluent Model

The sensor-reaching radiance of an imaging system can be broken into two main regimes: reflective and emissive. The reflective regime relies on an illuminating source, such as the Sun, reflecting off the object of interest. This takes place in the visible portion of the electro-magnetic spectrum. The emissive regime relies on the self-emission of the object of interest, and occurs within the near-infrared through longwave infrared (LWIR) portion of the spectrum. Thus, most radiometric problems typically only require the modeling of one regime.

A jet engine exhaust plume will be almost completely self-emissive rather than reflective, so an infrared imaging system is required for detection. In order to model the detected radiance of the imaging system, all

sources of radiance that will reach the sensor must be analyzed.

Figure 4.1 depicts the layout of a general plume model for an overhead sensor, where $L(\lambda)$ is the wavelength-dependent source radiance, τ is the transmission, T is the temperature [K], and ρ is reflectance. In this model, a corresponds to atmospheric terms, b corresponds to the atmosphere below the plume, p corresponds to plume terms, d corresponds to downwelled radiance, and s corresponds to surface, or ground terms.

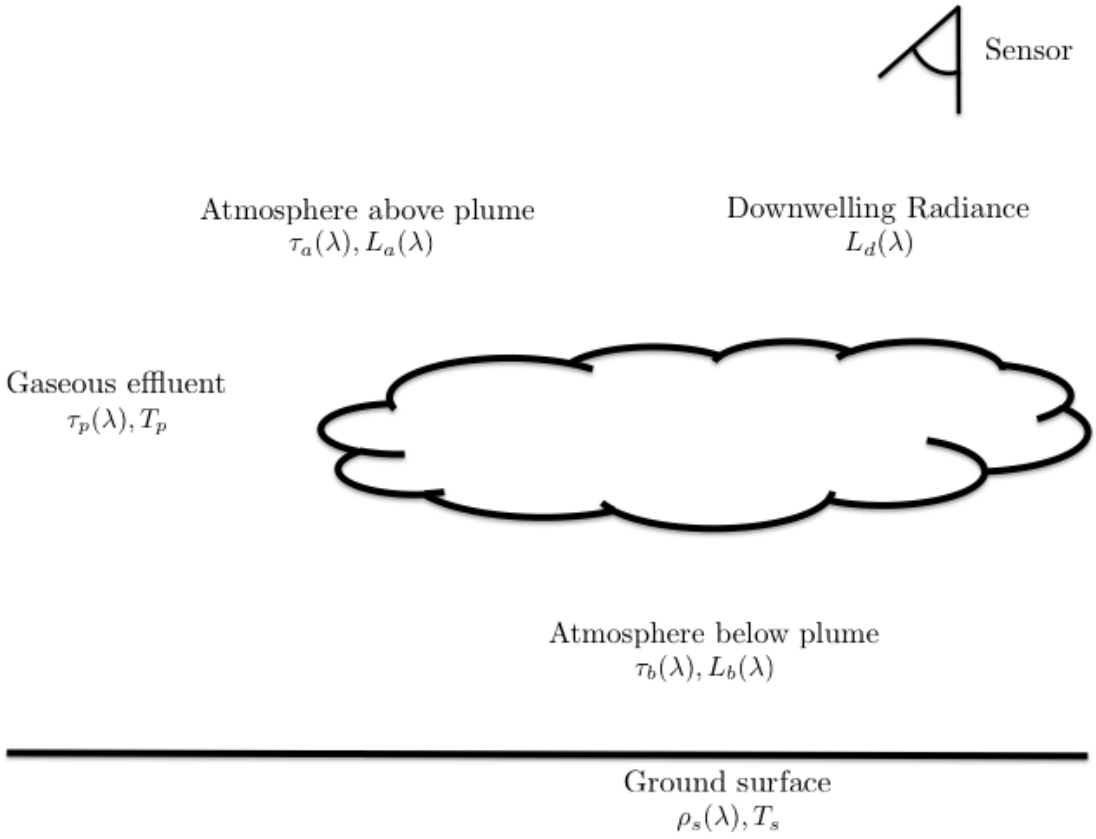

Figure 4.1: Schematic of a gaseous effluent model for an overhead sensor, adapted from Eismann[52].

There are five basic components to modeling the sensor-reaching radiance[52]:

1. surface emission (ground layer) through the plume;

2. upwelling emission from the plume;

3. downwelled radiance from the atmosphere, through the plume, reflected off the surface and back through the plume;

4. downwelled radiance from the plume, reflected off the ground surface and back through the plume; and

5. the path radiance, due to atmospheric scattering.

Ignoring scattering effects, Kirchoff's Law allows us to relate the emissivity (ε), transmission, and reflectance of objects:

$$\varepsilon + \rho = 1 \tag{4.1}$$

$$\varepsilon + \tau = 1 \tag{4.2}$$

The total radiance of the five previously listed terms can then be written as:

$$\begin{aligned} L_p(\lambda) =& \tau_a(\lambda)\tau_b(\lambda)\tau_p(\lambda)[1-\rho_s(\lambda)]B(T_s,\lambda) \\ &+ \tau_a(\lambda)[1-\tau_p(\lambda)]B(T_p,\lambda) \\ &+ \tau_a(\lambda)\tau_b(\lambda)\tau_p(\lambda)\rho_s(\lambda)[L_b(\lambda)+\tau_b(\lambda)\tau_p(\lambda)L_d(\lambda)] \\ &+ \tau_a(\lambda)\tau_b^2(\lambda)\tau_p(\lambda)\rho_s(\lambda)[1-\tau_p(\lambda)]B(T_p,\lambda) \\ &+ L_a(\lambda) + \tau_a(\lambda)\tau_p(\lambda)L_b(\lambda), \end{aligned} \tag{4.3}$$

where $B_\lambda(T,\lambda)$ is the blackbody radiance. If it can be assumed that the plume is relatively close to the ground, the below-plume atmospheric transmission is essentially one ($\tau_b = 1$), and the below-plume radiance is essentially zero ($L_b(\lambda) = 0$). This simplifies Equation 4.3 to

$$
\begin{aligned}
L_p(\lambda) =& \tau_a(\lambda)\tau_p(\lambda)[1-\rho_s(\lambda)]B(T_s,\lambda) \\
&+ \tau_a(\lambda)[1-\tau_p(\lambda)]B(T_p,\lambda) \\
&+ \tau_a(\lambda)\tau_p(\lambda)\rho_s(\lambda)[L_b(\lambda)+\tau_p(\lambda)L_d(\lambda)] \\
&+ \tau_a(\lambda)\tau_p(\lambda)\rho_s(\lambda)[1-\tau_p(\lambda)]B(T_p,\lambda) \\
&+ L_a(\lambda). \qquad (4.4)
\end{aligned}
$$

In this model, the plume transmission is the main parameter of interest, as a lower plume transmission leads to easier detectability[52]. A secondary factor in detectability is the temperature contrast between the atmosphere and the plume.

As we are proposing a ground-based imaging system capable of being deployed at any airport, this set-up must be modified and Equation 4.3 adjusted for a ground-based sensor. Modifications are described in the rest of the chapter.

4.2 Imaging System Design

The detectability of the plume must be maximized in order to effectively track the spatial and temporal nature of jet engine exhaust. The previous section stated that a low plume transmission will increase detectability; however, observers have no control over the plume transmission (see §7.2). The other factor in detectability, which can be controlled, is the temperature contrast between the plume and background.

The sensor will be ground-based, meaning a camera will look through the exhaust plume to a background of known (predicted) radiance. Two system designs were originally considered, one with a vegetation background and one with a sky background. The vegetation background would have allowed for easier set-up, as the camera could look directly across the runway through the plume, provided there was a forest nearby. This would likely not be the case for many urban airports, the main airports of concern in a pollution study. In addition, the average vegetation temperature (283 [K]) is warmer than the average sky temperature (260 [K]).

A sky background on the other hand, is guaranteed at any airport, as an unobstructed sky is essential for airplane takeoffs. Observing the sky through the plume will enhance the temperature difference and is easily accomplished with a highly reflective plate. The proposed system design is presented in Figure 4.2 (*Objective 2a*).

The main components in Figure 4.2 are the sky (background) radiance, the reflecting plate radiance, and the plume radiance. A small subset of sky photons will reflect off a zinc-coated plate and pass through the plume before transmitting to the sensor. A 12"×18" zinc-coated plate was chosen due to its high reflectivity and low emissivity in the infrared regime. This ensures that the majority of photons coming from the plate will be sky reflections, and not self-emission from the plate.

As in the gaseous effluent model presented in §4.1, radiance from small segments of atmosphere will be ignored. In the first model, this was L_b, the portion of atmosphere between the plume and the ground. In the current model, radiance generated by the atmosphere between the plate and plume, and the plume and camera will be ignored. However, short-distance transmission effects are taken into account, denoted by τ_{10} and τ_{50}, to indicate distances of 10 [m] and 50 [m], respectively. These distances were chosen as the reflective plate can easily stand alone, while the camera may need an operator present. As operators will likely be limited in how close they can stand to a moving airplane, an extended distance of 50 [m] was selected.

In an operational scenario, two cameras will be present, each with a different filter. The difference between the two filters will be used to monitor background levels and plume presence. The next step to model camera observations is to formulate a governing equation for the proposed system, adapted from Equation 4.3.

4.3 System Governing Equation

With the proposed imaging system of §4.2, shown in Figure 4.2, the expected sensor-reaching radiance can be mathematically modeled (*Objective 2b*) as:

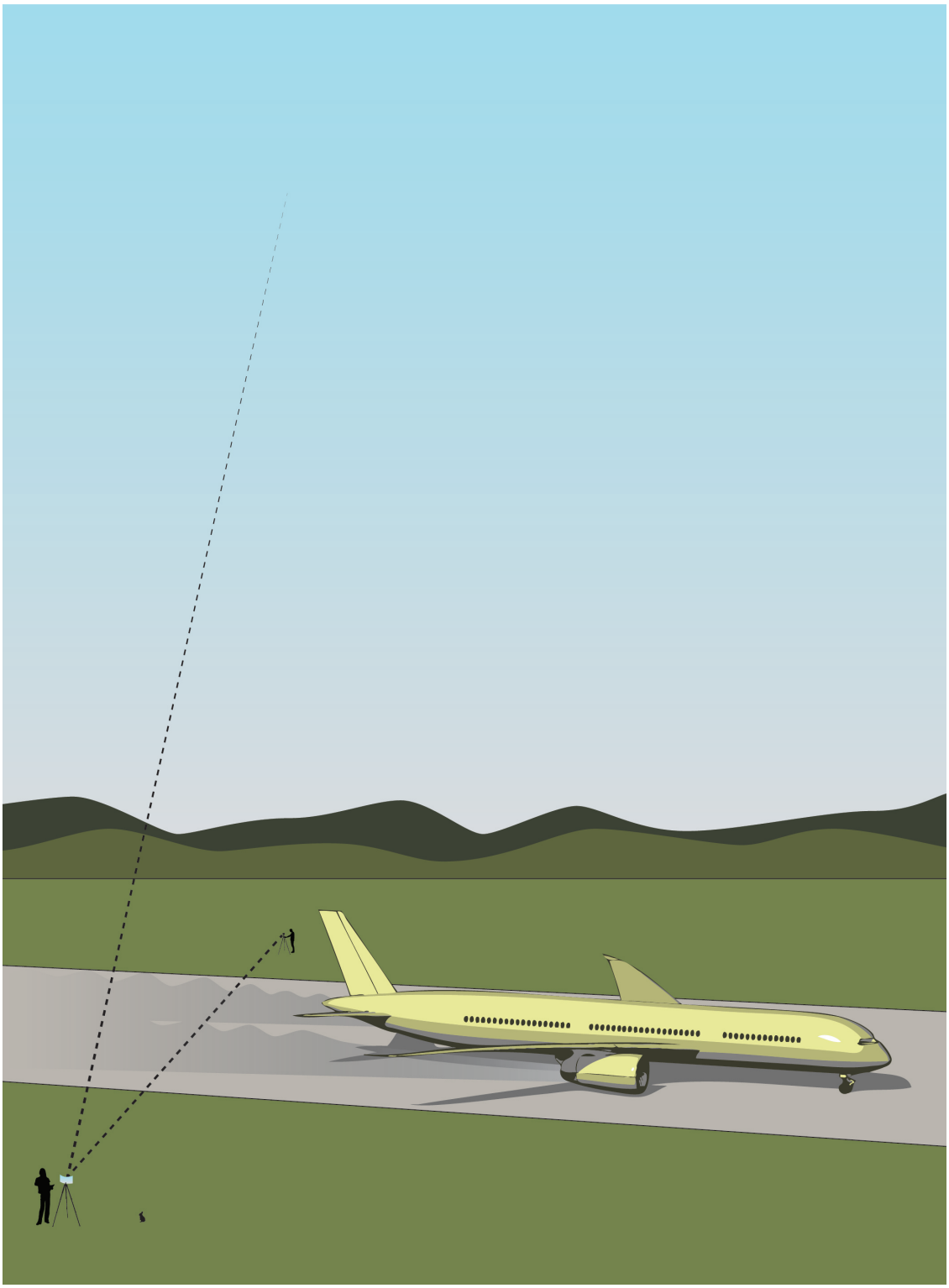

Figure 4.2: Schematic of the proposed imaging system with a ground-based sensor. The sky radiance serves as background and is modified by atmospheric transmission, the reflectivity of a zinc-coated plate, short ground distance atmospheric interference (transmission), and the plume transmission. The plate radiance is modified by its emissivity, the ground distance atmospheric interference, and the plume transmission. The plume radiance is modified by its emissivity and a ground-based atmospheric interference.

$$\begin{aligned} L_{sky}(\lambda) =& \tau_p \tau_{atm} \tau_{10} \tau_{50} B(T_b, \lambda) \rho_{Zn} \\ &+ \tau_p \tau 10 \tau_{50} B(T_{Zn}, \lambda)(1 - \rho_{Zn}) \\ &+ \tau_{50} B(T_p, \lambda)(1 - \tau_p), \end{aligned} \tag{4.5}$$

where

$L_{sky}(\lambda)$ = spectral sensor-reaching radiance,

τ_p = plume transmission,

τ_{atm} = atmospheric transmission,

$\tau_{10,50}$ = ground transmission across 10 and 50 [m] respectively (on each side of the plume),

$B_\lambda(T, \lambda)$ = blackbody radiance obtained through the Planck function,

T_b = sky background temperature (260 [K]),

ρ_{Zn} = reflectivity of a zinc-coated plate,

T_{Zn} = temperature of the zinc-coated plate (295 [K]), and

T_p = exhaust plume temperature (variable).

The three terms in Equation 4.5 represent, in order,

- the sky radiance modified by the atmospheric transmission, the reflectance of the zinc-coated plate, two short-distance atmospheric transmissions, and the plume transmission;
- the plate radiance modified by its emissivity, two short-distance atmospheric transmissions, and the plume transmission;
- and the plume radiance modified by its emissivity and one short-distance atmospheric transmission.

Several key assumptions are made in this governing equation, namely:

1. There are no adjacency effects in the photon path, where photons emit from surrounding objects and into the sensor[53];

2. Scattering and reflection effects due to the plume are minimal; and

3. The sky, zinc-coated plate, and plume can all be modeled as blackbody radiators.

Atmospheric transmissions can be modeled via software (see §7.4), and the reflectivity of the zinc-coated plate has been measured in a laboratory setting. After modeling the atmosphere, plate, and plume as blackbodies, the remaining step is to determine the plume transmission. This is the most difficult aspect of the presented work, and two methods are discussed in Chapter 6. First, however, the unburned hydrocarbons (UHCs) included in the plume model are examined, as they will impact the transmission. This is done in the following chapter.

Chapter 5

Pollutant Phenomenology

Objective 1 was to characterize the pollutant phenomenology of gases present within aircraft exhaust. This was partially discussed in §2.1.3, where the four pollutant categories monitored by the International Civil Aviation Organization (ICAO) were presented, along with a brief argument for targeting unburned hydrocarbons (UHCs) with the imaging system. To reiterate, UHCs are ideal for monitoring exhaust plumes due to their strong absorption features in the far infrared, where inexpensive cameras can be purchased commercially. In the previous chapter, the emissive nature of this problem was discussed and why the plume requires infrared observations in the first place, rather than the optical portion of the electromagnetic spectrum.

A future step in the design of our imaging system will be to select two filters with which to track total UHCs in the plume. Individual plume constituents can also be monitored by selecting narrow band filters based on their prominent absorption features. Plume transmission is inversely related to pollutant absorption, so stronger absorption features will increase plume detectability.

There are numerous available libraries for vapor-phase infrared spectra of pure materials[54–56]. In particular, the National Institute of Standards and Technology (NIST) and the Pacific Northwest National Laboratory (PNNL) have both developed an infrared spectral database with accurate absorbance and frequency values, documented sample purity, and high spectral resolution (0.1 [cm^{-1}], or roughly 0.1 [nm] to 3 [nm], depending on wavelength). Both NIST and PNNL used a Bruker-66v vacuum bench Fourier trans-

form infrared spectroscopy (FTIR) system, but their methods of sample preparation and sample delivery are significantly different. This allowed the measured absorption spectra to be checked for consistency[54]. Comparisons were made by integrating specific band regions of 12 different chemicals, and excluding three of the 26 bands under study, all percent differences in area was under 2%. We proceed under the assumption that the measured absorption spectra are accurate and examine the spectral features of plume constituents using the PNNL database.

The width of these features varies as a function of pressure and temperature however, and this needs to be taken into account when selecting filters. The absorption line width varies as

$$\Delta\sigma = \Delta\sigma_0 \left(\frac{P}{P_0}\right) \left(\frac{T_0}{T}\right)^n, \tag{5.1}$$

where $\Delta\sigma_0$ is the line width at standard atmospheric pressure and temperature ($T_0 = 273$ [K] and $P_0 = 1000$ [mbar]). The exponent n is empirically derived (nominally 0.5)[52]. As the ambient temperature T increases, the line width will broaden (Equation 5.1). In a dynamic sense, broad absorption line widths are expected near the jet engine exit, and narrowed line widths are expected as the plume temperature decreases to ambient levels.

Although this study primarily targets UHCs, all plume constituents will effect the plume transmission, so absorption profiles are presented for CO_x and NO_x as well (Figures 5.1 - 5.4). The effects of pressure broadening are minimal when comparing absorption spectra measured at 50° [C] (323 [K]) versus spectra measured at 5° [C] or 25° [C].

As mentioned in §2.1.3, almost all absorption features for CO_x and NO_x are in the midwave infrared (MWIR) (up to 8 [μm]), where there are no commercially available inexpensive cameras. In addition, longwave infrared (LWIR) camera sensitivity tends to drop off after 14 [μm], preventing observations of the LWIR CO_2 feature from 14 - 16 [μm] (Figure 5.2). Thus the search for observable absorption features is focused on the 8 - 14 [μm] range.

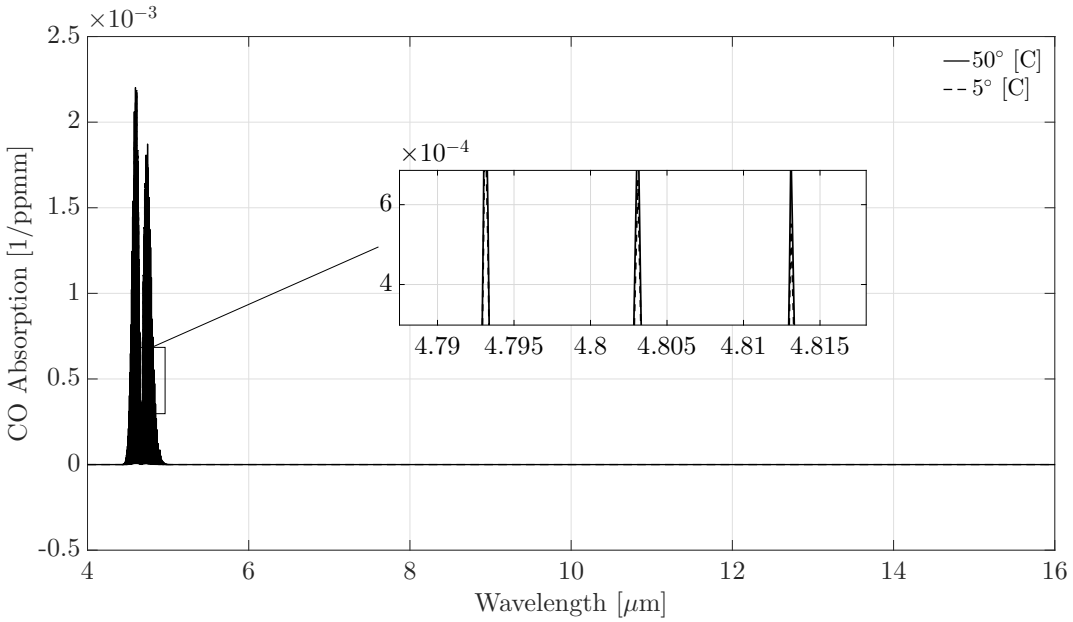

Figure 5.1: Absorption spectrum for carbon monoxide at 50° [C] (323.15 [K]) and 5° [C] (278.15 [K]). The minimal effects of pressure broadening are shown in the magnified inset.

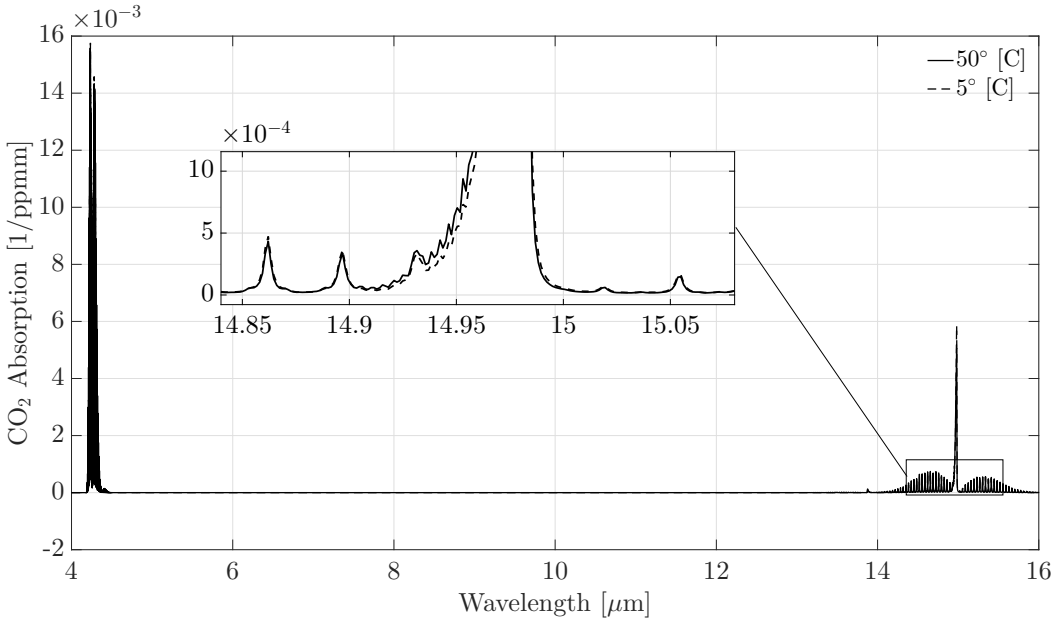

Figure 5.2: Absorption spectrum for carbon dioxide at 50° [C] (323.15 [K]) and 5° [C] (278.15 [K]). The minimal effects of pressure broadening are shown in the magnified inset.

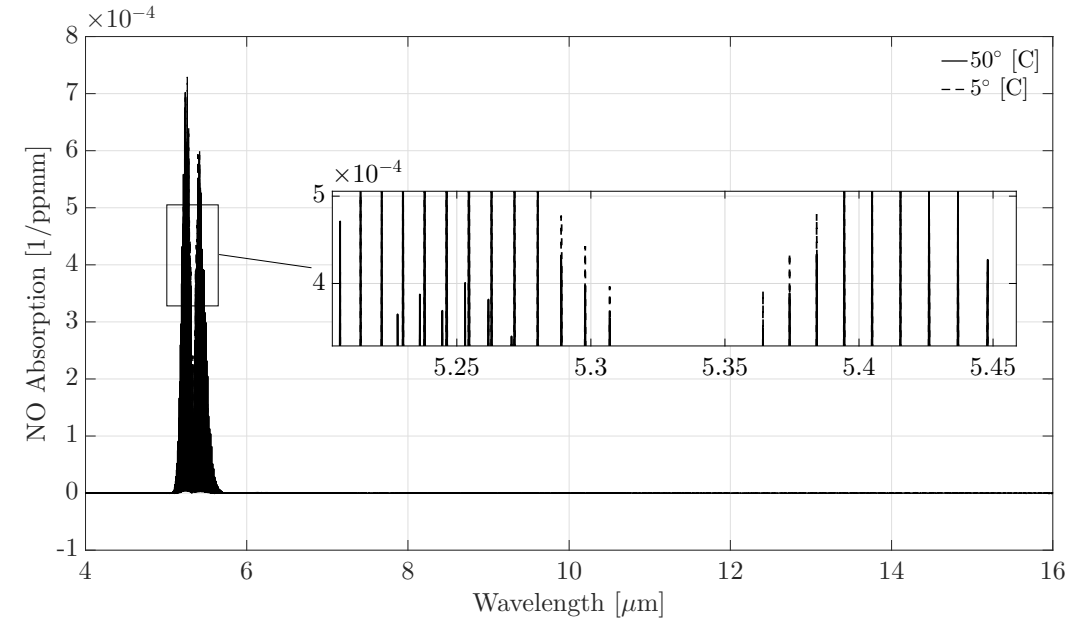

Figure 5.3: Absorption spectrum for nitrous oxide at 50° [C] (323.15 [K]) and 5° [C] (278.15 [K]). The minimal effects of pressure broadening are shown in the magnified inset.

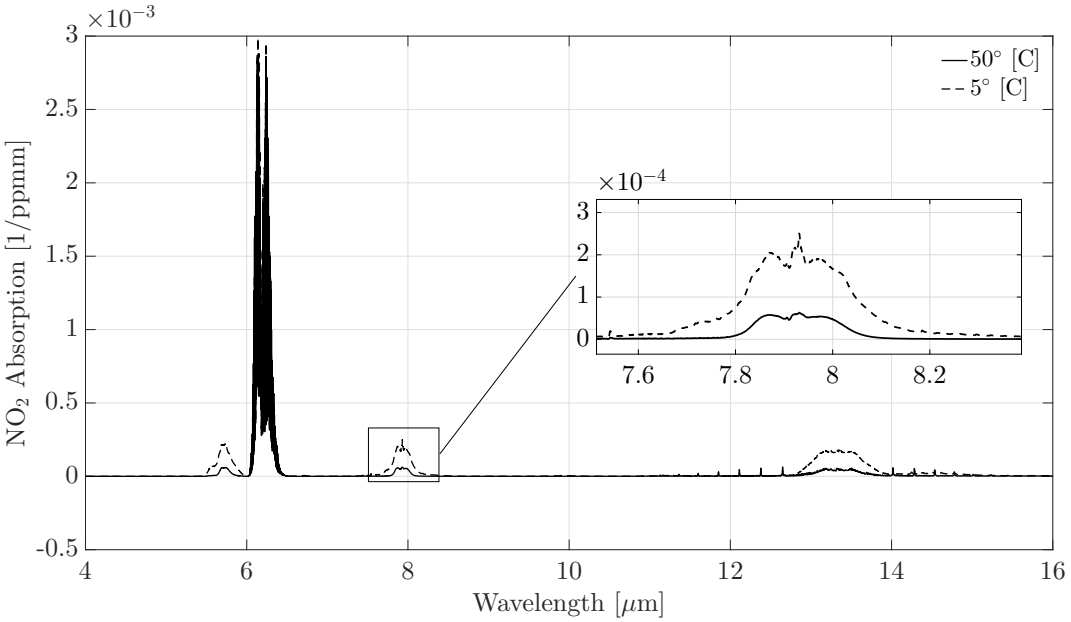

Figure 5.4: Absorption spectrum for nitrogen dioxide at 50° [C] (323.15 [K]) and 5° [C] (278.15 [K]). The minimal effects of pressure broadening are shown in the magnified inset.

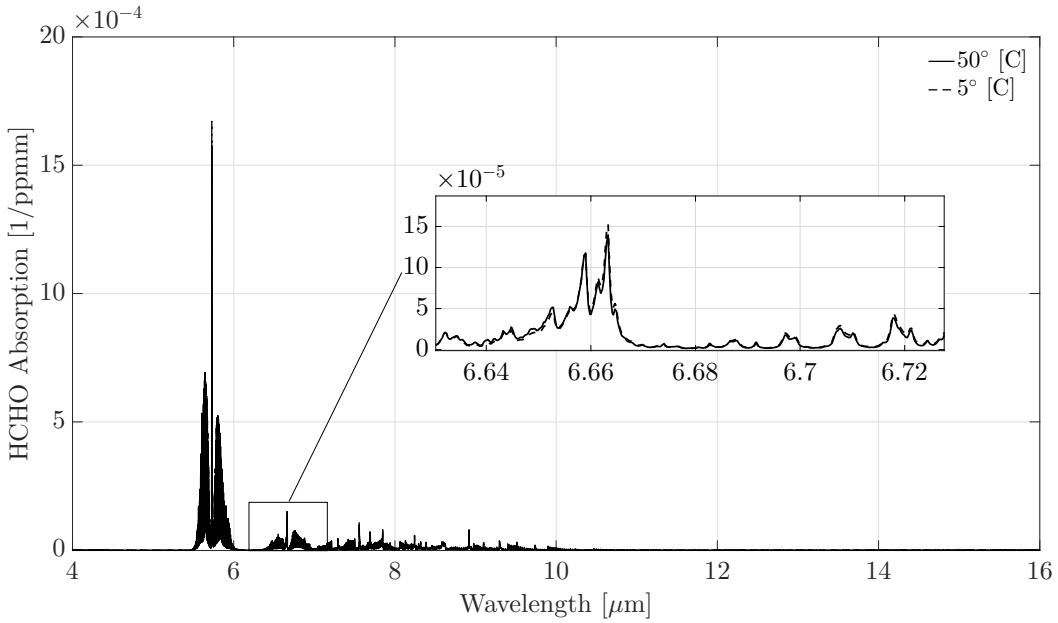

Figure 5.5: Absorption spectrum for formaldehyde at 50° [C] (323.15 [K]) and 5° [C] (278.15 [K]). The minimal effects of pressure broadening are shown in the magnified inset.

Nineteen UHCs were considered as plume constituents in this study (Figures 5.5 - 5.23). Unlike CO_x and NO_x, many prominent UHC features are seen in the LWIR (*Objective 1a*). Note that the strong absorption features seen in benzene (Figure 5.13) and toluene (Figure 5.14) are mostly undetectable given the poor camera sensitivity at longer wavelengths. As expected based on Equation 5.1, gases at greater temperatures exhibit broader line widths. However, these changes are only seen at very small scales and are not predicted to have any effect on future radiometric predictions (Chapter 7). The capacity to detect and track individual UHC levels is further discussed in Chapter 8.

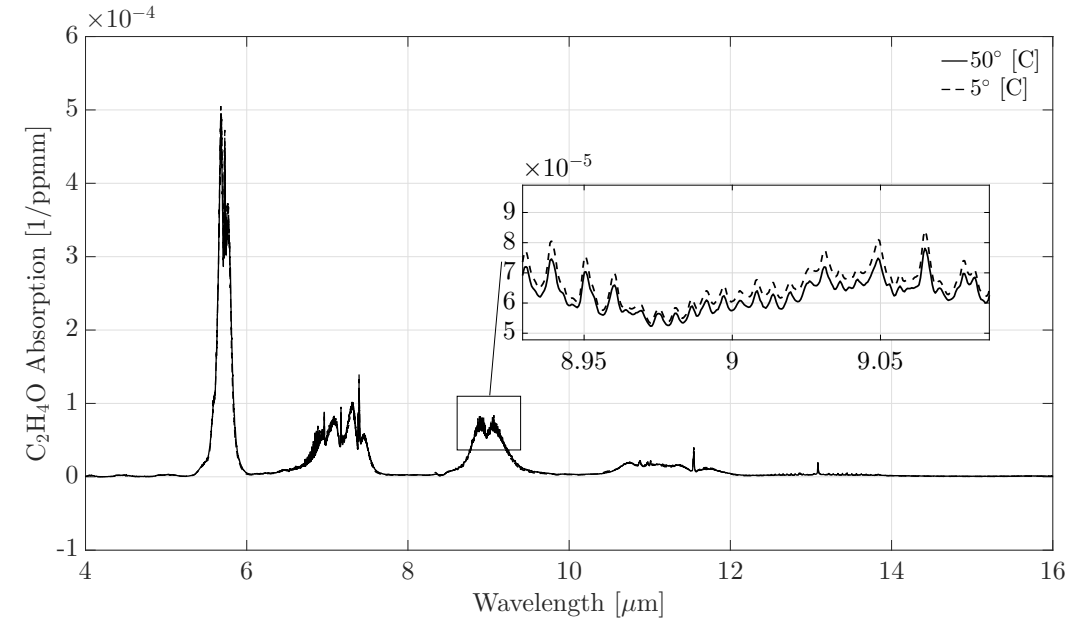

Figure 5.6: Absorption spectrum for acetaldehyde at 50° [C] (323.15 [K]) and 5° [C] (278.15 [K]). The minimal effects of pressure broadening are shown in the magnified inset.

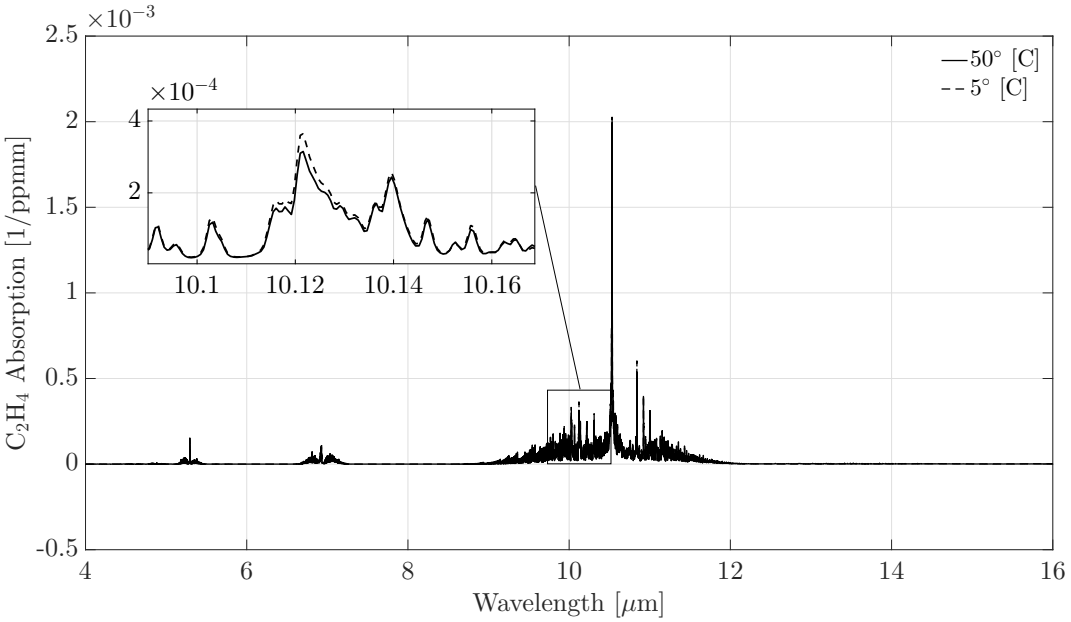

Figure 5.7: Absorption spectrum for ethylene at 50° [C] (323.15 [K]) and 5° [C] (278.15 [K]). The minimal effects of pressure broadening are shown in the magnified inset.

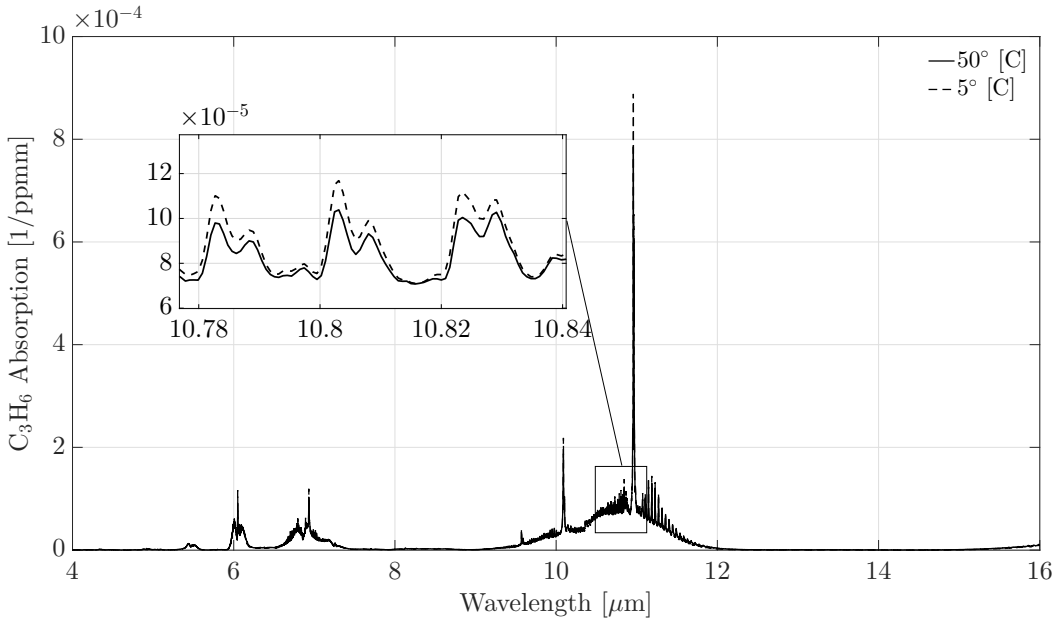

Figure 5.8: Absorption spectrum for propene at 50° [C] (323.15 [K]) and 5° [C] (278.15 [K]). The minimal effects of pressure broadening are shown in the magnified inset.

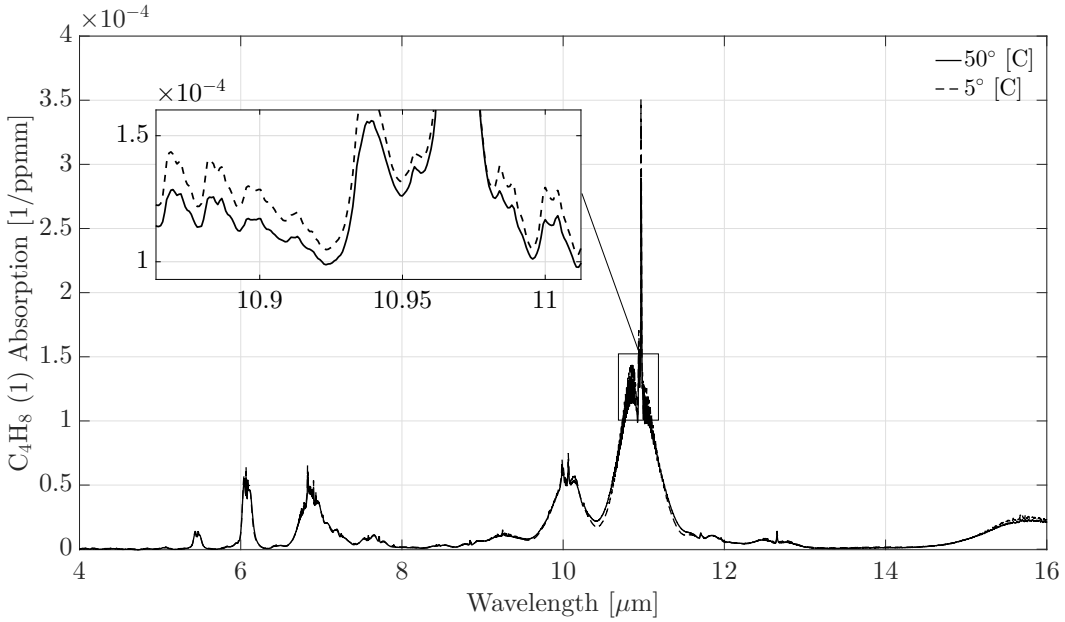

Figure 5.9: Absorption spectrum for butene-1 at 50° [C] (323.15 [K]) and 5° [C] (278.15 [K]). The minimal effects of pressure broadening are shown in the magnified inset.

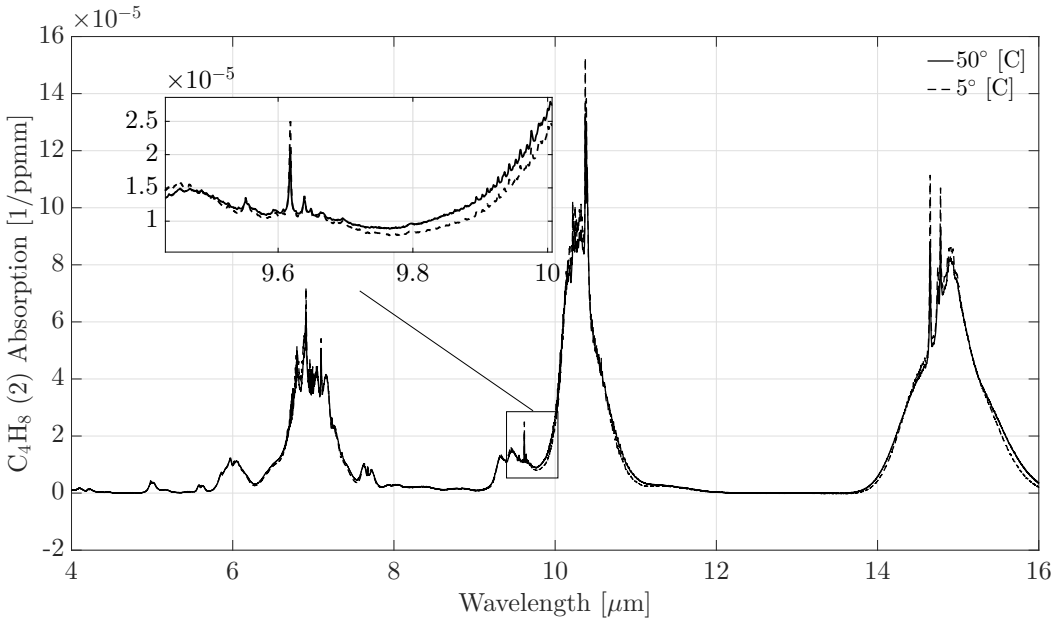

Figure 5.10: Absorption spectrum for butene-2 at 50° [C] (323.15 [K]) and 5° [C] (278.15 [K]). The minimal effects of pressure broadening are shown in the magnified inset.

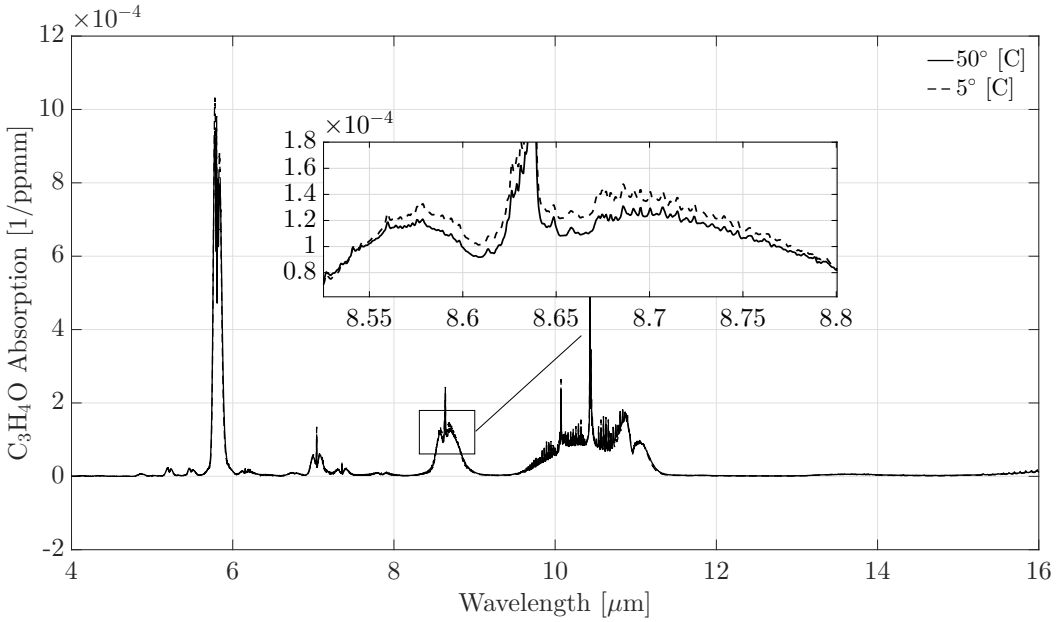

Figure 5.11: Absorption spectrum for acrolein at 50° [C] (323.15 [K]) and 5° [C] (278.15 [K]). The minimal effects of pressure broadening are shown in the magnified inset.

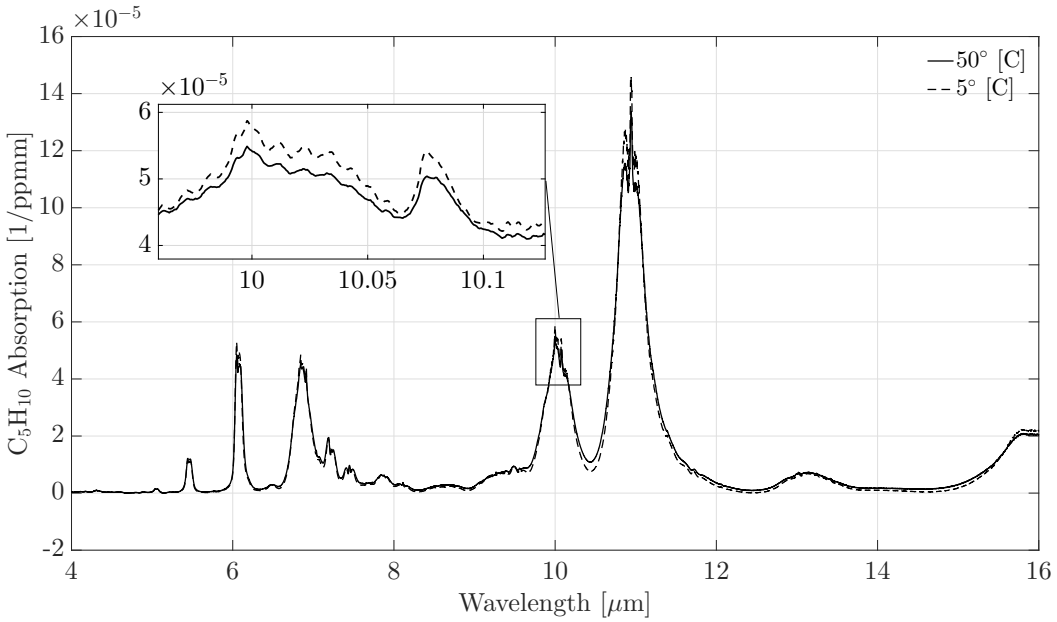

Figure 5.12: Absorption spectrum for pentene at 50° [C] (323.15 [K]) and 5° [C] (278.15 [K]). The minimal effects of pressure broadening are shown in the magnified inset.

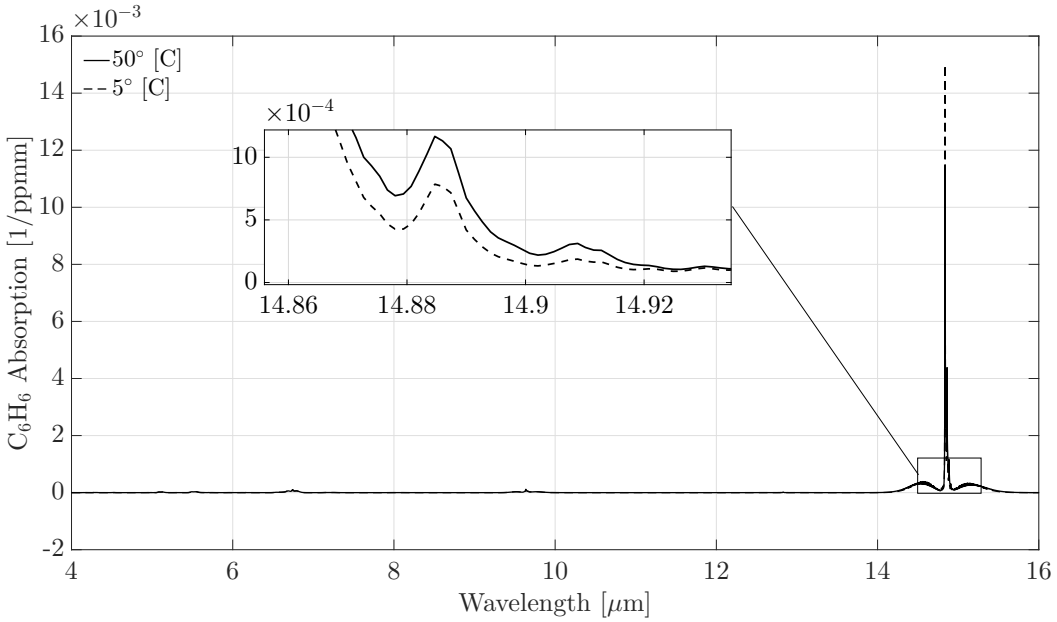

Figure 5.13: Absorption spectrum for benzene at 50° [C] (323.15 [K]) and 5° [C] (278.15 [K]). The minimal effects of pressure broadening are shown in the magnified inset.

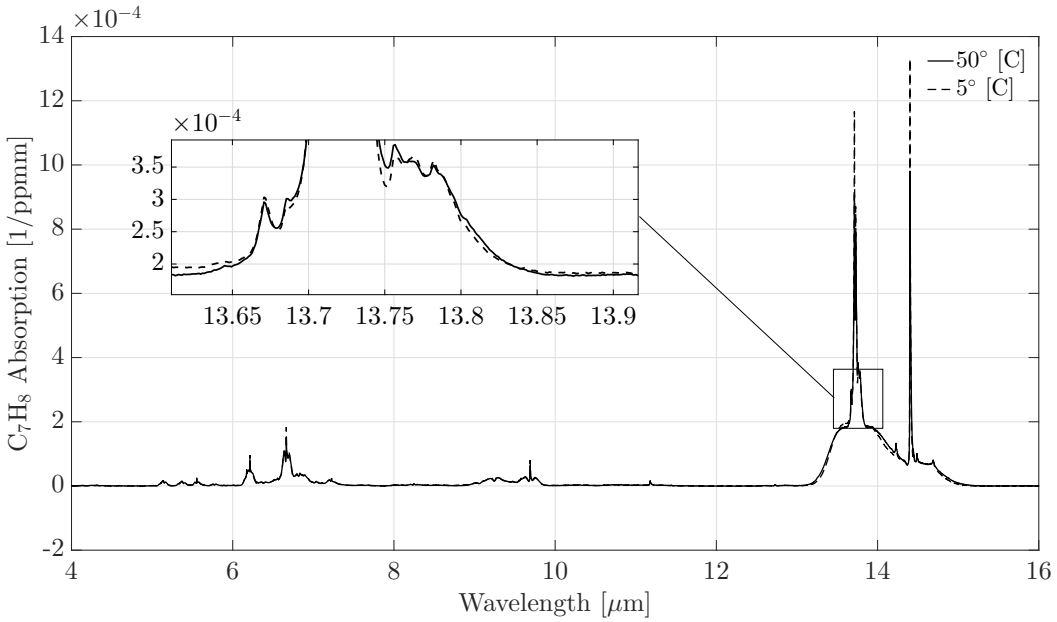

Figure 5.14: Absorption spectrum for toluene at 50° [C] (323.15 [K]) and 5° [C] (278.15 [K]). The minimal effects of pressure broadening are shown in the magnified inset.

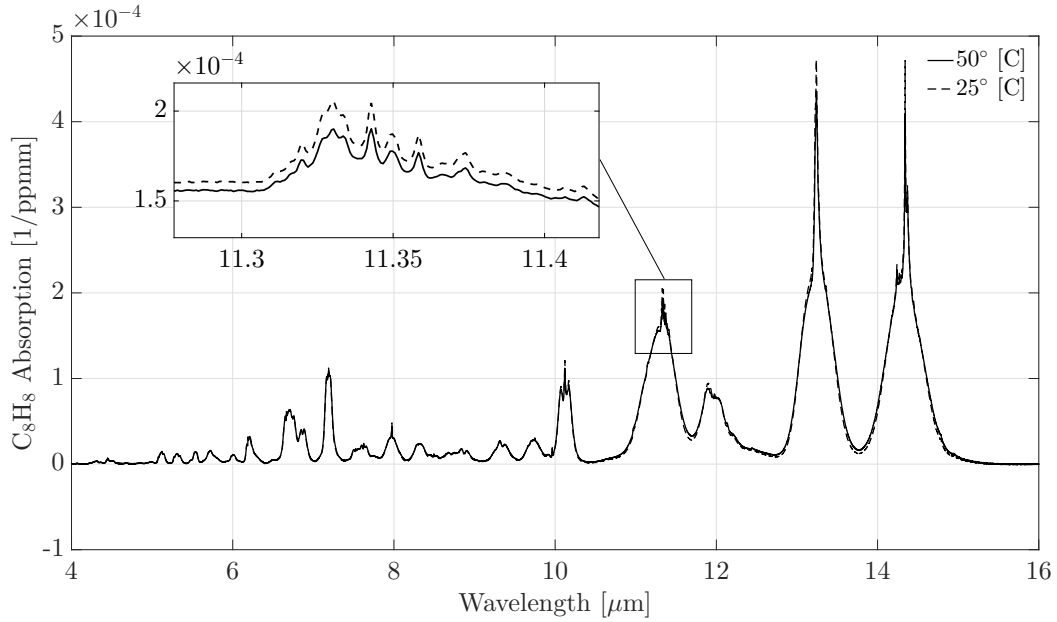

Figure 5.15: Absorption spectrum for styrene at 50° [C] (323.15 [K]) and 25° [C] (298.15 [K]). The minimal effects of pressure broadening are shown in the magnified inset.

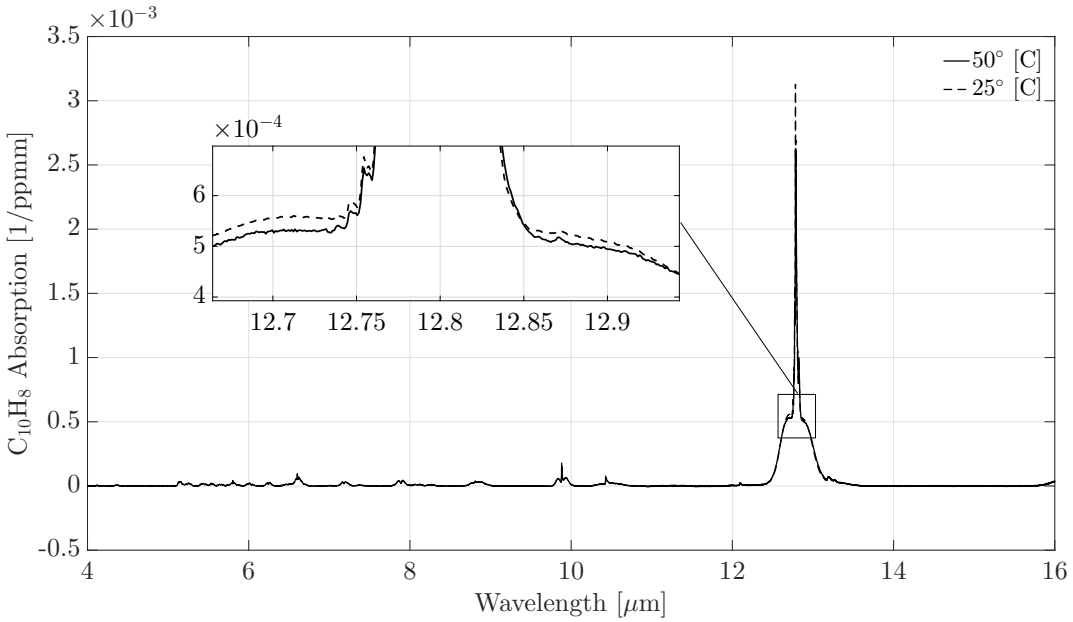

Figure 5.16: Absorption spectrum for naphthalene at 50° [C] (323.15 [K]) and 25° [C] (298.15 [K]). The minimal effects of pressure broadening are shown in the magnified inset.

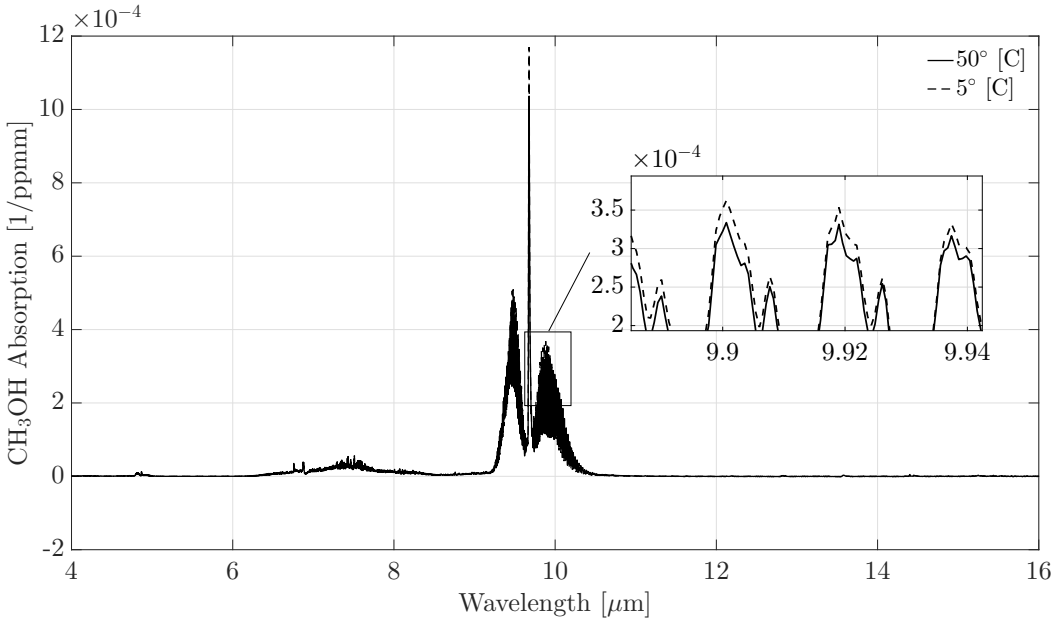

Figure 5.17: Absorption spectrum for methanol at 50° [C] (323.15 [K]) and 5° [C] (278.15 [K]). The minimal effects of pressure broadening are shown in the magnified inset.

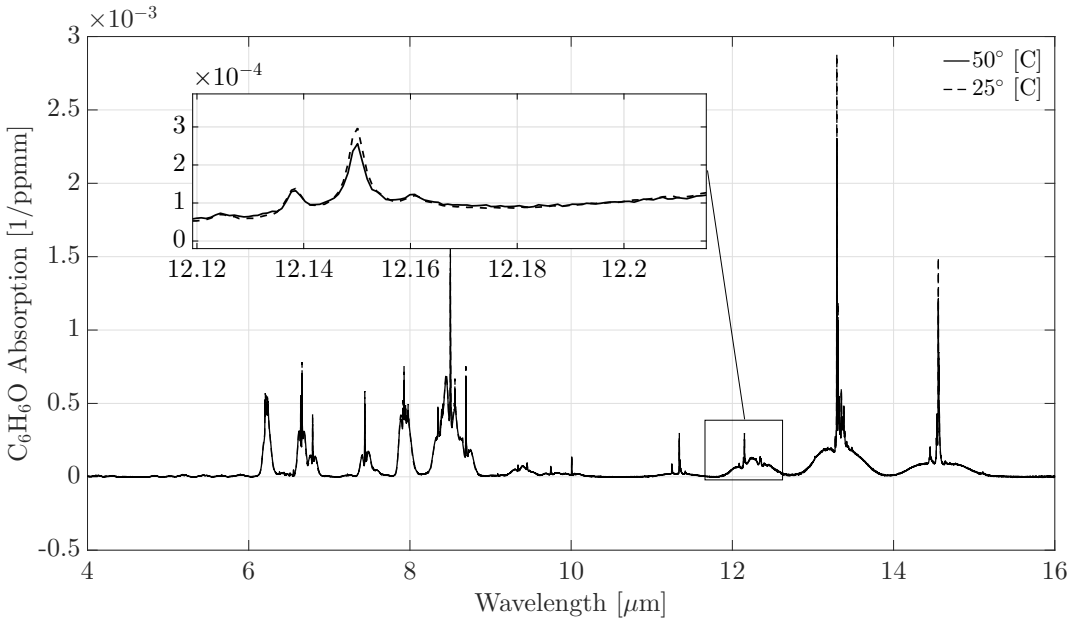

Figure 5.18: Absorption spectrum for phenol at 50° [C] (323.15 [K]) and 25° [C] (298.15 [K]). The minimal effects of pressure broadening are shown in the magnified inset.

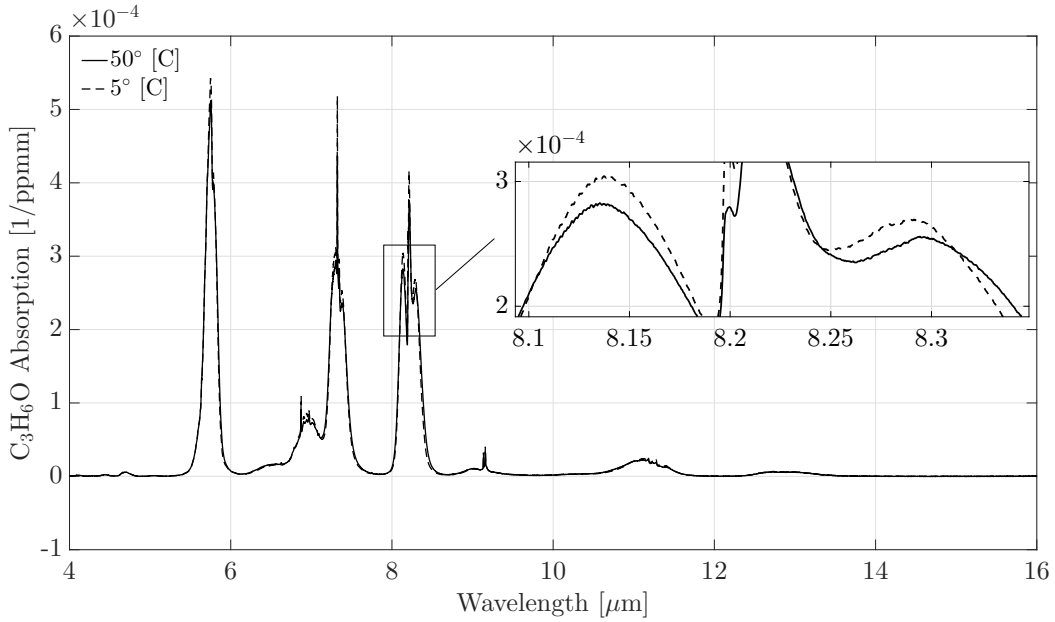

Figure 5.19: Absorption spectrum for acetone at 50° [C] (323.15 [K]) and 5° [C] (278.15 [K]). The minimal effects of pressure broadening are shown in the magnified inset.

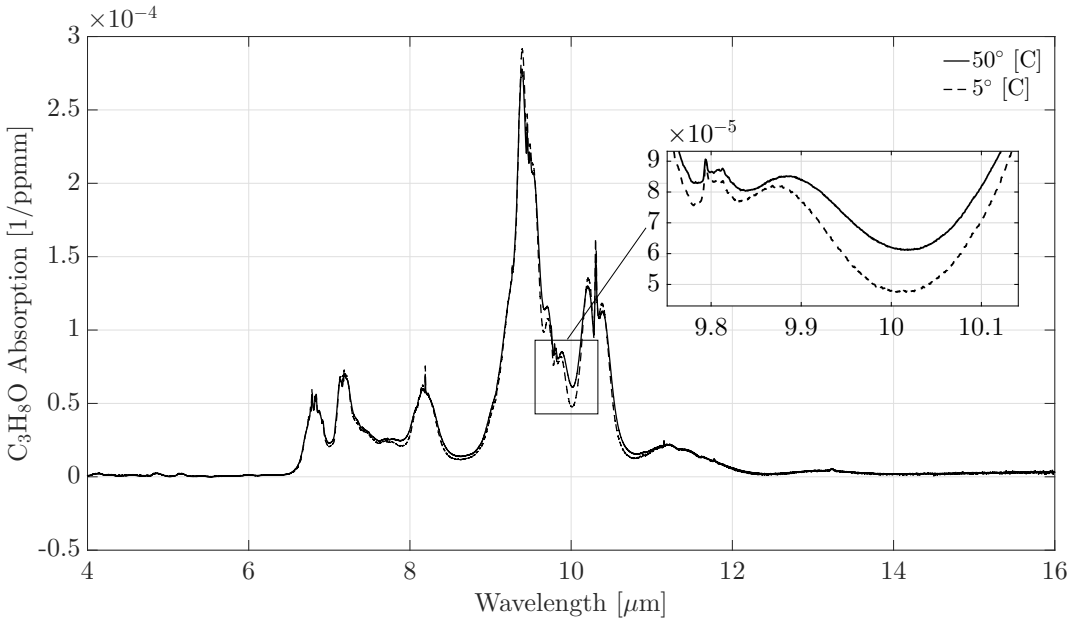

Figure 5.20: Absorption spectrum for propanal at 50° [C] (323.15 [K]) and 5° [C] (278.15 [K]). The minimal effects of pressure broadening are shown in the magnified inset.

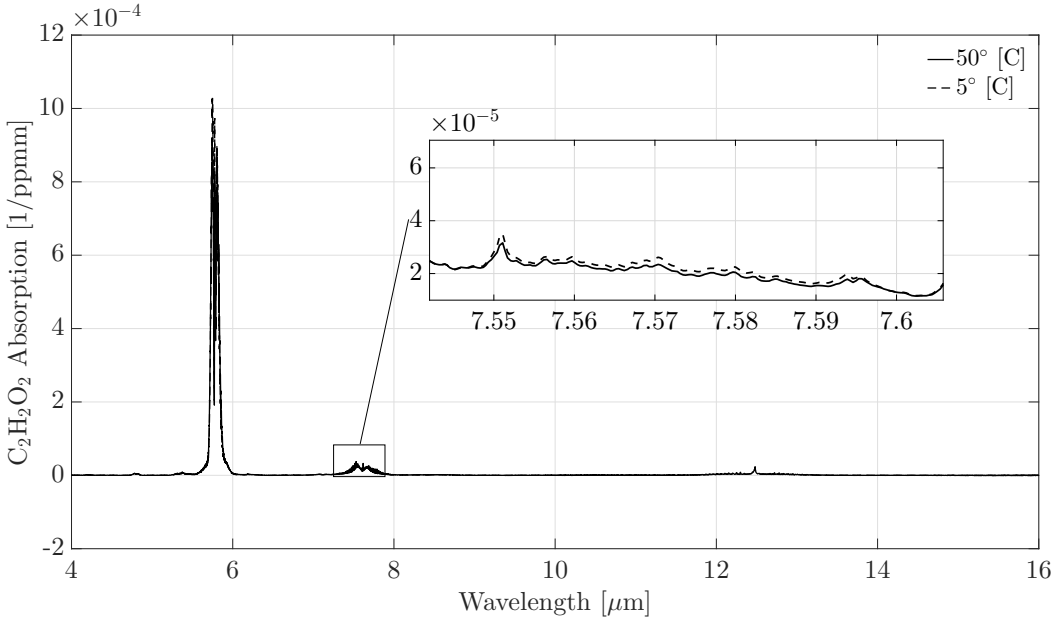

Figure 5.21: Absorption spectrum for glyoxal at 50° [C] (323.15 [K]) and 5° [C] (278.15 [K]). The minimal effects of pressure broadening are shown in the magnified inset.

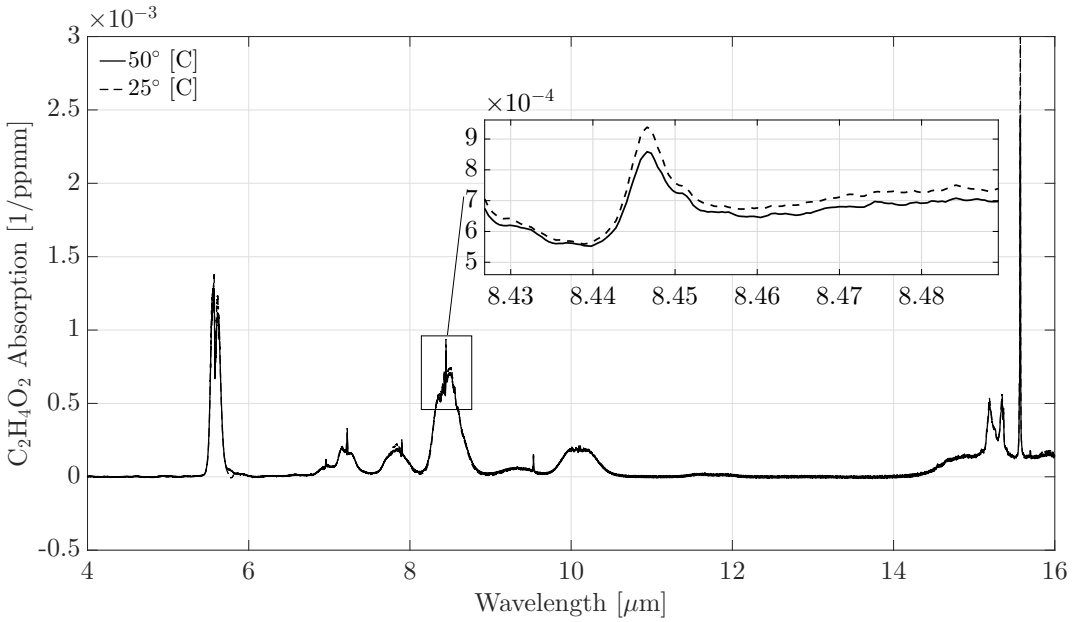

Figure 5.22: Absorption spectrum for acetic acid at 50° [C] (323.15 [K]) and 25° [C] (298.15 [K]). The minimal effects of pressure broadening are shown in the magnified inset.

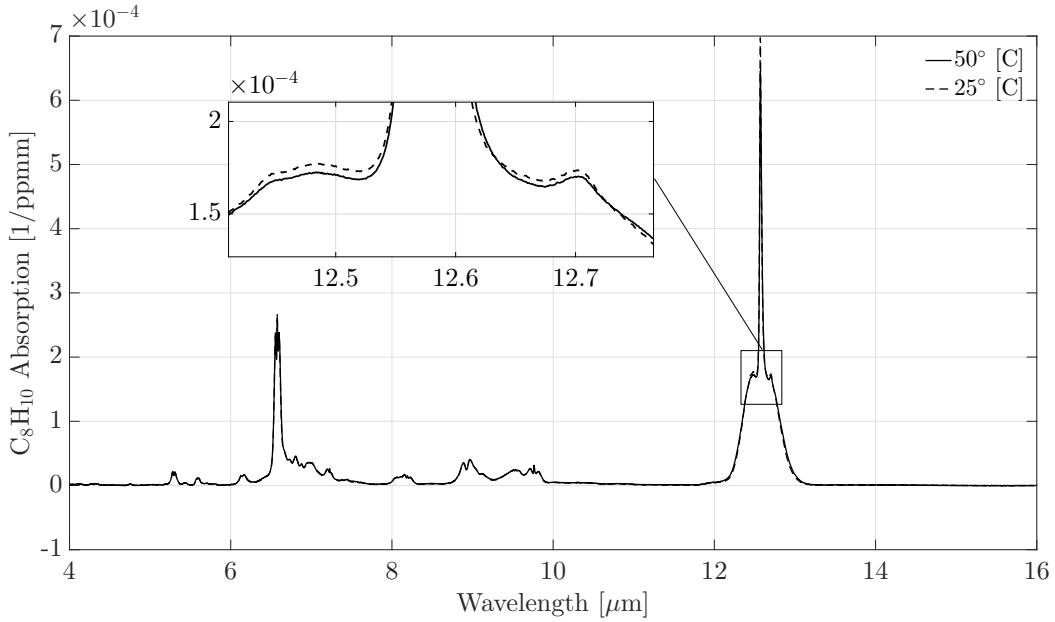

Figure 5.23: Absorption spectrum for p-xylene at 50° [C] (323.15 [K]) and 25° [C] (298.15 [K]). The minimal effects of pressure broadening are shown in the magnified inset.

Chapter 6

Concentration Modeling Methods

Chapter 4 concluded by stating that determining the plume transmission would be the most difficult step in modeling the plume radiometry. The plume transmission will depend on the absorption spectra of individual constituents, the plume width, and the concentration of each constituent (see §7.2). Precise absorption spectra, measured in a laboratory setting, were presented in Chapter 5. The goal is then to correctly model the plume width and concentration.

It is useful to first establish a common geometry for 3-dimensional plume models. This is presented in Figure 6.1, where $E1$ and $E2$ represent two jet engines. The x-axis is commonly referred to as the downwind distance, the y-axis as the crosswind distance, and the z-axis as the vertical distance.

Through the course of this study the plume concentration was modeled with two different methods: the Ideal Gas Law and the Gaussian Plume Equation. Both methods, and their advantages and disadvantages, are presented in this chapter (*Objective 2c*).

6.1 Ideal Gas Law

This study began by using the Ideal Gas Law to model the concentration of unburned hydrocarbons (UHCs) constituents within the plume. The basic premise of this approach was to estimate the amount of emitted UHC molecules over one meter of travel, and divide that by the number of air molecules in a plume volume of

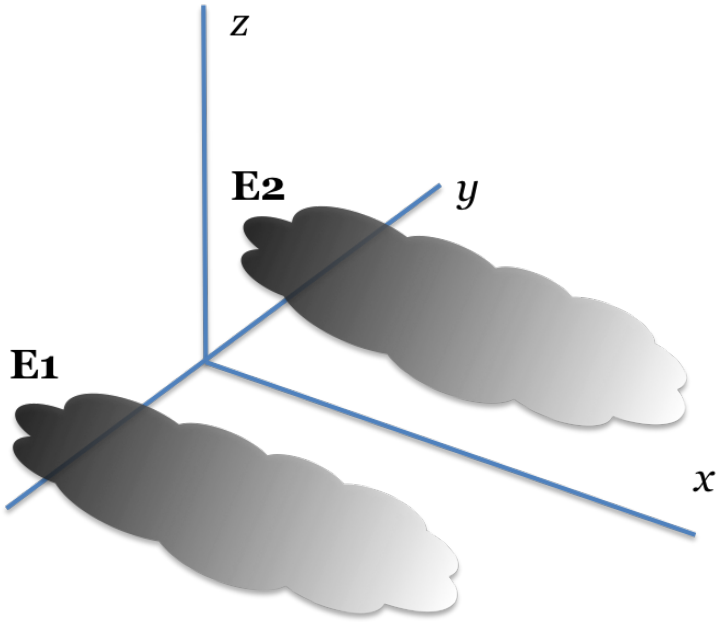

Figure 6.1: Axes definitions for 3-D plume modeling. The x-axis is referred to as the "downwind" or "downstream" axis; the y-axis as the "crosswind" direction (which two aircraft engines lie on, $E1$ and $E2$), and the z-axis as the vertical direction.

the same width under ambient conditions. This gave a concentration estimation in parts-per-million (ppm) which would later be used in transmission estimates.

A typical engine used for Boeing 737 (B737) aircraft was examined, the CFM56-7B22. This engine has a UHC pollutant emission index (EI) of 2.5 [g/kg] and a fuel flow (FF) of 0.105 [kg/s], which equates to an emission rate of 0.2625 [g/s][20]. Assuming an average taxi speed of 7.7 [m/s], the engine emits 0.0341 [g/m] UHCs. The number of UHC molecules can be determined as

$$N = \frac{m}{M} N_a, \tag{6.1}$$

where m is the mass of emitted UHCs (0.0341 [g] for an engine that has traveled one meter), M [g/mol] is the molar mass of UHCs (defined by the International Civil Aviation Organization (ICAO) as that of methane, 16.04 [g/mol][18]), and N_a is Avogadro's number (6.022×10^{23} [1/mol]). These values indicated that the engine would release about 1.28×10^{21} molecules of UHCs for every meter of travel.

To determine the number of air molecules in comparison to the amount of UHCs, the Ideal Gas Law was used, expressed as

$$PV = nRT, \tag{6.2}$$

where P is the pressure in [Pa], V is the volume in [m^3], n is the number of moles of the gas under consideration, R is the Ideal Gas Constant (8.314 [J·$mol^{-1}K^{-1}$]), and T is the temperature [K]. The number of moles n is the parameter of interest, as that can be converted into a number of air molecules N_{UHC} with Avogadro's number:

$$N_{UHC} = \frac{PV}{RT} \times N_a. \tag{6.3}$$

In Equation 6.3, the temperature was assumed to be ambient (307 [K] during the time of Boeing observations), and the pressure was also assumed to be ambient, as one of the main functions of an ideal exhaust nozzle is to match atmospheric pressure and exit pressure as closely as possible[57].

R is a known value, so only the volume of the plume required estimation. Because the UHC emissions were measured as grams-per-meter, the volume was partitioned into sections with one-meter widths. Boeing point measurements of the plume width for an idling B737 were used to predict the plume width as a function of downwind distance (Figure 6.2)[58]. With this, the plume volume partitions were estimated as a function of downwind distance from the engine.

Once the plume volume was modeled, the number of UHC molecules was divided by the number of air molecules and scaled by 10^6 to estimate a concentration η. This is written in ppm as

$$\eta = \frac{N_{UHC}}{N_{air}} \times 10^6 = \frac{N_{UHC} PV}{RTN_a} \times 10^6, \tag{6.4}$$

and provides a model of UHC concentration as a function of downwind distance. Multiplying by two accounts for both engines on a B737, and this measure was converted to a concentration-path-length (CPL) by multiplying by 3.05 meters (a representation of an average plume width). The final model of downwind CPL is presented in Figure 6.3, where the dashed line shows the estimated concentration, and the solid line

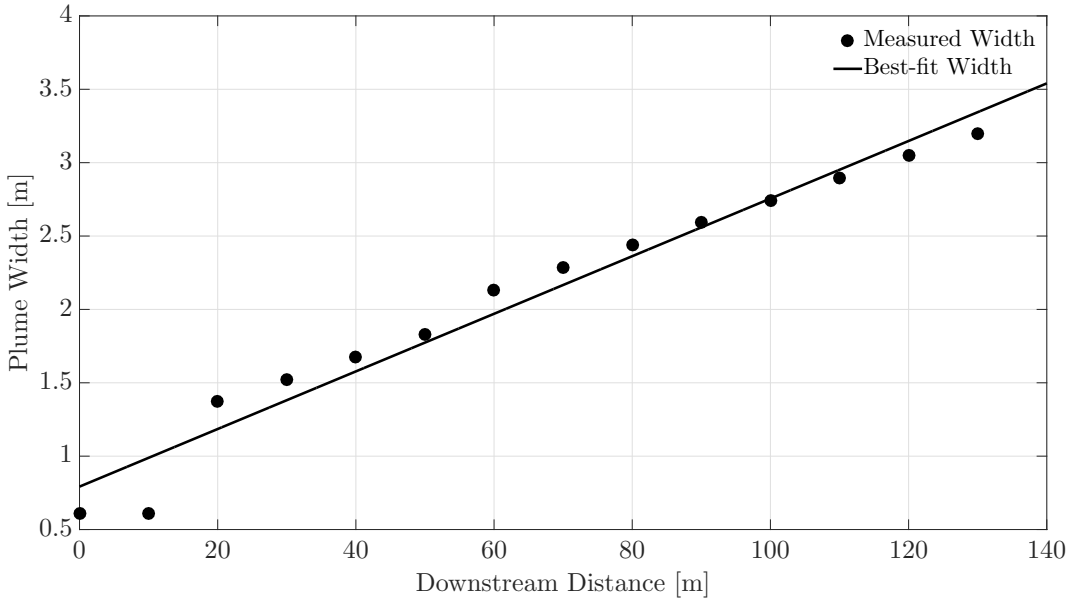

Figure 6.2: Plume width at engine idle, modeled using data from Boeing[58]. Boeing measurements are shown as points and the best fit plume width as the solid black line.

shows the best fit decaying exponential.

This, in essence, represents an instantaneous plume snapshot of how an unmoving idle plume would appear. An extra step is to account for the motion of the airplane. This is similar to a series of plume snapshots being stacked, also understood as integrating the concentration model. The integrated model of CPL, for two engines, is shown in Figure 6.4. At this stage, a temporal dispersion factor is required for our model, as the CPL will not continue to grow unbounded. However, this step is left for the next section, where the Gaussian plume model is presented.

The study moves to Gaussian plumes for a number of reasons. First and foremost, the Ideal Gas Law is meant to be used for closed systems, a criteria which exhaust plumes do not meet. Secondly, there is no physical understanding of dispersion in this model. This is simplistically taken into account by dividing by larger volumes of air as the plume width increases. Additionally, the model assumes a common plume width when determining the CPL. The Ideal Gas Law served as a beginning with which to better understand plume dynamics, but the research now turns to the more sophisticated Gaussian plume model.

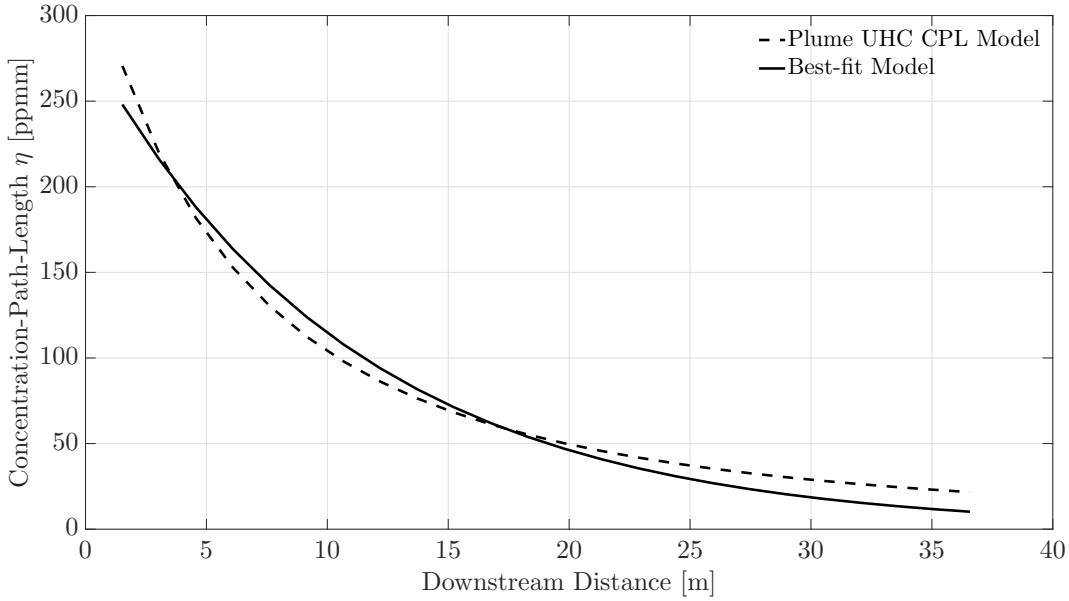

Figure 6.3: Modeled idle plume CPL as a function of downstream distance (dashed line). Best fit decaying exponential model of plume CPL (solid line).

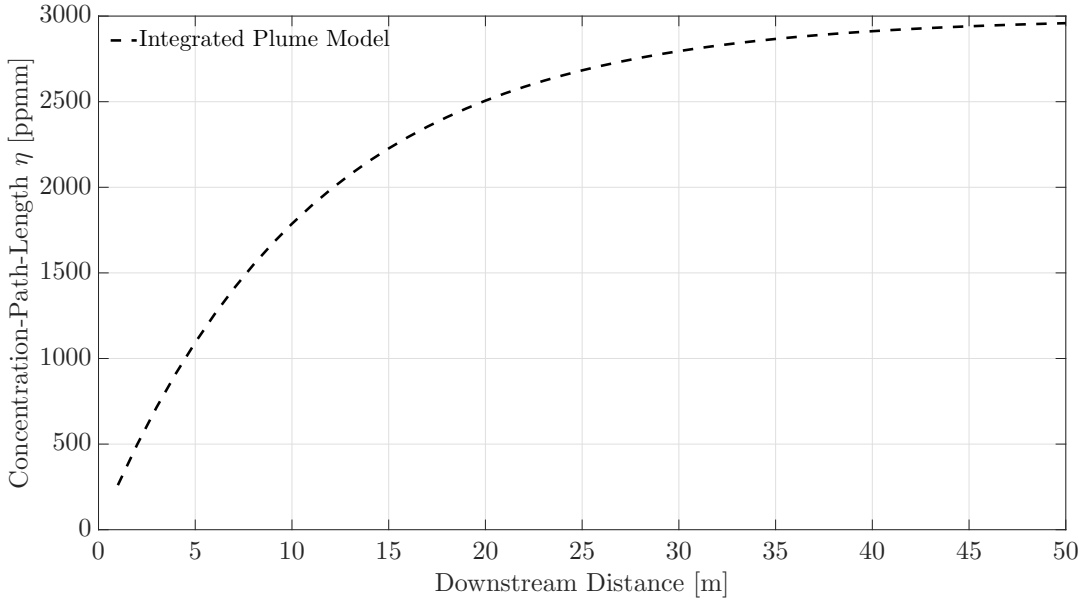

Figure 6.4: Integrated plume concentration-path-length from Figure 6.3, representing the temporal nature of the idle plume.

6.2 Gaussian Plume Model

The Gaussian approach to plume modeling is formulated, starting with an instantaneous "puff" emitted from a point source. In the presence of stationary, homogeneous atmospheric turbulence, the mean concentration of a gaseous species emitted from a point source can be assumed to have a Gaussian distribution[59]. While stationary, homogeneous atmospheric turbulence is exceedingly rare in practice, the assumption is used in a wide variety of atmospheric diffusion models, including the one presented here.

Start by considering a transition probability density (Q) which describes the probability that a gas particle starting at x', y', and z' at time t', will be at x, y, and z at time t. Using the assumption described previously and assuming a wind speed in the x-direction of $\bar{u}$, Q can be written as

$$Q(x,y,z,t|z',y',z',t') = \frac{1}{(2\pi)^{3/2}\sigma_x\sigma_y\sigma_z} \times \exp\left(-\frac{(x-x'-\bar{u}(t-t'))^2}{2\sigma_x^2} - \frac{(y-y')^2}{2\sigma_y^2} - \frac{(z-z')^2}{2\sigma_z^2}\right), \tag{6.5}$$

where the variances σ_x, σ_y, and σ_z are dependent on atmospheric conditions and travel time, or downwind distance from the point source. In Equation 6.5, the z-dimension is assumed to be infinite; no boundary conditions have been applied. Boundary conditions include setting the minimum z-value to 0, to represent the ground; setting a maximum z-value to represent the atmospheric inversion layer; and defining the type of interaction particles will have with the ground (total reflection, total absorption, or partial absorption). The z-dependence can be separated and Equation 6.5 can be written as

$$Q(x,y,z,t|z',y',z',t') = \frac{1}{(2\pi)^{3/2}\sigma_x\sigma_y\sigma_z} \exp\left(-\frac{(x-x'-\bar{u}(t-t'))^2}{2\sigma_x^2} - \frac{(y-y')^2}{2\sigma_y^2}\right) \times Q_z(z,t|z',t'). \tag{6.6}$$

A plume is modeled taking into account the z=0 ground level but the inversion layer is ignored (as we are only concerned with low-level local effects). Total reflection is assumed at the ground. In this case the

z-term in Equation 6.6 becomes

$$Q_z(z,t|z',t') = \frac{1}{(2\pi)^{1/2}\sigma_z}\left[\exp\left(-\frac{(z-z')^2}{2\sigma_z^2}\right) + \exp\left(-\frac{(z+z')^2}{2\sigma_z^2}\right)\right], \tag{6.7}$$

where a second plume is modeled at the same height beneath the surface to account for ground reflections. In this formulation, $(z-h)$ represents the above ground distance from plume to engine, and $(z+h)$ is the below ground distance from the plume to the engine. The probability density Q can be used to model the mean concentration from a continuously emitting point source by integrating over time t:

$$\begin{aligned}\langle c(x,y,z)\rangle = \lim_{t\to\infty}\int_0^t \frac{q}{(2\pi)^{3/2}\sigma_x\sigma_y\sigma_z}\exp\left(-\frac{(x-\bar{u}t')^2}{2\sigma_x^2} - \frac{y^2}{2\sigma_y^2}\right) \\ \times\left[\exp\left(-\frac{(z-h)^2}{2\sigma_z^2}\right) + \exp\left(-\frac{(z+h)^2}{2\sigma_z^2}\right)\right]dt',\end{aligned} \tag{6.8}$$

where q is the source emission rate [kg/s] and h is the source height [m]. The continuous emission is modeled as a series of instantaneous "puffs," which allows us to make use of the slender plume approximation. This assumes that the spread of each puff is small compared to the downwind distance it has traveled since emission, so Equation 6.8 can be evaluated in the limit of $\sigma_x = 0$. In other words, the effects of advection outweigh those of dispersion along the x-axis[60]. Integrating Equation 6.8, provides the standard Gaussian plume equation for a totally reflecting surface at $z = 0$:

$$\begin{aligned}\langle c(x,y,z)\rangle = &\frac{q}{2\pi\bar{u}\sigma_y\sigma_z}\exp\left(-\frac{y^2}{2\sigma_y^2}\right) \\ &\times\left[\exp\left(-\frac{(z-h)^2}{2\sigma_z^2}\right) + \exp\left(-\frac{(z+h)^2}{2\sigma_z^2}\right)\right],\end{aligned} \tag{6.9}$$

where $c(x,y,z)$ is the mean concentration [mg/m^3] at location x, y, z, and $\bar{u}$ is the wind speed in the downwind direction [m/s] (*Objective 2c*).

Equation 2.1 determined the amount of pollutants emitted from a jet engine; it can be modified into a pollutant emission rate, given as

$$R_{ik} = (FF_k) \times (EI_{ik}), \tag{6.10}$$

where R_{ik} is the emission rate in [g/s], FF_k is the fuel flow [kg/s], and EI_{ik} is the EI for a specific pollutant and thrust level [g/kg]. The rate q in Equation 6.9 is obtained by converting R_{ik} to [kg/s].

As mentioned previously, the variances of the Gaussian distributions, σ_y and σ_z, depend on atmospheric turbulence and increase at greater downwind distances (i.e. the plume is more disperse further away from the emission source). Observational studies have helped develop empirical formulas to estimate σ_y and σ_z, commonly in the form of

$$\sigma_y = R_y x^{r_y} \tag{6.11}$$

$$\sigma_z = R_z x^{r_z}, \tag{6.12}$$

where R_y, r_y, R_z, and r_z depend on the atmospheric stability class and observational averaging time. Various values for these parameters have been determined experimentally[61–64]. Atmospheric stability classes are separated into six groups (A - F), moving from extremely unstable to moderately stable[65]. We assume Class C, a slightly unstable atmosphere with a wind speed of $\bar{u} = 3$ [m/s], and we use parameters determined by Klug with an averaging time of ten minutes[64]:

$$R_y = 0.230$$

$$r_y = 0.855$$

$$R_z = 0.076$$

$$r_z = 0.879$$

Equation 6.9 is then used to model the mean concentration levels in a three-dimensional B737 exhaust plume. As in §6.1, the CFM56-7B22 engine is used with an EI of 2.5 [g/kg] and a FF of 0.105 [kg/s],

yielding an emission rate of 0.2625 [g/s]. The model includes two jet engines located along the y-axis at y = -5 and y = +5 (see Figure 6.1). Both jet engines are placed 3.5 [m] off the ground. The average wind speed $\bar{u}$ is set in the x-direction at 3 [m/s] and the atmospheric stability parameters discussed earlier are used. The model output is a concentration map in [mg/m^3].

Modeling the plume transmission requires concentrations to be measured as ppm, or parts-per-million-meter (ppmm). At standard atmospheric pressure and temperature (STP, 100 [kPa] and 298.15 [K]), the concentration c [mg/m^3] is related to the concentration η [ppm] by

$$c = \eta \times \frac{M}{V}, \tag{6.13}$$

where M is the molar mass (16.043 [g/mol] for UHCs in general), and V is the molar volume (24.45 [L]). At temperatures greater than STP however, the molar volume will increase. Charle's Law is used to determine the new molar volume:

$$\frac{V_1}{T_1} = \frac{V_2}{T_2}, \tag{6.14}$$

where V_1 and T_1 are at STP, and T_2 is the plume temperature. V_2 is the volume at temperature T_2, and is used in Equation 6.13. The plume temperature profile was modeled as a function of downwind distance using Boeing point measurements of an idling exhaust plume (Figure 6.5)[58]. The curve was modeled with a decaying exponential and an undefined zero-level, as the ambient temperature during observations was not defined. An ambient temperature of 307 [K] was determined. Equations 6.13 and 6.14 allow the plume concentration η to be modeled three-dimensionally in ppm or the CPL in ppmm.

Figure 6.6 shows a bird's-eye view of the exhaust plumes sliced at z=3.5 [m], the level of the engines (*Objective 2c*). Concentration is expressed as [ppm] with warmer colors indicating higher concentrations. The highest concentration levels drop off slightly before 15 [m] downwind, right before the tail of the aircraft has passed and the camera can begin observations. The plume dissipates quickly, and emissions from both engines combine to create one plume shortly ahead of 10 [m] downwind.

A side view of the plume CPL is also modeled, similar to what we would expect a camera to observe for a stationary idling engine (Figure 6.7). The CPL profile can be drawn at the engine height, z=3.5 [m], for

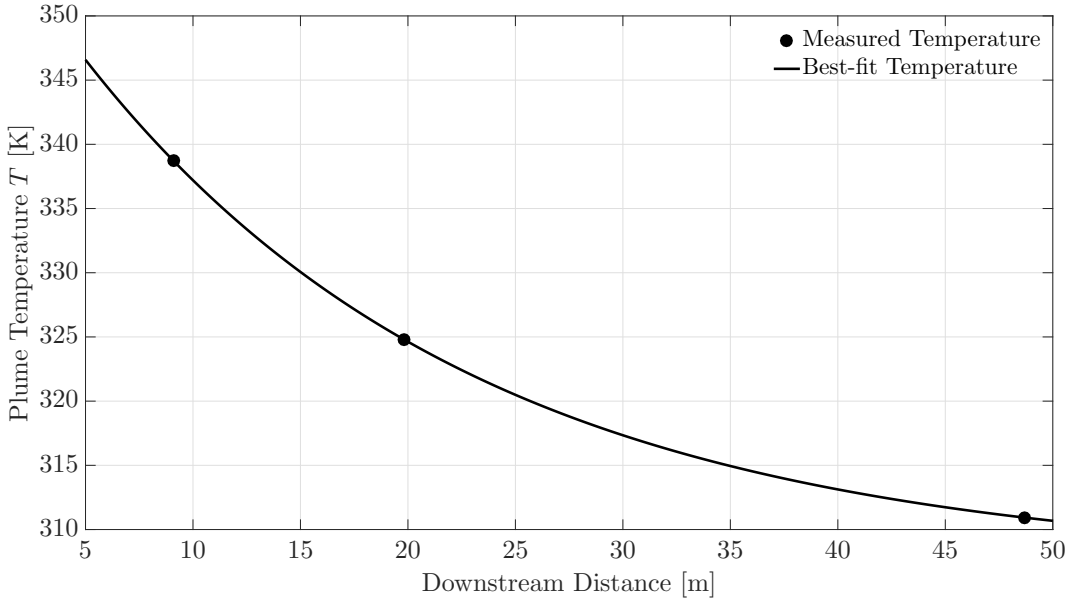

Figure 6.5: Boeing measured temperature of an idling engine[58] (points), and best-fit plume temperature (solid black line).

use in determining plume transmission. This map shows the effects of the total reflection at the ground, as the contours are asymmetric above and below the plume centerline.

Finally, a 3D model of the plume concentration was generated (Figure 6.8). The airplane is centered at y=25, and two jet engines are located at y=20 and y=30. Warmer colors indicate higher concentrations.

There are additional assumptions to be aware of when using the Gaussian plume model. For instance, it is assumed that the pollutant emission rate, q, is constant, which will not be the case if the aircraft changes speed or the ambient temperature changes. It is also assumed that the wind speed is constant with height above the ground, and that the atmospheric turbulence is not greatly varying. Finally, the terrain must be relatively flat for this model to work, although this is not a concern for airport runways.

Despite some simplifications and uncertainties in this model, the Gaussian assumption is well-accepted in the scientific community and it is used in almost all present-day atmospheric dispersion models. It provides a solid starting point with which to model plume concentrations. This model is used in the next chapter to determine the plume transmission.

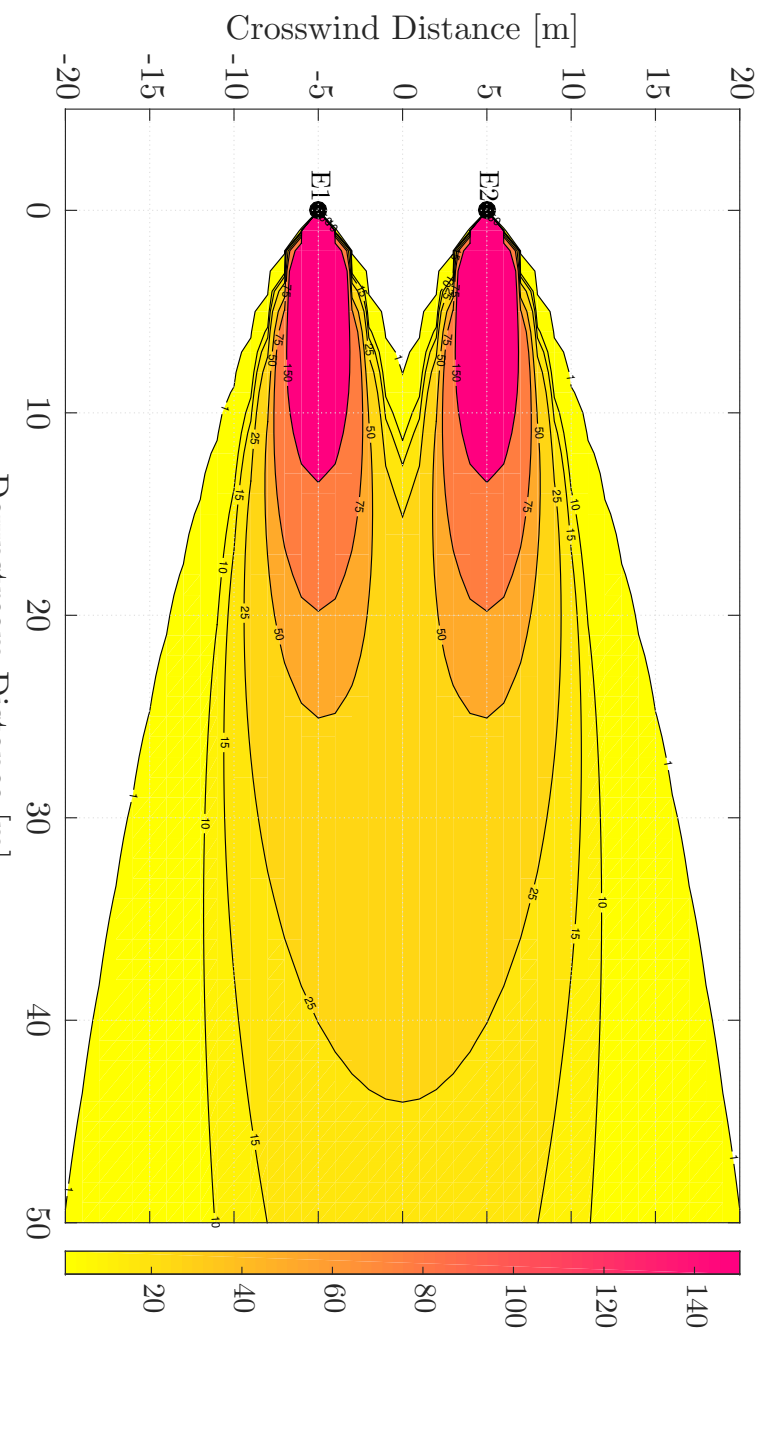

Figure 6.6: Top-down view of plume concentration at z=3.5 [m] (engine level). Contours are shown for two jet engines spaced 10 [m] apart. Hotter colors indicate higher plume concentrations.

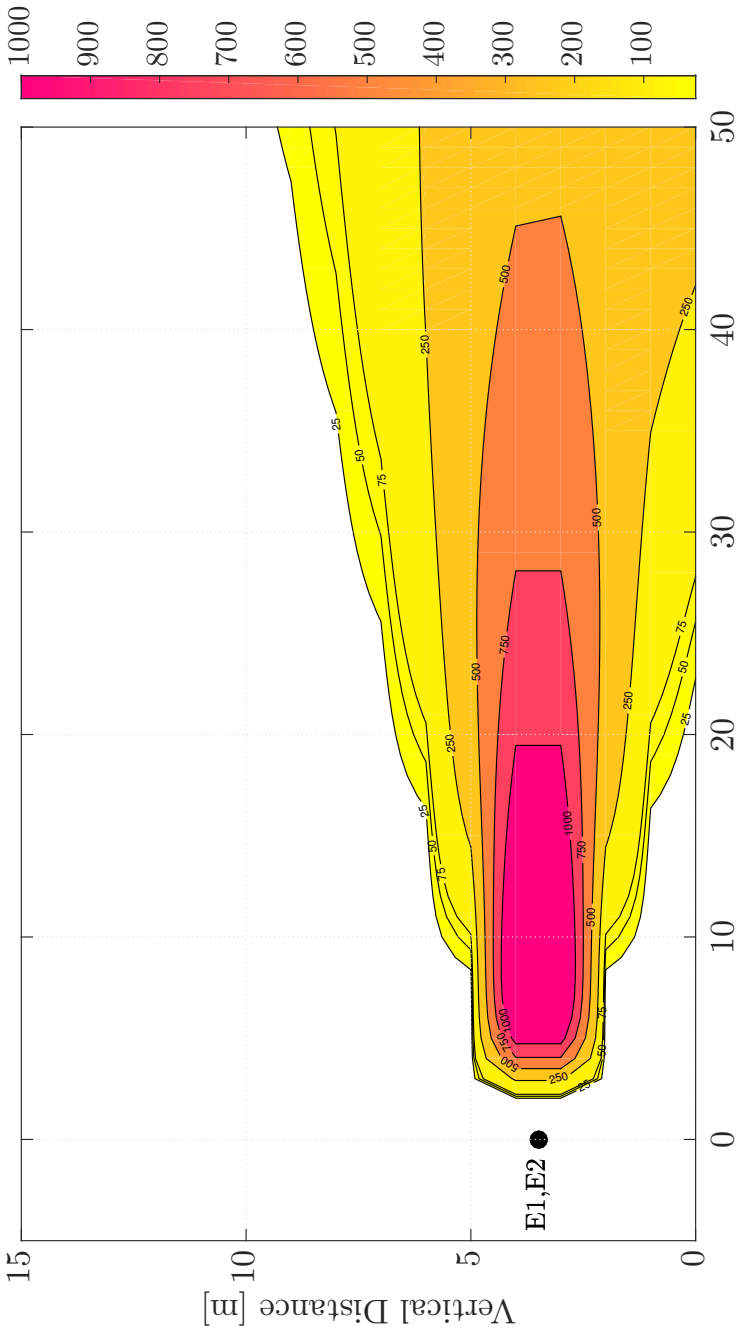

Figure 6.7: Side view of plume concentration-path-length. Hotter colors indicate a higher *CPL*s. Ground reflections cause an asymmetric plume at further downwind distances (beginning at 40 [m]). The imaging system can begin to capture at 15 [m] downwind from the engines, when the plane has moved enough to allow the reflective plate to be visible by the camera.

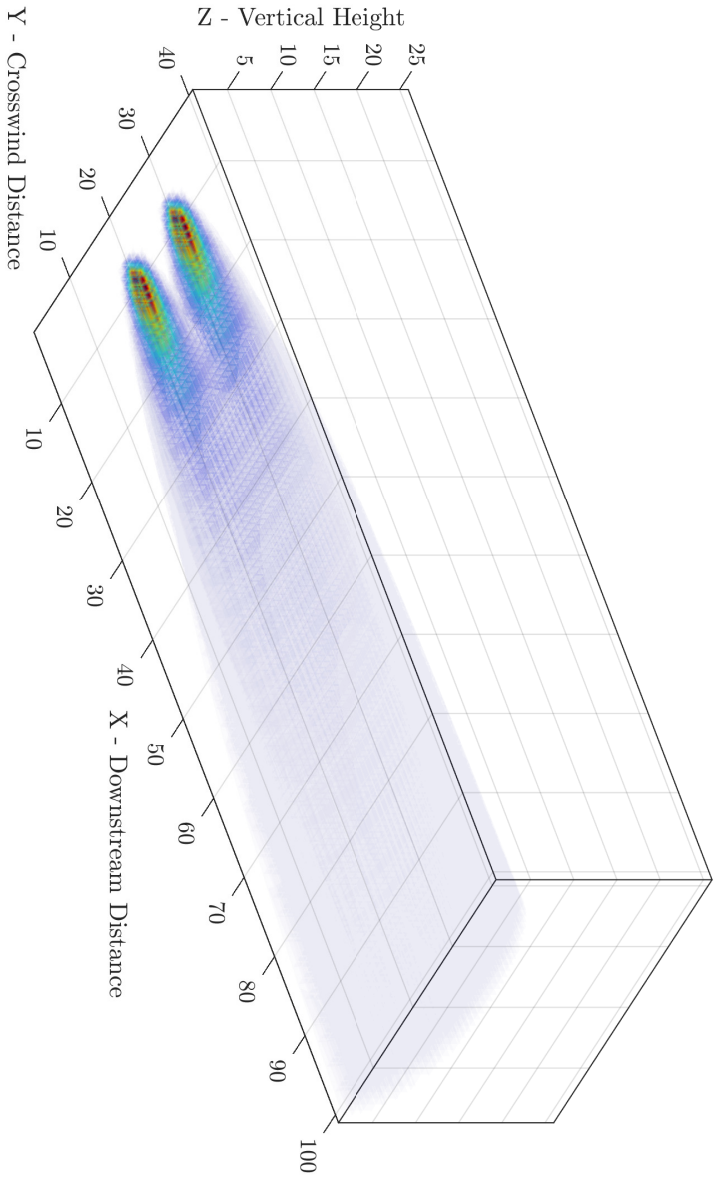

Figure 6.8: 3-D model of idle plume concentration, with hotter colors indicating higher concentrations.

Chapter 7

Results

The Gaussian plume model provides the capability to model the concentration of unburned hydrocarbons (UHCs) in the idle exhaust plume of a typical Boeing 737 (B737) jet engine. This chapter presents the results of the plume concentration and transmission modeling (*Objective 2c*), and the predictions of plume radiance (*Objective 2d*). It concludes with a selection of on-hand and ideal filters used for tracking the plume presence (based on the radiometric models), an assessment of plume detectability at various noise equivalent change (delta) in temperature (NEΔT) values, and with a temporal model of filtered camera observations.

7.1 Concentration Model

A basic method for modeling plume concentration, and graphical results of that method, were presented in §6.2. However, those models used a general UHC pollutant emission index (EI), which assumes that all UHCs are emitted equally. This is not the case, and as concentration levels of each UHC will affect the strength of absorption features in transmission models (see next section), it is necessary to account for the different ratios of UHC EIs.

Multiple studies have been undertaken to estimate UHC speciation in idle plumes[30,35,42,66]. We use a combination of measurements obtained from Spicer et al. (1994) and the National Aeronautics and Space Administration (NASA) Aircraft Particle Emissions eXperiment (APEX) campaign (detailed in Chapter

Table 7.1: List of hydrocarbons included in plume models. *EIs* relative to formaldehyde were measured by multiple sources in facilities or outside. *EIs* were scaled to sum to a typical UHC *EI* of 2.5 [g/kg], and the molar mass *M* was used to convert between $[mg/m^3]$ and [ppm] (see §6.2).

Chemical Constituent	Formula	Test Location	Relative *EI* $[g/kg]$	Scaled *EI* $[g/kg]$	Molar Mass $[g/mol]$
Formaldehyde	HCHO	Outside[35]	1.00	0.518	30.03
Acetaldehyde	C_2H_4O	Outside[35]	0.35	0.181	44.05
Ethylene	C_2H_4	Outside[35]	1.26	0.653	28.05
Propene	C_3H_6	Outside[35]	0.36	0.186	42.08
Butene 1	C_4H_8	Outside[35]	0.36	0.048	56.11
Butene 2	C_4H_8	Outside[35]		0.048	56.11
Acrolein	C_3H_4O	Outside[35]		0.095	56.06
Pentenes	C_5H_{10}	Outside[35]	0.11	0.057	70.13
Benzene	C_6H_6	Outside[35]	0.14	0.073	78.11
Toluene	C_7H_8	Outside[35]	0.05	0.026	92.14
Styrene	C_8H_8	Outside[35]	0.03	0.016	104.15
Naphthalene	$C_{10}H_8$	Outside[35]	0.04	0.021	128.17
Methanol	CH_3OH	Facility[42,66]	0.15	0.078	32.04
Phenol	C_6H_6O	Facility[35]	0.02	0.009	92.11
Acetone	C_3H_6O	Facility[35]	0.24	0.014	58.08
Propanal	C_3H_8O	Facility[35]		0.030	60.10
Glyoxal	$C_2H_2O_2$	Facility[35]		0.076	58.04
Acetic Acid	$C_2H_4O_2$	Facility[42,66]	0.1	0.052	60.05
p-xylene	C_8H_{10}	Facility[35]	0.09	0.046	106.16

3). UHC *EIs* are given in terms of formaldehyde. Given a general UHC *EI* of 2.5 [g/kg], all individual components are scaled to sum to 2.5. *EIs* for the 19 components presented in Chapter 5 are shown in Table 7.1 (*Objective 1b*). The table also lists the chemical symbol of each component, and the testing location that was used to determine the *EI* (outside or indoor facility). Finally, the molar mass *M* [g/mol] is listed as well, used to convert concentration measurements from [mg/m^3] to [parts-per-million (ppm)].

Gaussian plume modeling was done for each component, and a concentration-path-length (*CPL*) was determined along the engine height at z=3.5 [m]. Summing the *CPL* for each component gives a general *CPL* for all UHCs under consideration in an idle plume (Figure 7.1). This represents a plume snapshot, or the plume *CPL* for a stationary aircraft.

However, the temporal nature of a moving aircraft must be accounted for as well, as the aircraft will be taxiing at a rate of 7.7 [m/s]. The plume of a moving aircraft is represented as a series of stacked snapshot

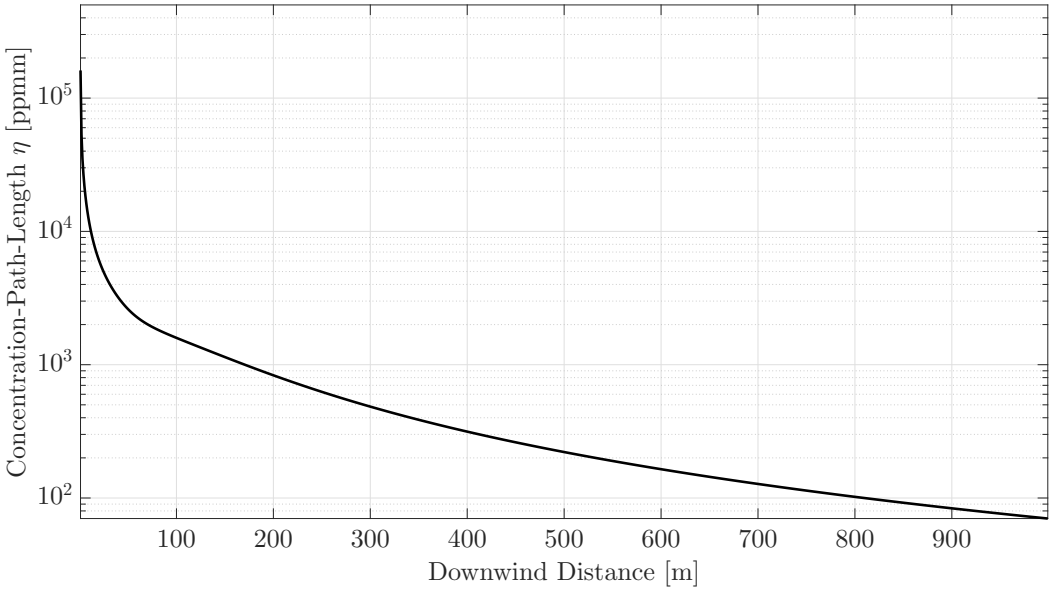

Figure 7.1: Plume *CPL* modeled with the Gaussian Plume Equation, as a function of downwind distance.

plumes. At every instance the aircraft moves forward, a new snapshot plume is generated and added to the previous plume. Mathematically, this is interpreted as the integrated *CPL*.

Figure 7.2 shows the integration of a single aircraft *CPL* as a solid line on the left-hand side and a dashed line on the right-hand side. The UHC concentration now increases without bound, and thus a plume dispersion parameter for the time domain must be included in the model.

Temporal dispersion is modeled to begin at the knee of the integrated plume model, defined as the location where the curve can be best approximated as a pair of straight lines. This occurs at 34.3 [s], or 264 [m], and is represented in Figure 7.2 as a black point. The Gaussian assumption of plume behavior (as presented in §6.2) is employed again, and a decaying Gaussian is modeled to account for temporal plume dispersion. The peak of the decaying Gaussian is set to match the value of the integrated *CPL* model at the knee of the curve, and the center set to 34.3 [s]. The standard deviation was estimated to be $^2/_3$ of the downwind distance at the knee of the curve (89 [m]). Note that this standard deviation was estimated with the goal of producing a smooth decay in *CPL*; no data on temporal dispersion parameters is currently known to be available for this problem.

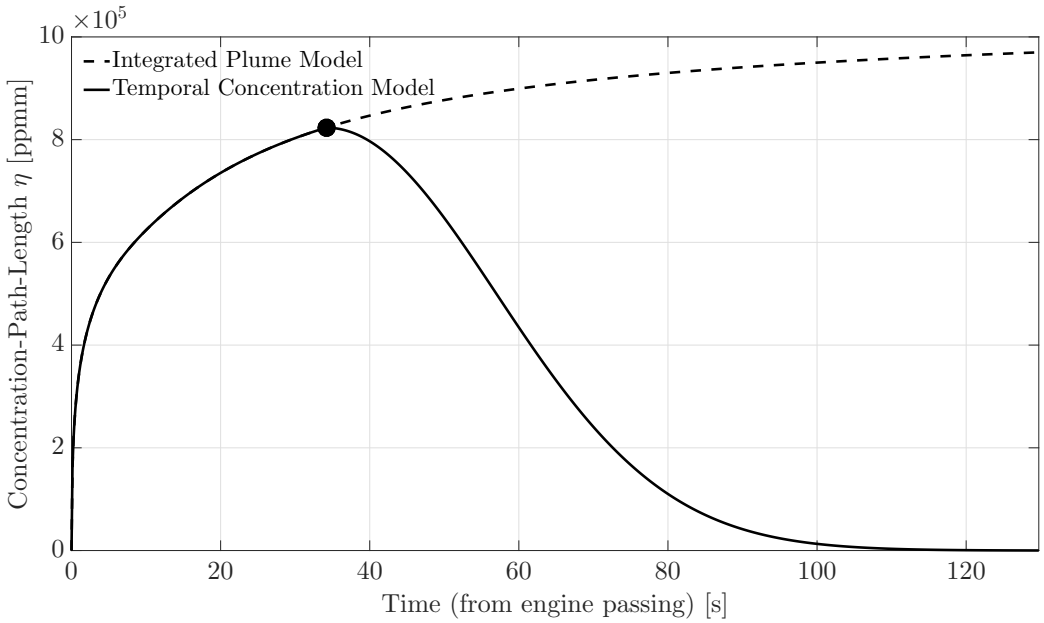

Figure 7.2: Integrated plume *CPL* as a function of downwind distance, to represent a taxiing aircraft (solid black line on left, dashed black line on right). Turning point in integrated curve (point) representing where temporal dispersion effects will begin, and the Gaussian temporal dispersion factor modeled after the turning point (solid black line on right).

The full *CPL* model, including the temporal dispersion effect, is shown as the solid black line in Figure 7.2 (*Objective 2c*). The standard deviation estimation will have a significant effect on how soon the *CPL* returns to background levels, indicating the plume has dissipated. Larger standard deviations will model an extended plume presence, while smaller standard deviations will shorten the estimated time for complete plume dispersion. This value will be better estimated empirically during initial observations, and will be a significant contribution to current knowledge of plume dissipation.

With the speciated *CPL* developed for idle exhaust plumes, the plume transmission was modeled. This was one of the final requirements before the sensor-reaching radiance of the multispectral imaging system could be modeled.

7.2 Plume Transmission

It was previously mentioned that the plume CPL and each UHC absorption spectra will impact the plume transmission. This becomes apparent with Beer's Law, written as

$$\tau(\lambda) = \exp^{[-\Sigma(nz\alpha(\lambda))]}, \tag{7.1}$$

with concentration η [ppm], where z is the path length [m], and $\alpha(\lambda)$ is the absorption profile for each pollutant [parts-per-million-meter $(\text{ppmm})^{-1}$]. Recall that ηz forms the CPL, which was modeled in the previous section. Each UHC is associated with a unique CPL (§7.1) and absorption spectrum (Chapter 5) forming $\eta z \alpha(\lambda)$ for each constituent. Summed together, this becomes the exponent in Equation 7.1. It is apparent that larger values of η, z, and $\alpha(\lambda)$ lead to lower plume transmission values, which is ideal for plume detection.

The 50° [C] absorption spectra will always be used in this model, as temperature impacts on broadening were shown to be limited in Chapter 5. This means that the overall plume transmission will mainly depend on the CPL, and we expect the general trend to inversely coincide with our temporal CPL model from Figure 7.2 (i.e. the plume transmission will be lowest at the knee in the curve, where the CPL is highest, and greatest at large downwind distances, where the CPL is minimized).

The plume transmission (*Objective 2c*) was plotted at downwind distances of 15 [m] (the point at which the aircraft has passed and the reflective plate is again viewable by the camera), 264 [m] (the point at which the plume transmission is lowest and begins to increase again), 600 [m], and 750 [m] (Figures 7.3-7.6).

To study the trends in plume transmission, the peak located at 12.25 [μm] and the valley located at 10.5 [μm] were examined. At 15 [m] downwind (Figure 7.3), the peak is at almost 90% transmission, while the valley transmits essentially zero radiance. At 264 [m] downwind where the CPL is at its maximum (Figure 7.4), the peak is down to almost 80% transmission, and the valley has grown in width from its 0% transmission center. Drastic effects are seen at 600 [m] downwind (Figure 7.5), where the peak has risen to above 90%, and the valley has shrunk in size, just barely dropping to 0% transmission. Finally, at 750 [m] downwind (Figure 7.6), the peak is hardly discernible at nearly 100% transmission and the valley has increased to above 40% transmission.

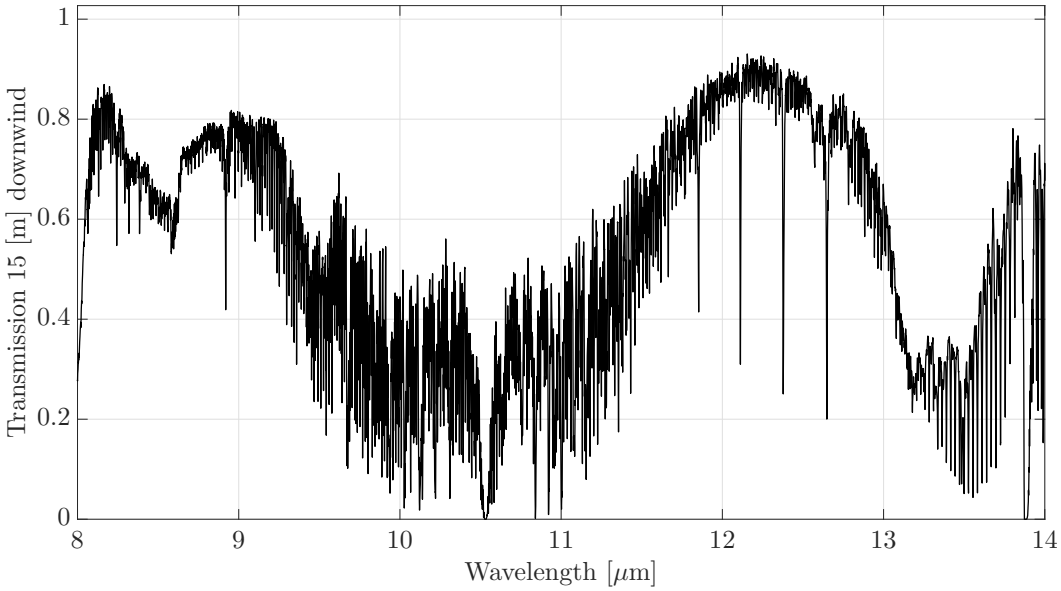

Figure 7.3: Plume transmission modeled at 15 [m] downwind distance. Significant effects are seen in the 10.5 [μm] region.

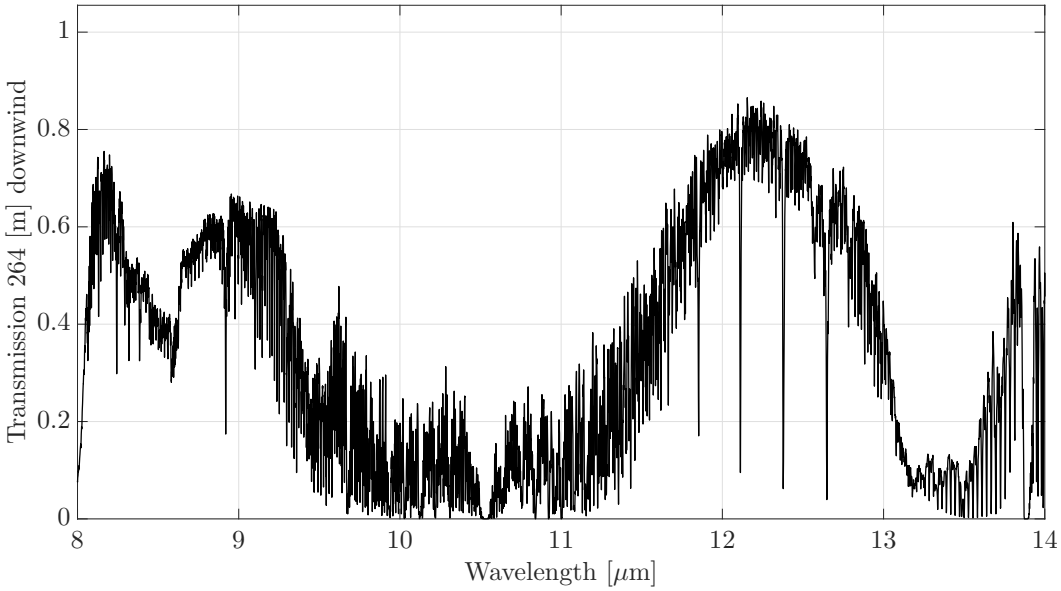

Figure 7.4: Plume transmission modeled at 264 [m] downwind distance. The well around the 10.5 [μm] region has widened compared to Figure 7.3. This represents the turning point in the concentration-path-length model, where temporal dispersion begins; thus the CPL is maximized here and the transmission is the lowest we expect to see.

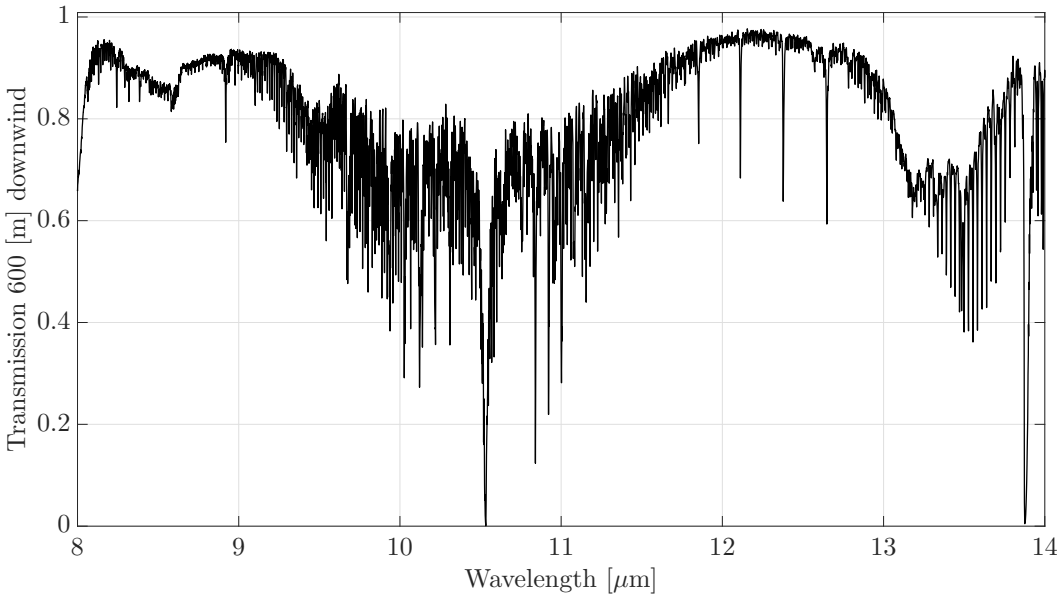

Figure 7.5: Plume transmission at 600 [m] downwind. The transmission values around 10.5 [μm] have significantly increased as a result of the temporal dispersion.

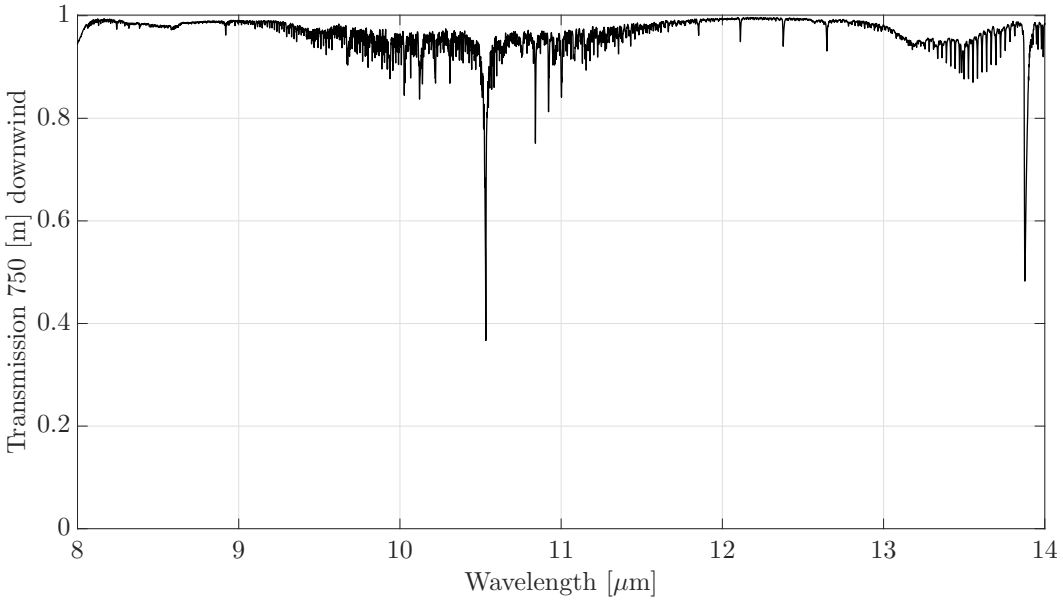

Figure 7.6: Plume transmission at 750 [m] downwind. Due to temporal dispersion, the plume is almost no longer detectable as the transmission values are near 100%.

A physical basis has now been provided to explain how the plume appears, strengthens, and dissipates as a function of downwind distance (analogous to time). The trend will become even more apparent once the plume and background radiance are modeled in §7.4, but first, other parameters in the system governing equation (Equation 4.5) are discussed.

7.3 Non-Plume Parameters

Recall the system governing equation presented in §4.3. The plume transmission was modeled, but the atmospheric and zinc-coated plate radiance, the atmospheric and ground-based transmission, and the reflectivity of the zinc-coated plate remain to be determined.

In §4.3 it was assumed that the sky, zinc-coated plate, and plume could be modeled as blackbody radiators. Planck's Law was used to approximate the blackbody radiance,

$$B_\lambda(\lambda, T) = \frac{2hc^2}{\lambda^5} \frac{1}{\exp^{\frac{hc}{\lambda k_B T}} - 1}, \tag{7.2}$$

where $B_\lambda(T, \lambda)$ is the blackbody radiance at a certain wavelength λ and T is the temperature [K] (assumed to be uniform), h is the Planck constant (6.626×10^{-34} [J·s]), c is the speed of light (2.998×10^{8} [m/s]), and k_B is the Boltzmann constant (1.381×10^{-23} [J/K]). Assuming $T = 260$ [K] for the sky and $T = 295$ [K] for the zinc-coated plate, blackbody radiance models were generated for the atmosphere and plate (Figure 7.7). Note that the warmer temperature plate radiance peaks at a shorter wavelength than the sky radiance, as Planck's Law predicts.

The sky is partially modified by the atmospheric transmission and the plate reflectivity. The plate radiance is partially modified by its emissivity (recall Kirchoff's Law from §4.1). The reflectance of the zinc plate was measured in a laboratory setting with the Surface Optics Corporation 400-T directional reflectometer[67]. Spectral resolution is normally set to 4 [cm^{-1}], but was interpolated to match the spectral resolution of the Pacific Northwest National Laboratory (PNNL) spectra from Chapter 5.

To model the atmospheric transmission, the MODerate resolution atmospheric TRANsmission (MODTRAN) algorithm was used. MODTRAN solves the radiative transport equation by modeling multiple strat-

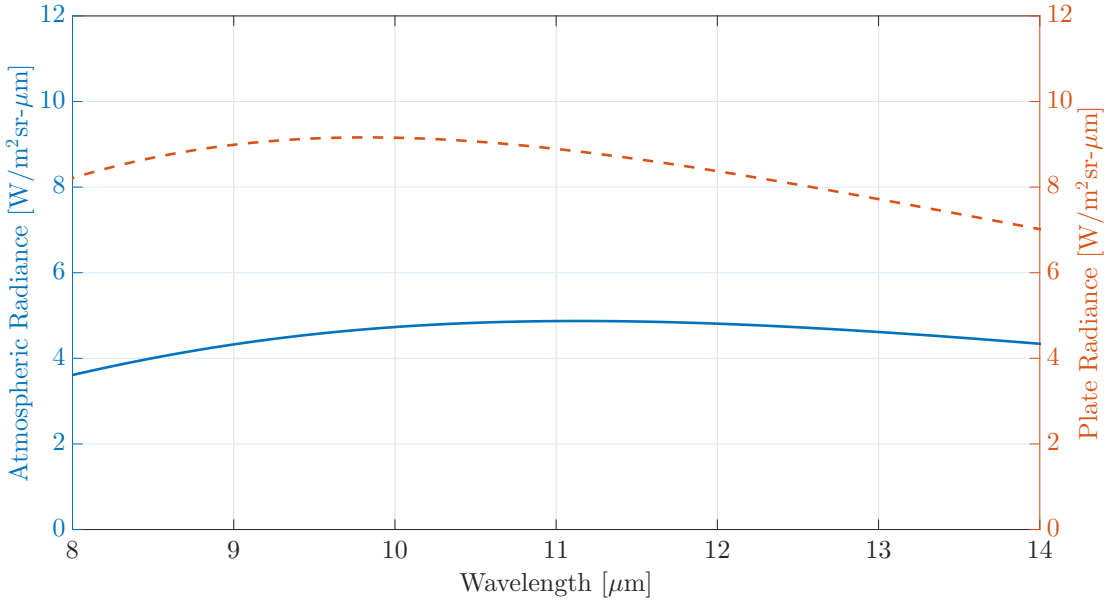

Figure 7.7: Atmospheric radiance (solid blue line, left-axis) modeled as a blackbody with Planck's Law (T = 260 [K]). Zinc-coated plate radiance (dashed red line, right-axis), modeled as a blackbody at T = 295 [K].

ified, horizontally homogeneous layer atmospheres[68]. The model incorporates effects related to molecular and particulate absorption/emission and scattering, surface reflections and emission, and solar illumination[69]. A mid-latitude summer atmosphere was modeled over Rochester, NY (43.26°N, 77.61°W), with default atmospheric constituent profiles, from the elevation of Rochester (0.79 [km]) to a sensor height of 20.53 [km]. The spectral output was given at 0.01 [μm^{-1}] resolution and interpolated to match the resolution of PNNL spectra.

Both the reflectance of the zinc-coated plate and the transmission of the atmosphere are shown in Figure 7.8. The solid blue line shows the atmospheric transmission, while the dashed red line shows the plate reflectivity. Notice that the plate reflectivity is consistently at or above 90%. This is ideal to reflect as much of the sky radiance as possible in order to maximize the temperature contrast between the warm plume and cool background. Kirchoff's Law indicates that the plate emissivity is then very low. It is consistently below 10%, which minimizes the detected radiance from the warm plate blackbody at 295 [K].

Finally, atmospheric transmission effects over short ground distances were considered, specifically over the

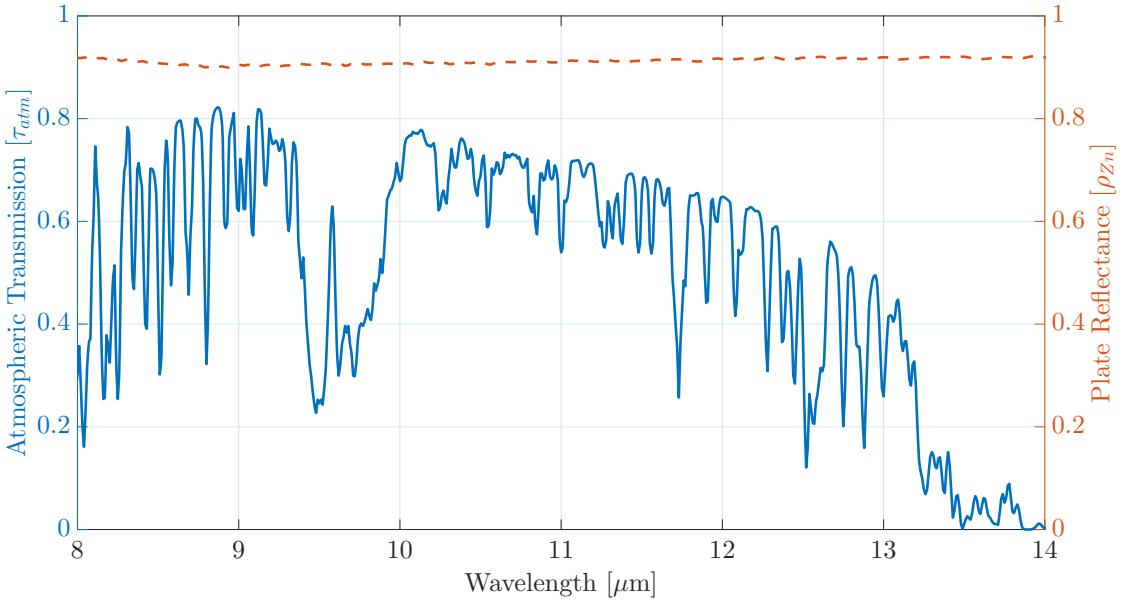

Figure 7.8: Atmospheric transmission modeled over 19.74 [km] for a mid-latitude summer (solid blue line, left axis). Zinc-coated plate emissivity, measured in laboratory (dashed red line, right axis).

50 [m] and 10 [m] paths defined in Equation 4.5. Ground-based transmission effects from object to camera are typically considered negligible over small distances; however this was confirmed using MODTRAN again. The MODTRAN algorithm models the heterogeneous atmosphere by separating it into 32 homogeneous layers based on height. At low altitudes, the homogeneous layers are roughly 1 [km] in height; the layers increase to 5 [km] heights above 25 [km][70]. Since we are only interested in ground-based transmissions at distances shorter than 100 [m], MODTRAN was run using a vertical path from the elevation of Rochester (0.079 [km]) to a height of 0.179 [km]. The transmission was also modeled at 50 [m], 10 [m], and 5 [m] path lengths (Figure 7.9). As expected, the transmission is mostly above 90% and will have little impact on the radiance. In particular, the selected on-hand filter region from 9-10 [μm] is highlighted. The reason for these filters being selected is presented in the next section, which also presents the final models of sensor-reaching radiance for the imaging system.

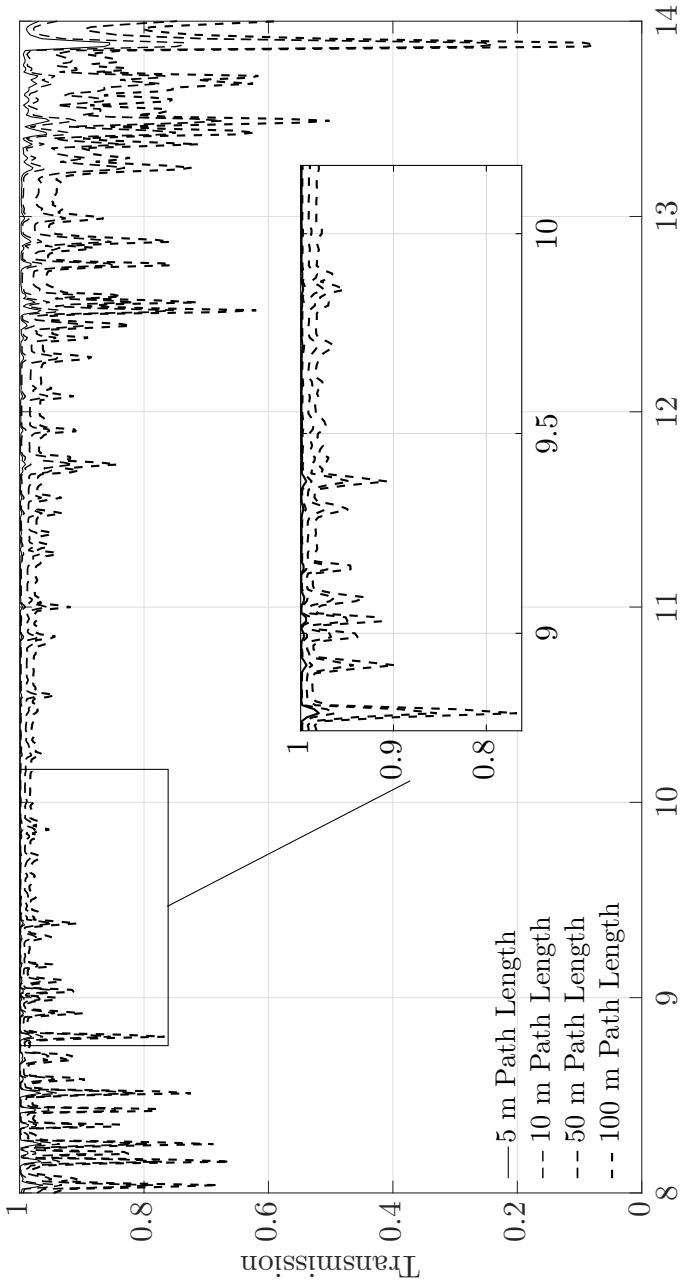

Figure 7.9: Ground-based transmission models for 5, 10, 50, and 100 [m] path lengths. Atmospheric transmission losses over short distances are normally assumed to be negligible, but are included in our model for accuracy. The inset shows the region where two filters were selected to monitor the background radiance and plume radiance (explained further in §7.4).

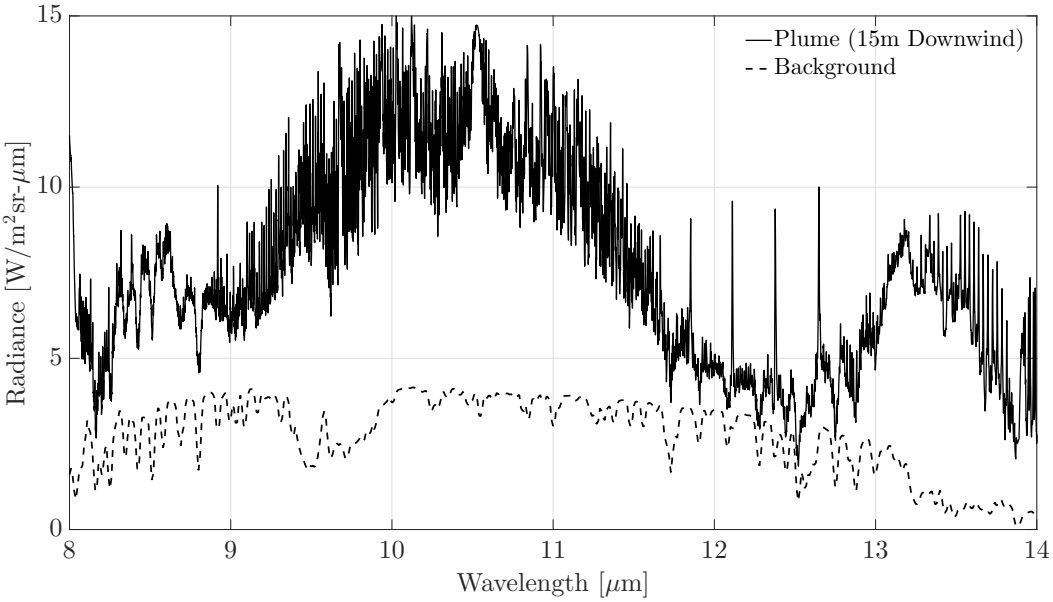

Figure 7.10: Plume radiance (solid black line) and background radiance (dashed black line) at 15 [m] downwind from the aircraft engines.

7.4 Plume Radiance and Filter Selection

At this stage, each parameter of the governing equation has been modeled. The sensor-reaching radiance of the imaging system is modeled in this section and a combination of on-hand filters are selected that will maximize the plume detectability. The radiance models are used to select ideal filters, and the section concludes by examining plume detectability as a function of downwind distance.

In Figures 7.10 - 7.13 we compare the sensor-reaching radiance when there is no plume present to plumes of varying *CPL* strengths (*Objective 2d*). The plume radiance (solid black line) and the expected background radiance (dashed black line) are modeled for downwind distances corresponding to the plume transmission plots in Figures 7.3 - 7.6. For reference, solid blue lines are plotted in Figure 7.11 indicating the center wavelengths (CWLs) of the already purchased filters.

Section 7.2 discussed how the plume transmission was dependent on downwind distance. The same effects can be seen here when comparing the plume and background radiance. At 15 [m] downwind, the difference between plume and background radiance is significant, especially from 9 - 11.5 [μm] and from 13 - 14 [μm].

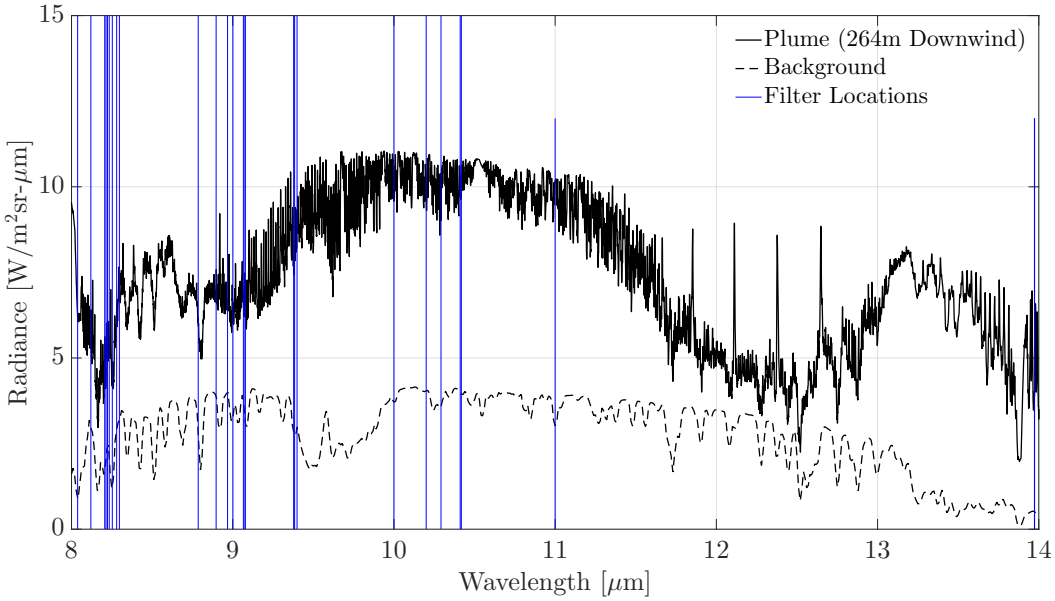

Figure 7.11: Plume radiance (solid black line) and background radiance (dashed black line) at 264 [m] downwind. Solid blue lines indicate the CWL of on-hand filters.

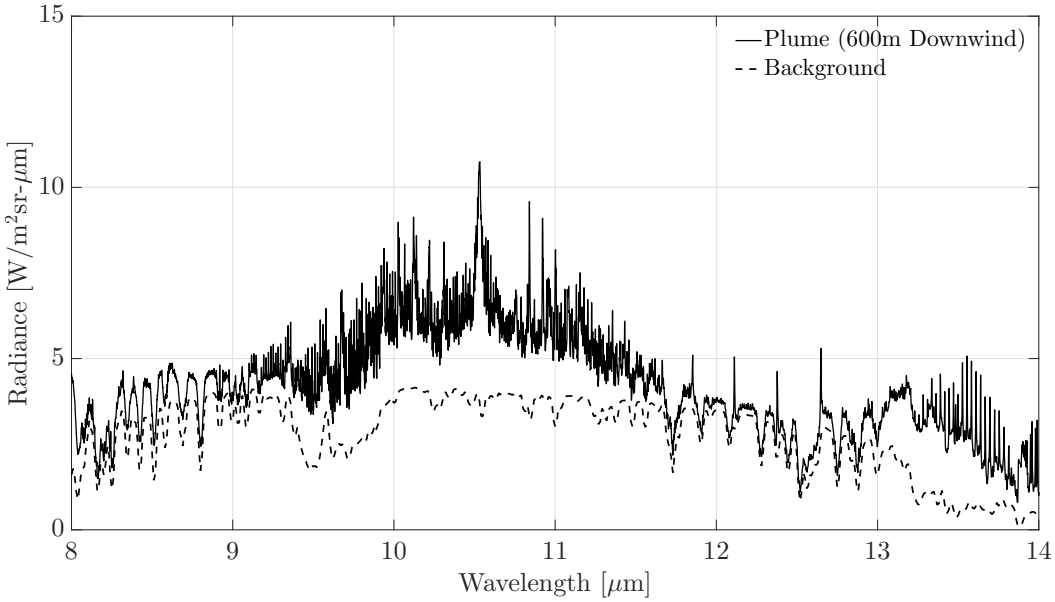

Figure 7.12: Plume radiance (solid black line) and background radiance (dashed black line) at 600 [m] downwind from the aircraft engines. The plume and background radiance are much more similar than Figures 7.10 - 7.11, as a result of temporal dispersion.

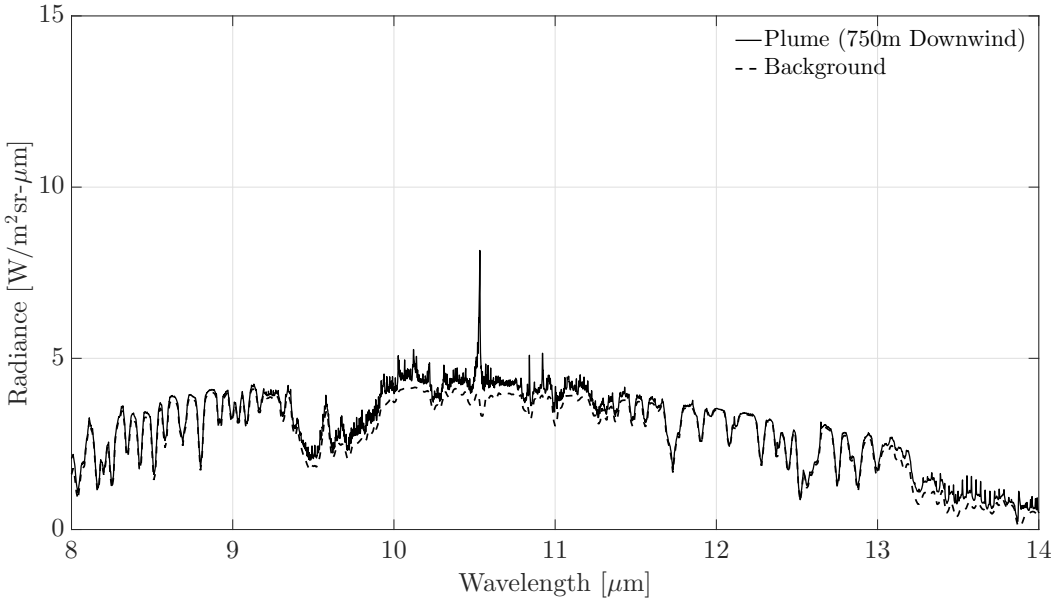

Figure 7.13: Plume radiance (solid black line) and background radiance (dashed black line) at 750 [m] downwind. Differences are virtually indistinguishable as a result of the plume transmission being nearly 100% (Figure 7.6).

The *CPL* is large here, and so is the temperature contrast between plume and sky. The differences are still significant at 264 [m] downwind, as shown in Figure 7.11. This is at the maximum *CPL*, but a smaller temperature contrast between plume and sky results in a slightly smaller radiance difference.

The effects of increased plume transmission are seen in Figures 7.12 - 7.13. As the plume dissipates, the difference between the plume and background radiance decreases until it is almost no longer visible in Figure 7.13. These observations match expectations of a plume becoming more detectable until the *CPL* begins to decrease, at which point the plume becomes increasingly difficult to detect.

Plume tracking will require two-filters: one filter to represent the background (i.e. where the plume transmission is most nearly 100%), and one filter centered on the wavelength with the maximum difference between plume radiance and background radiance (acting as a plume tracer). Thus the difference between the two filter measurements will be minimized to a unique background level when no plume is present.

There were 29 on-hand filters made available for this project; their features are detailed in Table 7.2. CWL values range from 8 - 14 [μm], the available range of an infrared camera. Filters with high transmissions are

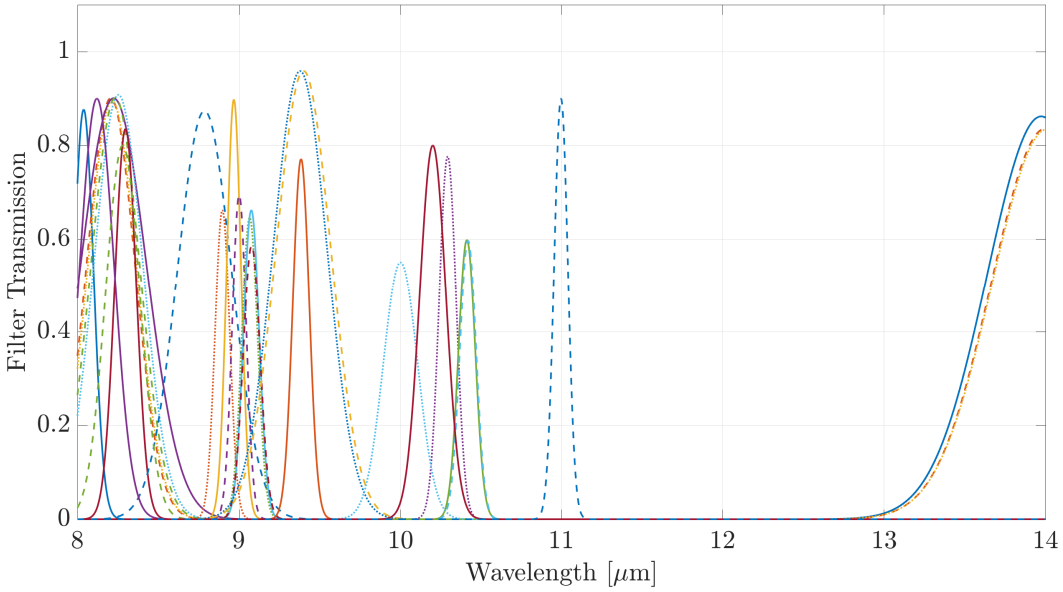

Figure 7.14: Profiles of the 29 on-hand filters available for this study, using the parameters of Table 7.2.

preferable, although some have transmissions below 70%. Finally, the full-width half-max (FWHM) values indicate how wide each filter is. This will determine which wavelengths, or UHC absorption features will be observed.

These filters are visualized as Gausisan distributions in Figures 7.14 and 7.15, using the relationship

$$\sigma = \frac{\text{FWHM}}{2\sqrt{2\ln 2}}, \tag{7.3}$$

which relates the FWHM and the filter standard deviation (σ).

To select the best combination of on-hand filters, the difference between plume and background radiance was modeled at 264 [m] downwind (Figure 7.16). Again, filter centers are indicated with solid blue lines. The difference spectrum was multiplied by each filter profile individually; the results were summed and multiplied by the wavelength sampling interval. This gave an indication of the sensor-reaching radiance associated with each filter. The minimum radiance was selected as the background filter, and the maximum radiance was selected to track the plume formation and dissipation.

Table 7.2: CWL, peak transmission, and FWHM of the on-hand filters available for this study. The two filters highlighted in bold are the two selected for tracking the background and plume radiance (elaborated on later in this section).

CWL [μm]	Peak Transmission [%]	FWHM [μm]
8.038	87.66	0.144
8.120	90.00	0.250
8.206	90.10	0.353
8.214	89.53	0.353
8.223	90.08	0.479
8.234	90.16	0.353
8.253	90.80	0.355
8.280	80.00	0.250
8.297	83.50	0.156
8.786	87.35	0.397
8.897	66.17	0.107
8.968	89.79	0.104
9.001	**69.40**	**0.101**
9.066	64.61	0.115
9.076	66.20	0.115
9.078	58.57	0.123
9.378	95.87	0.393
9.384	77.09	0.119
9.399	**95.90**	**0.398**
10.000	55.00	0.250
10.200	80.00	0.190
10.292	77.64	0.124
10.411	59.84	0.122
10.418	55.69	0.119
11.000	90.00	0.100
13.973	86.17	0.788
13.974	86.19	0.790
14.001	83.60	0.791
14.010	83.42	0.799

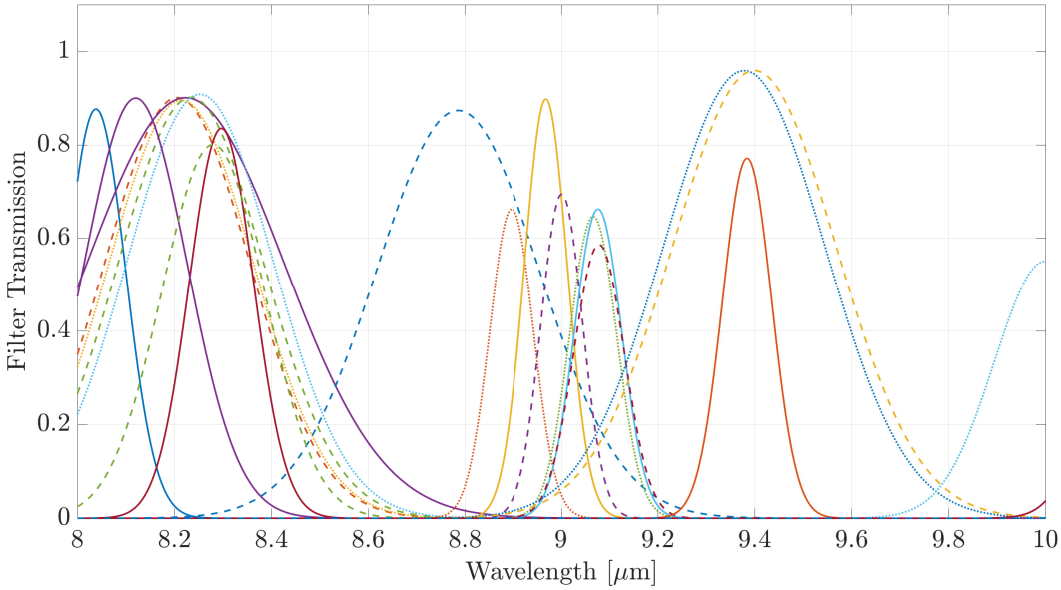

Figure 7.15: Profiles of the 19 filters available for this study centered in the 8 – 10 [μm]region, using the parameters given in Table 7.2.

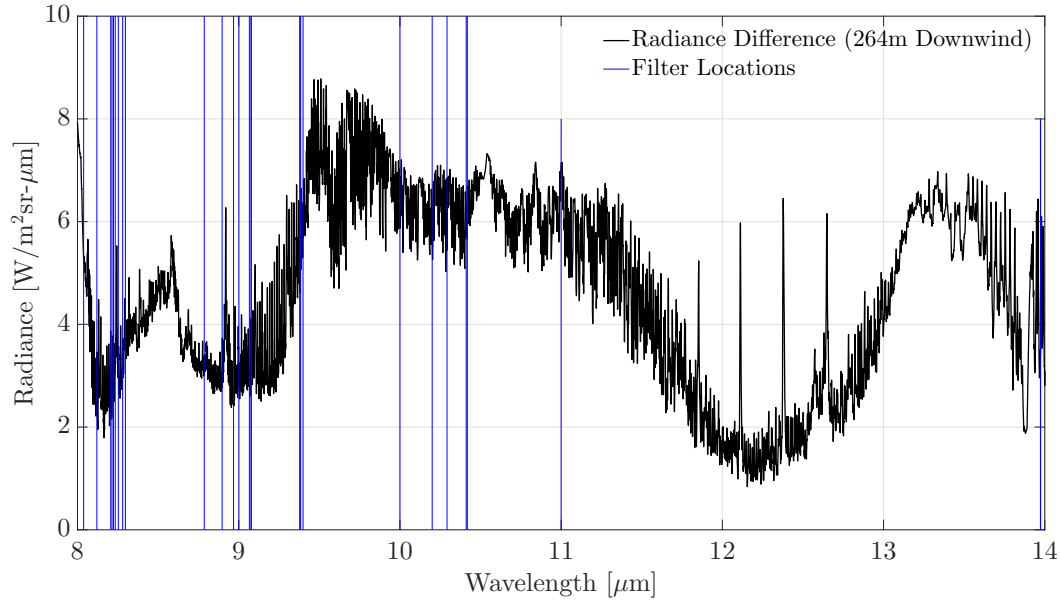

Figure 7.16: Radiance difference between plume and background from Figure 7.11. Larger differences indicate ideal locations for plume tracking filters, while smaller differences indicate ideal locations for background filters. Solid blue lines show CWLs of on-hand filters.

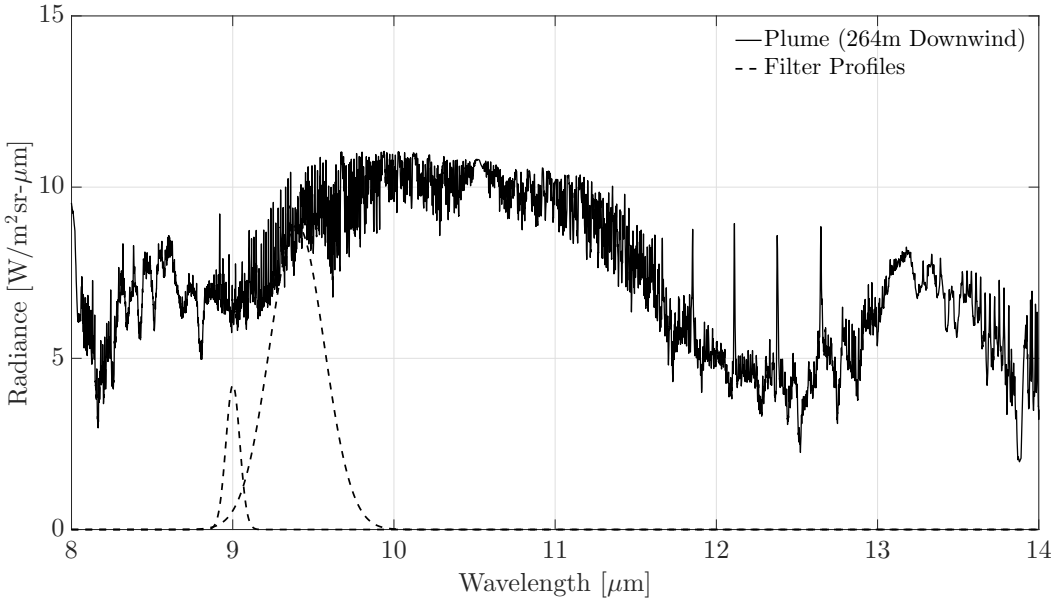

Figure 7.17: Plume radiance at 264[m] downwind with overlaid filters, scaled for the CWL radiance value, selected for background monitoring and plume measurements.

The maximum radiance values were located at the filters centered around 14 [μm], but these were rejected due to the camera sensitivity falloff in that region. With this exclusion, the ideal filter combination used the filters centered at 9.001 [μm] (background) and 9.399 [μm] (plume tracer). Filter standard deviations, obtained with Equation 7.3, were 0.0429 [μm] and 0.169 [μm], respectively. These two filters appear as bold in Table 7.2, and their profiles in combination with the radiance difference can be seen in Figure 7.17. Although the filters slightly overlap at the edges, the difference is still maximized with this combination.

A similar analysis was performed to select ideal filter locations. If any CWL could be chosen, the plume detectability may increase. To ensure a fair comparison between on-hand and ideal filters, the ideal filters used the same FWHM and peak transmission values from the two previously selected filters. The CWL was varied from 8 - 14 [μm] in 0.001 [μm] steps, and the incoming radiance at each location was measured for both filters. The background filter radiance was minimized at 12.212 [μm], while the plume tracing filter was maximized at 9.776 [μm] (Figure 7.18).

The background, or the sensor-reaching radiance baseline, will be the difference in filter readings when

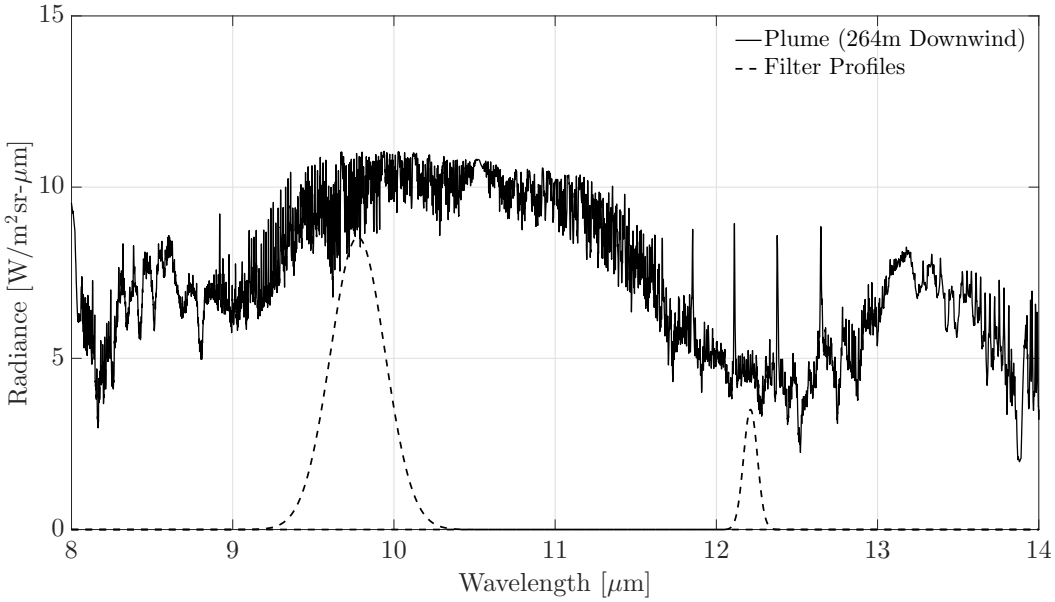

Figure 7.18: Plume radiance at 264 [m] downwind with overlaid filters, scaled for the ideal filters CWL radiance values. Peak transmission and FWHM match those from Figure 7.17 to allow comparisons.

no plume is present. For the on-hand filters, this value is expected to be 0.932 [W/m^{2}sr]. For the ideal filters, the baseline measurement is expected to be 0.907 [W/m^{2}sr].

The difference between the plume and background radiance within the plume tracing filters is indicative of the plume detectability. As the difference approaches zero, the plume is no longer distinguishable from the background levels. A temporal analysis was performed for the plume and background radiance that would be observed in the 9.339 [μm] and 9.776 [μm] filters. Radiance predictions were made for every second after a plane had passed the imaging system, at a velocity of 7.7 [m/s] (Figures 7.19 - 7.20).

The difference can also be compared to various system NEΔTs. NEΔT relates to the system noise equivalent radiance (NER) as

$$\text{NE}\Delta\text{T} = \text{NER}\frac{\Delta T}{\Delta L}. \tag{7.4}$$

Figures 7.19 - 7.20 show NER levels corresponding to NEΔTs of 0.5 [K], 0.25 [K], and 0.05 [K]. (For reference, the FLIR Systems, Inc. (FLIR) Tau® 2 Uncooled Core has a performance NEΔT of 0.05 [K] at

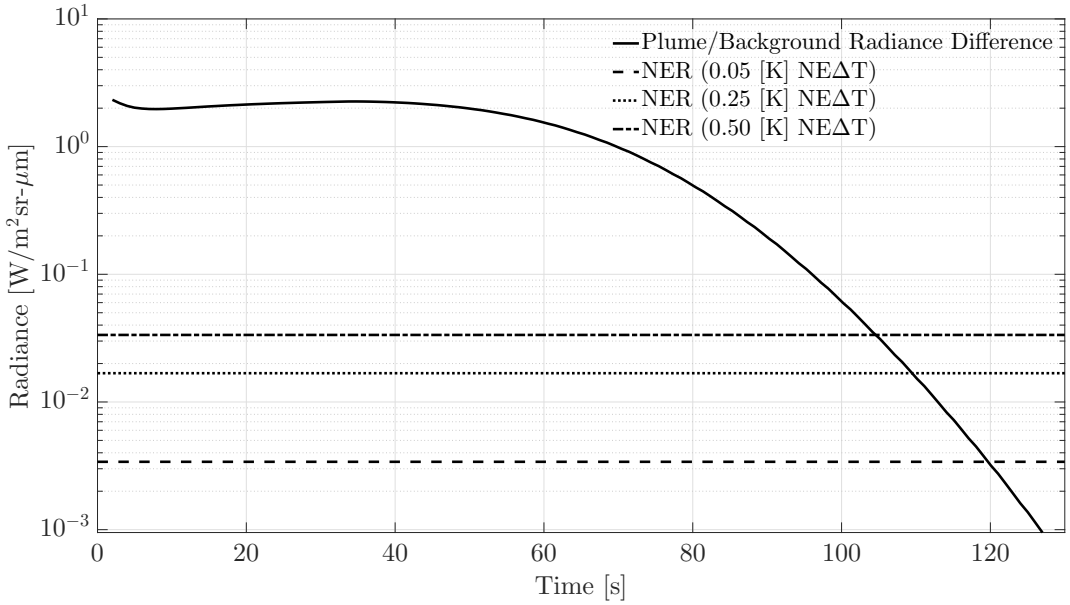

Figure 7.19: Difference in plume and background radiance in the on-hand plume tracing filter located at 9.399 [μm]. As the difference approaches zero, the plume is increasingly difficult to detect. Sample system NEΔTs are converted to NERs; the crossover point indicates where the plume will become undetectable.

$f/1$[71].) Both the on-hand and ideal filter combination indicate that a plume will be detectable out to 100+ [s], or 770 [m] downwind of the engine. It also becomes apparent that the ideally located filters will allow for increased detectability past 120 [s].

With on-hand and ideal filters selected for the proposed system (*Objective 2d*), temporal predictions can be made for the sensor-reaching radiance and filter differences. The next section concludes this chapter with temporal models for multiple taxiing aircraft.

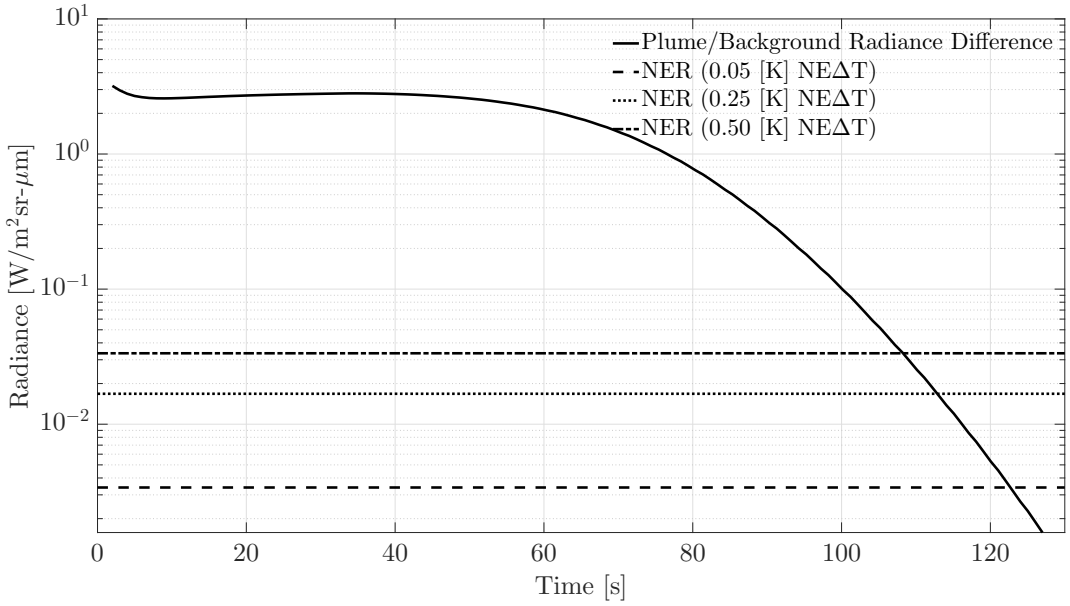

Figure 7.20: Difference in plume and background radiance in the ideal plume tracing filter located at 9.776 [μm]. As the difference approaches zero, the plume is increasingly difficult to detect. Sample system NEΔTs are converted to NERs; the crossover points indicate where the plume will become undetectable. The plume is detectable for a longer than with the on-hand filter.

7.5 Temporal Modeling

An important, and up until this point overlooked, impactor of airport air quality is the time it takes for a plume to disperse. Baggage handlers, aircraft fuelers, and mechanics all work in close vicinity of engine idle plumes. The frequency with which plumes are generated and the rate at which they dissipate will have a significant effect on these workers' exposure to volatile organic compounds (VOCs). Many of the studies presented in Chapter 1 were done at the airport fence line or further away from the runways, where plumes had the space and time to disperse. Worker exposure to VOCs where plumes are being generated, before they have had time to dissipate, will be significantly higher.

We therefore examine the filter difference readings of two stationary cameras fitted with a background and plume tracing filter, set to observe the plumes of taxiing aircraft. In §7.4, the baseline radiance level for a two-filter system was predicted, using on-hand filters and ideally located filters. We simulate readings being taken every second, or every 7.7 [m] of aircraft travel. Note that readings will not be obtainable until two

seconds have passed and the aircraft no longer blocks the reflective plate-camera line-of-sight. The temporal models begin with six seconds of background readings (for each filter combination) before an initial plume is generated (Figure 7.21 - 7.22). As the plume is generated, the difference in filter readings increases by a factor of 3 and 4, for the on-hand and ideal filters respectively. Following this, the filter difference decreases due to the temperature contrast between plume and background decreasing. As the plume temperature approaches ambient, the CPL is still increasing, and thus the filter difference increases again. Roughly 34 seconds after the plume is generated, the temporal dispersion comes into play and the filter difference begins its final descent back to baseline levels. Additional plumes are modeled after 120 [s], 90 [s], 60 [s], and 30 [s]; dashed lines indicate how the plume would dissipate if no subsequent plume were to be generated. Observations of filter differences will serve as indicators of relative plume strength (i.e. accurate background readings of absolute radiance, and thus extremely well-calibrated cameras are not necessary in this set-up).

Notice how the ideal filter differences are greater than the on-hand filter differences. Simulations indicate that when plumes are generated less than one minute apart, there is no time for the preceding plume to completely disperse. With less than one minute separation, the filter readings begin to increase as the plumes stack. Note however that this effect is due in large part due to the standard deviation set for temporal dispersion back in §7.1. The standard deviation will be better set with empirical observations, and the minimum time required for plumes to begin stacking will be adjusted based on this. These models are presented solely as predictions of the trends that our imaging system is expected to find during prototype testing. Initial results will provide valuable information regarding the exposure of airport employees to UHCs/VOCs.

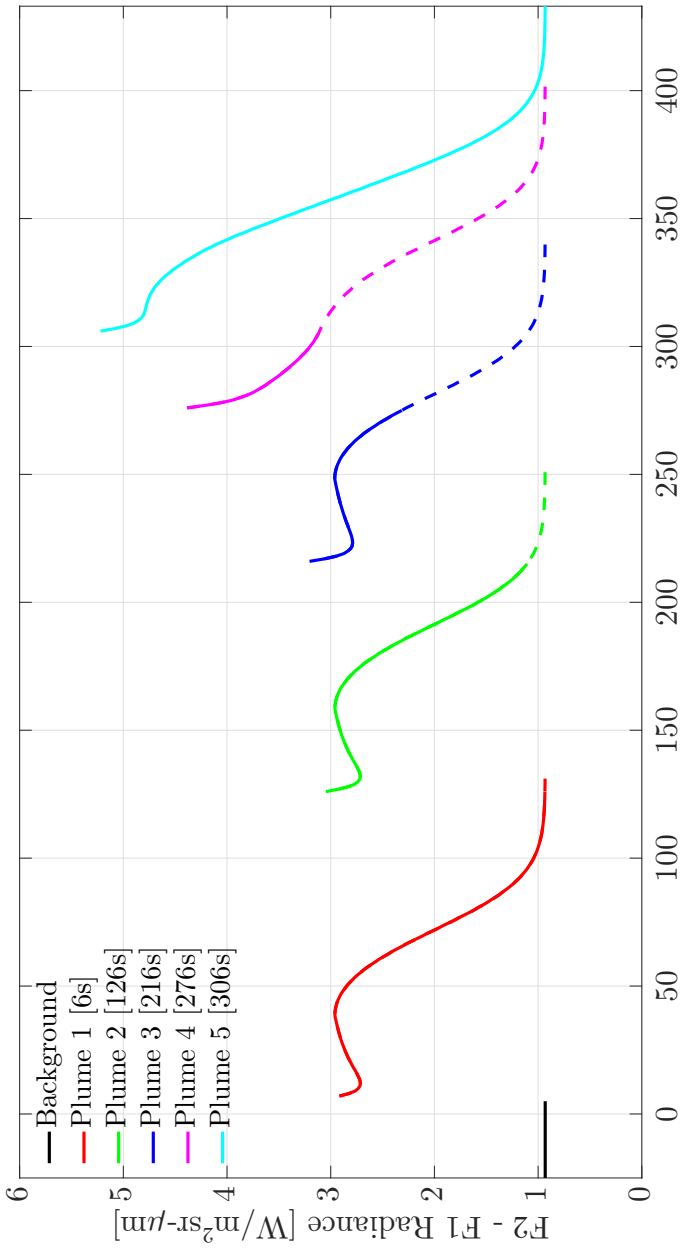

Figure 7.21: Difference between plume tracing and background on-hand filters as a function of time. New plumes are generated at six seconds, 126 [s], 216 [s], 276 [s], and 306 [s], shown as the solid red, green, blue, magenta, and cyan lines. When plumes are generated less than two minutes apart (green to blue), the filter differences begin to increase. Dashed lines show how the filter difference would return to baseline levels (black line), if no new plumes were generated.

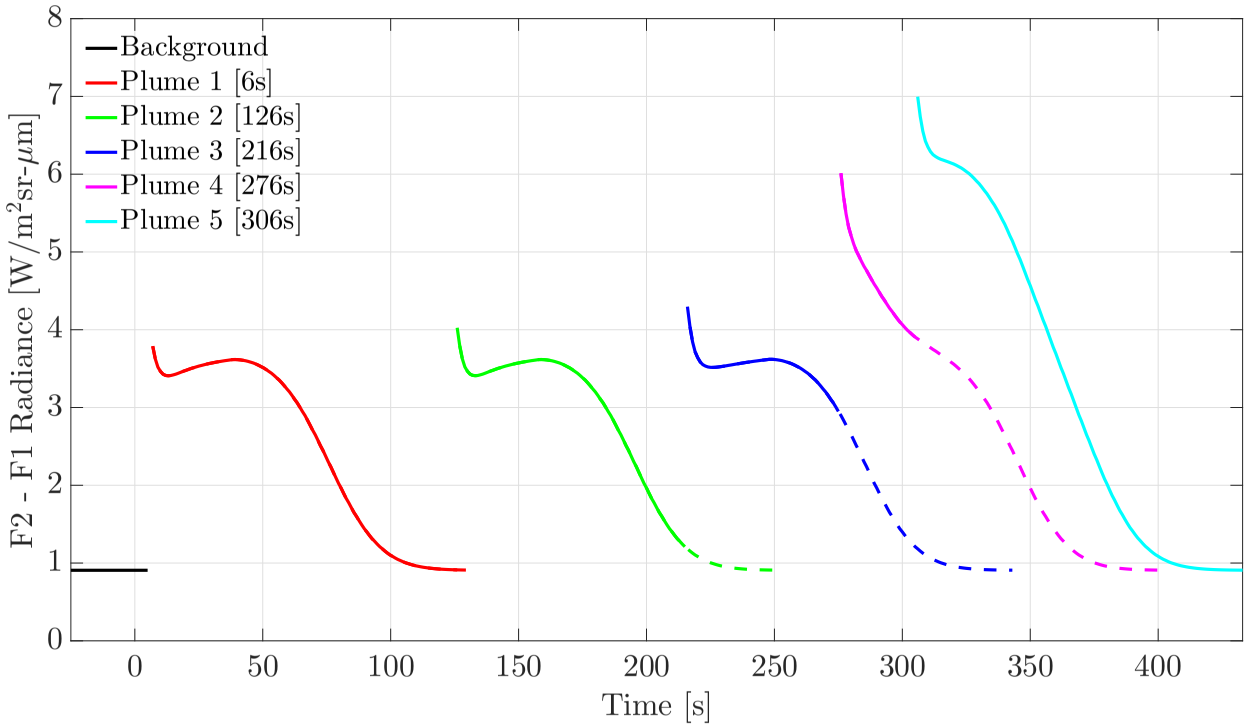

Figure 7.22: Difference between plume tracing and background ideal filters as a function of time. New plumes are generated at six seconds, 126 [s], 216 [s], 276 [s], and 306 [s], shown as the solid red, green, blue, magenta, and cyan lines. When plumes are generated less than two minutes apart (green to blue), the filter differences begin to increase. Dashed lines show how the filter difference would return to baseline levels (black line), if no new plumes were generated.

Chapter 8

Future Work Outlook

It is necessary to understand not just what the camera will observe during operations, but what can be learned from observations. In the following Chapter, a brief overview is given of the information to be gathered in an operational scenario. An extended selection of filters for tracking individual unburned hydrocarbons (UHCs) is also presented, and future work that would benefit this project is described.

Future work on this project will require deploying the prototype imaging system and gathering initial observations. The proposed testing site is Rochester International Airport (ROC), a small airport scheduling mostly regional flights, where Boeing 737s (B737s) are common (Figure 8.1). There are multiple possible points of observation for idling or taxiing; one near to the airport is suggested as it has the highest potential for aircraft traffic. In this chapter we discuss what information we can gather from our imaging system, and propose capabilities for acquiring additional information.

8.1 Observations to Information

The proposed multispectral imaging system will consist of two cameras with two filters, described in the previous chapter. The difference in measurements between the two filters will enable tracking of the relative plume strength and generate temporal observations similar to the predictions presented in §7.5.

In this section we discuss what else we can learn from our system; specifically, can we predict actual

Figure 8.1: Google screenshot of Rochester International Airport, showing two major runways, and multiple taxiways available for observations.

concentration levels for individual UHCs, and is it possible to measure pollutant emission indices (EIs) for each aircraft engine? Recall the governing equation presented in §4.3. When there is no plume present, this equation simplifies to

$$\begin{aligned} L_{np}(\lambda) =& \tau_{atm}\tau_{10}\tau_{50}B(T_b,\lambda)\rho_{Zn} \\ &+ \tau_{10}\tau_{50}B(T_{Zn},\lambda)(1-\rho_{Zn}), \end{aligned} \tag{8.1}$$

with the same definitions given previously. We can simplify the governing equation to

$$L_{sky}(\lambda) = \tau_p\left[L_{np} - \tau_{50}B(T_p,\lambda)\right] + \tau_{50}B(T_p,\lambda). \tag{8.2}$$

The one parameter of interest is the plume transmission τ_p. Assuming the 50 [m] atmospheric transmission can be accurately modeled with the MODerate resolution atmospheric TRANsmission (MODTRAN) algorithm, and the plume can be modeled as a blackbody, τ_p should be easily determined. From τ_p our goal is to determine the concentration-path-length (CPL). This requires the assumption that the Pacific Northwest National Laboratory (PNNL) absorption spectra are accurately measured (a fair assumption discussed in Chapter 5). Beer's Law can also be written as

$$\ln\tau_p = -\sum \eta z \alpha. \tag{8.3}$$

Representing ηz as the single variable CPL gives an equation with 23 unknowns (the CPLs for each constituent) and 24 knowns (plume transmission and constituent absorption spectra). With the measured ratio of UHC emissions, discussed in §7.4, the CPL can be determined for each UHC. Since the path-length z will be the same for all CPLs, we can also obtain an accurate measurement of each UHC concentration (*Objective 3*). This relies on the speciation of hydrocarbons being accurate.

This assessment can be taken one step further: if we know the downwind distance where the measurement was obtained, the Gaussian plume equation can be used to determine the emission rate, q, of each pollutant. Finally, if accurate information is available regarding the engine fuel flow during idling, the initial parameter,

the emission index (EI), can be determined.

The bare minimum capability of this system is to track relative plume strengths as they are generated and dispersed, using a baseline level measured with two filters. However, there is a high potential to extend the capabilities of this system to extract information such as concentration levels and engine EIs. In the next section, further system improvements are discussed that would allow for the tracking of individual UHCs.

8.2 Tracking Individual Hydrocarbons

A total of eight infrared cameras were purchased for this project, and two filters selected to track relative plume presence. Six cameras remain with which to gather information. In this section we assess the potential of using additional filters to track individual pollutant species within exhaust plumes.

The total plume transmission (including all UHCs) was modeled at 15 [m] downwind (Figure 7.3). The plume transmission is remodeled at 15 [m] downwind, this time removing each UHC contributor one-by-one. The total plume transmission is then subtracted from the newly modeled transmission, where one constituent is missing. This gives an idea of how much each pollutant lowers the plume transmission (Figures 8.2 - 8.8). The effect each pollutant will have is dependent on its concentration (i.e. emission index) and the strength of its absorption features. Of the 19 UHCs under study, formaldehyde, acetaldehyde, ethylene, propene, naphthalene, methanol, and acetic acid had the most significant impact on the plume transmission. Most differences were found to be above 20%. Using the same background filter selected in Chapter 7, the change in individual pollutant levels could be targeted with narrowband filters. This requires ensuring that the targeted wavelengths have no overlap with other UHC absorption features. In particular, many significant features of the above-listed UHCs are covered by the ethylene absorption from 9 - 12 [μm]. Some potential filter locations, and the UHCs they would monitor, are listed in Table 8.1.

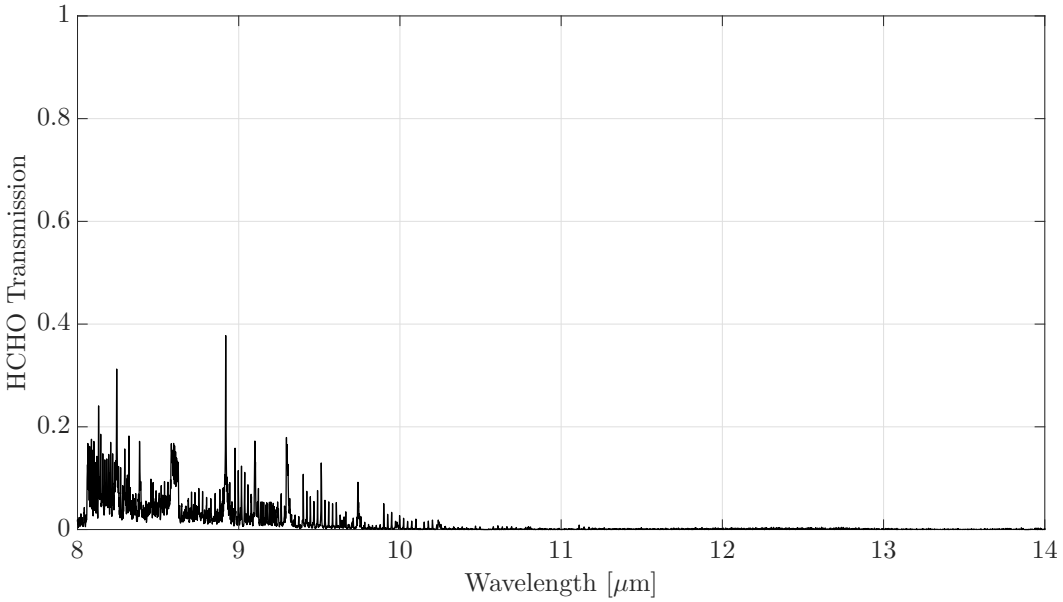

Figure 8.2: The effect of formaldehyde emissions on plume transmission, shown as the difference between total plume transmission (with all UHCs included) and transmission without formaldehyde included.

Table 8.1: Suggested center wavelengths (CWLs) for filters to track individual or groupings of hydrocarbon emissions.

Wavelength [μm]	Targeted UHCs
8.446	Acetic Acid ($C_2H_4O_2$)
8.992	Formaldehyde (HCHO)
	Acetaldehyde (C_2H_4O)
9.679	Methanol (CH_3OH)
10.53	Ethylene (C_2H_4)
10.96	Propene (C_3H_6)
12.79	Naphthalene ($C_{10}H_8$)

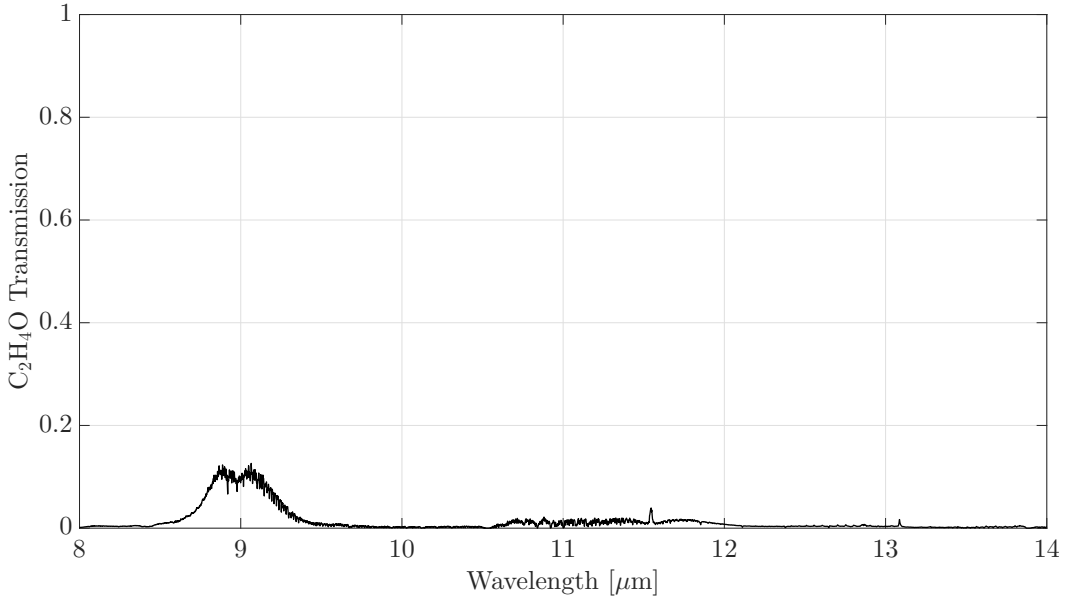

Figure 8.3: The effect of acetaldehyde emissions on plume transmission, shown as the difference between total plume transmission (with all UHCs included) and transmission without acetaldehyde included.

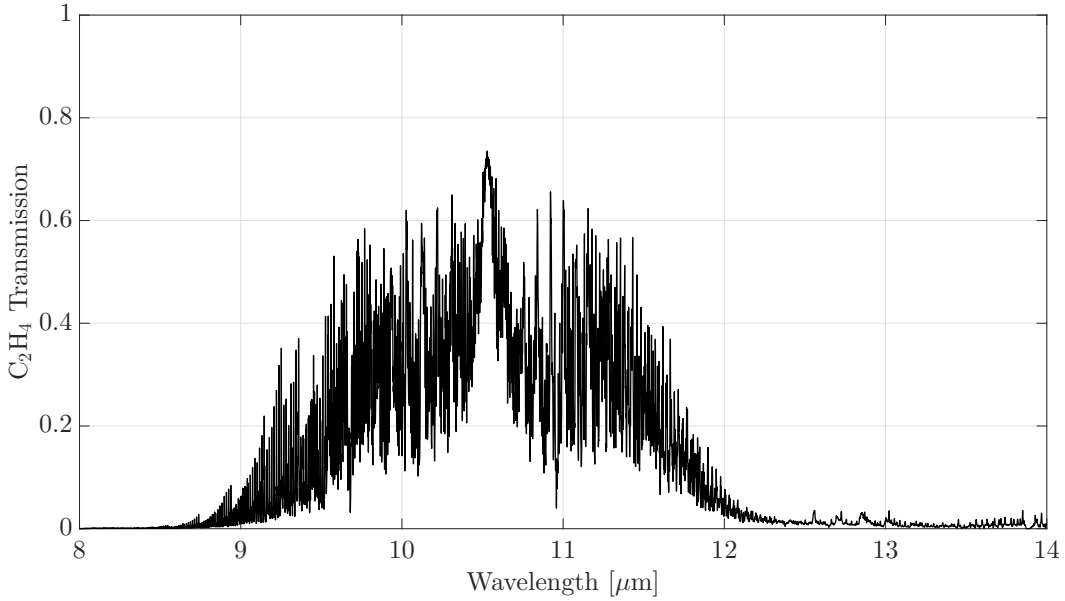

Figure 8.4: The effect of ethylene emissions on plume transmission, shown as the difference between total plume transmission (with all UHCs included) and transmission without ethylene included.

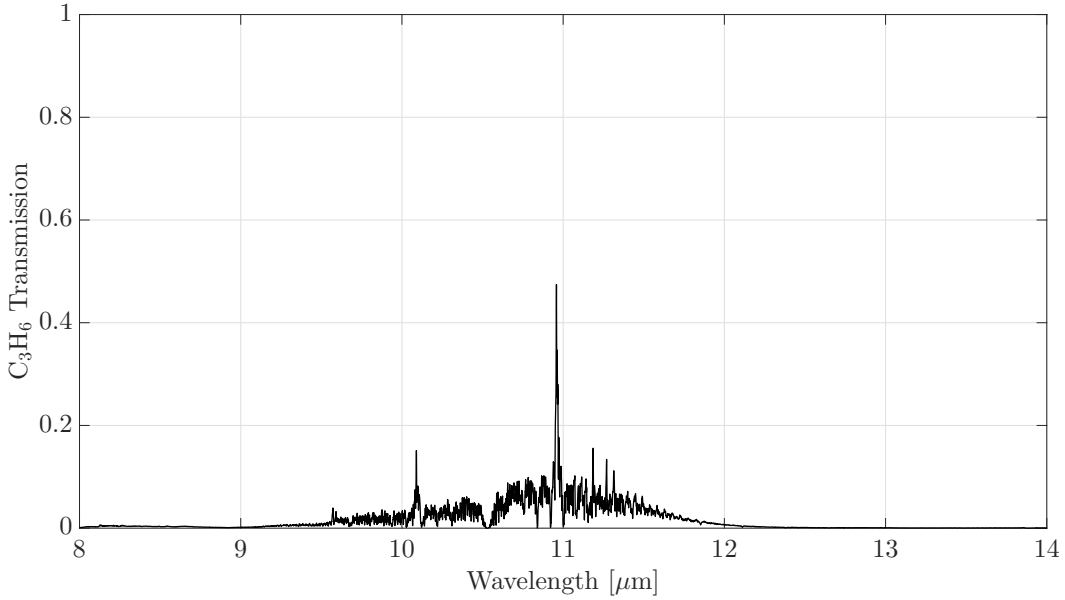

Figure 8.5: The effect of propene emissions on plume transmission, shown as the difference between total plume transmission (with all UHCs included) and transmission without propene included.

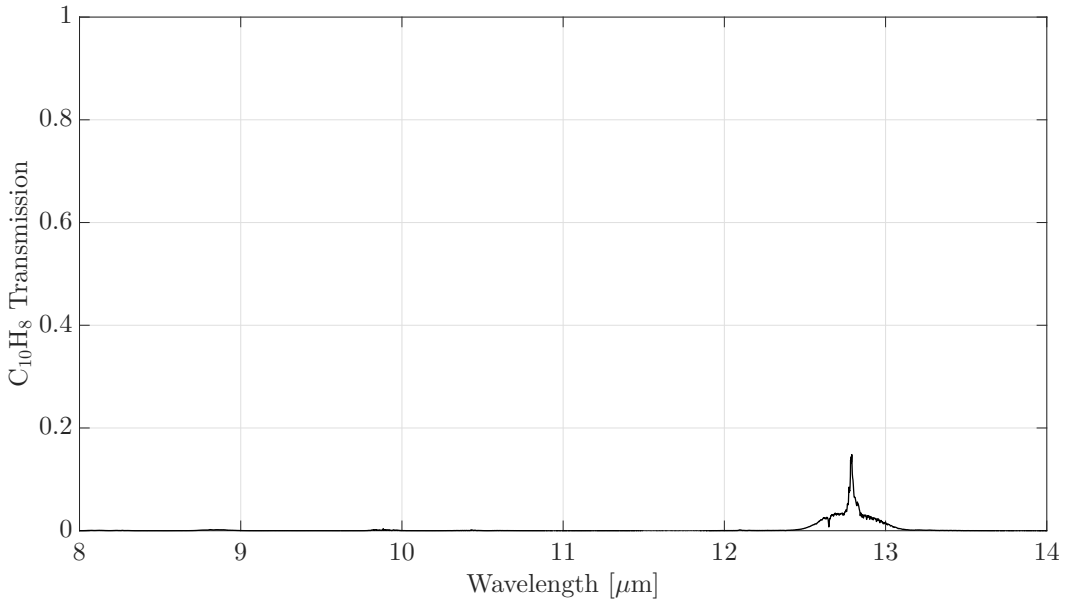

Figure 8.6: The effect of naphthalene emissions on plume transmission, shown as the difference between total plume transmission (with all UHCs included) and transmission without naphthalene included.

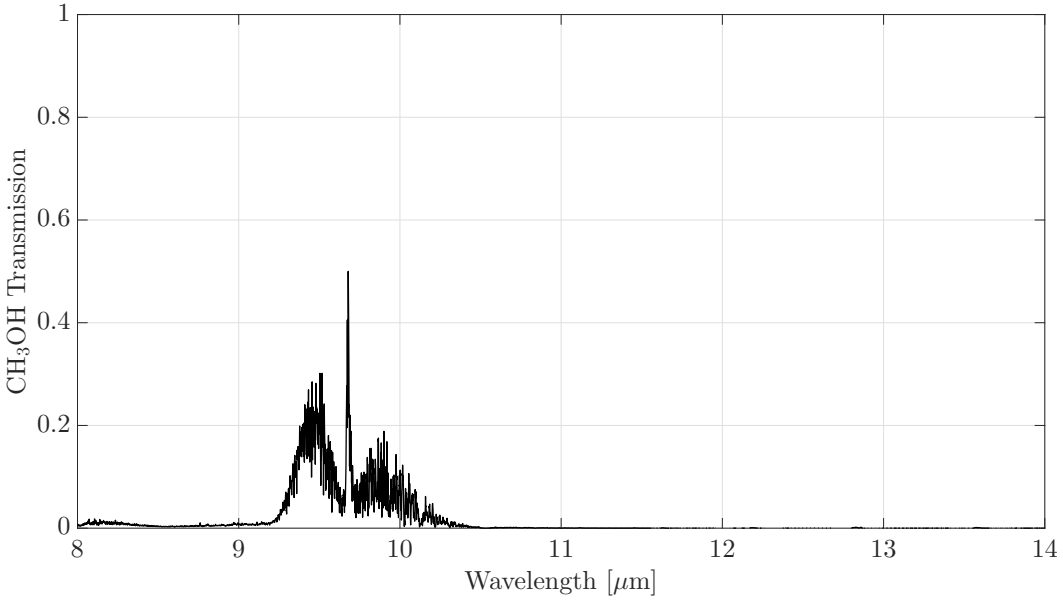

Figure 8.7: The effect of methanol emissions on plume transmission, shown as the difference between total plume transmission (with all UHCs included) and transmission without methanol included.

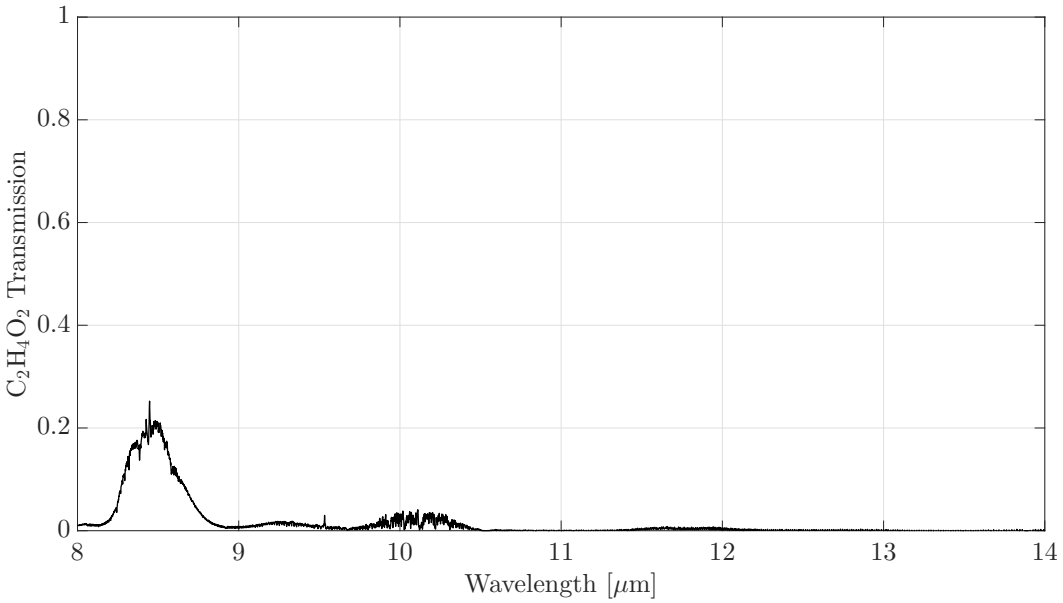

Figure 8.8: The effect of acetic acid emissions on plume transmission, shown as the difference between total plume transmission (with all UHCs included) and transmission without acetic acid included.

8.3 System Design Modifications

The discussion on future work concludes with suggestions for system design improvements. The current proposed model requires a reflection off of a zinc-coated plate, which is about 18"×12" in area. When tilted at 45°, the longer dimension has an effective length of 12.72", thus the 12" width is still the limiting factor for observations. Limiting the camera to observe the smaller dimension of 12", and considering the plate-to-camera distance of at least 60 [m] (assuming a plume at least 10 [m] in diameter), we determine that a camera must have a field-of-view (FOV) of 0.66°. There can be any number of pixels on the detector, but the spatial extent of observation will be limited by the plate. This limits our capability to study the spatial nature of the plume.

An operator will be required for initial testing and calibration of the camera system. This will likely require a stand-off distance of at least 50 [m] from the plume center, making the reflective plate a necessity to observe a sky background. However, if the system could be remotely operated, the camera could be placed on the ground directly at the edge of the runway, looking diagonally through the plume and to the sky. This would slightly modify the governing equation to

$$\begin{aligned} L_{sky}(\lambda) =& \tau_p \tau_{atm} \tau_{10} \tau_{50} B(T_b, \lambda) \\ &+ \tau_{50} B(T_p, \lambda)(1 - \tau_p), \end{aligned} \tag{8.4}$$

and allow for a much larger collection FOV. With this adjustment we can not only observe a single plane of emission at height $z = 0$, but a vertical swath of layers. This will provide much more detailed information regarding the plume spatial extent.

Chapter 9

Conclusions

A multispectral longwave infrared (LWIR) imaging system was proposed to detect and monitor the spatial and temporal extent of aircraft jet engine exhaust during the landing/takeoff (LTO) cycle. The system is inexpensive, portable, and unobtrusive to daily airport operations, allowing it to be deployed in a wide variety of settings.

Of the main pollutants emitted in jet engine exhaust, unburned hydrocarbons (UHCs) were targeted due to their prominence in the LWIR and the strength of their spectral absorption features. Other constituents, such as CO_x and NO_x, had few or no absorption features in the LWIR. As UHCs emissions are highest during the taxi/idle stage of an aircraft, the system is proposed to monitor aircraft along taxiways.

Two methods of modeling plume concentration were tested: the Ideal Gas Law and the Gaussian plume equation. As the Ideal Gas Law is used for closed systems (a criteria exhaust plumes do not meet), we concluded that the Gaussian plume equation provided a better portrayal of a jet engine exhaust plume. Previous studies were used to determine the UHC speciation, and 19 individual constituents were scaled to appropriate pollutant emission indices (EIs). The total sum of speciated UHC EIs was set to match the UHC EI of a typical Boeing 737 (B737) engine. The Gaussian plume model was modified to characterize UHC emissions as a function of time by insertion of a decaying Gaussian function (representing the temporal dispersion) on an integrated concentration plot (representing the plume of a moving aircraft).

The proposed system models the sky radiance reflecting off of a zinc-coated plate and through the exhaust plume, into the camera. Models were generated for three atmospheric transmission profiles (one atmospheric and two ground-based), and the reflectivity of the zinc-coated plate was measured in the laboratory. The plume transmission was modeled with the Gaussian concentration model and UHC absorption spectra from Pacific Northwest National Laboratory (PNNL).

The plume radiance was modeled at various downwind distances, or at certain time intervals. The difference between the expected plume and background radiance was used to select a combination of two filters that would best approximate the background radiance (where the difference was minimum) and best highlight the plume radiance (where the difference was maximized). Through this process two on-hand filters were selected with center wavelengths (CWLs) of 9.0001 [μm] (background) and 9.399 [μm] (plume tracer). Filters with ideal CWLs were also selected, located at 12.212 [μm] (background) and 9.776 [μm] (plume tracer).

Using the on-hand and ideal filter combinations, a baseline difference was determined for the system of 0.932 [W/m^{2}sr] and 0.907 [W/m^{2}sr], respectively. The difference in plume and background radiance for the plume tracing filters was used as a measure of plume detectability. Models suggest that the plume will be detectable up to 120 [s] after an engine has passed the imaging system, provided the camera has an noise equivalent change (delta) in temperature (NEΔT) of 0.05 [K] or less.

Temporal models were also generated to show the effect of multiple plumes being generated in the camera line-of-sight. If one plume does not have time to dissipate before another plane taxis by, subsequent plumes will further enhance the UHC concentration levels above the baseline. This effect is shown in the temporal models, but the exact taxiing frequency at which this occurs will be better defined with empirical observations.

Future work requires deploying this system for initial testing and improving uncertain parameters. The proposed system demands reflectance off of a zinc-coated plate. Once the system can be operated remotely, the entire spatial domain will become available for monitoring, as the camera can be placed right next to the runway at an angle that enables viewing the sky directly. In addition, more narrowband filter CWLs were highlighted that would be capable of monitoring individual UHC levels.

The unique speciation of UHCs will be better defined as a result of this work. Moreover, this work will enable airport officials to efficiently and inexpensively perform emissions inventories, and allow communities to better assess the local air quality.

Bibliography

[1] *Preliminary Study and Analysis of Toxic Air Pollutant Emissions from O'Hare International Airport and the Resulting Health Risks Created by these Toxic Emissions in Surrounding Communities*. Park Ridge, IL, Aug. 2008.

[2] N. S. Ahmed-Allah. "Study Says O'hare Emissions Hike Cancer Risks". *Chicago Tribune*. (Aug. 2000). online.

[3] *Chicago O'Hare Airport Air Toxic Monitoring Program*. Environmental Protection Agency, IL, 2000.

[4] M. Inman. "Plane Exhaust Kills More People Than Plane Crashes". *National Geographic*. (Oct. 2010). online.

[5] R. E. B. Steven R. H. Barrett and I. A. Waitz. "Global Mortality Attributable to Aircraft Cruise Emissions". *Environmental science & technology*. 44.19 (2010), pp. 7736–7742.

[6] D. Weikel and T. Barboza. "Planes' exhaust could be harming communities up to 10 miles from LAX". *LA Times*. (May 2014). online.

[7] N. Hudda, T. Gould, K. Hartin, T. V. Larson, and S. A. Fruin. "Emissions from an International Airport Increase Particle Number Concentrations 4-fold at 10 km Downwind". *Environmental science & technology*. 48.12 (2014), pp. 6628–6635.

[8] D. Abel and Z. T. Sampson. "Lung illnesses more likely near Logan Airport: Study doesn't find higher rates of heart disease, hearing loss". *Boston Globe*. (May 2014). online.

[9] M. D. of Public Health. *Logan Airport Health Study*. Tech. rep. Bureau of Environmental Health, May 2014.

[10] R. Mason. "Heathrow third runway decision put off until at least summer 2016". *The Guardian*. (Dec. 2015). online.

[11] P. Fonta. "Pushing the technology envelope". *BAN Ki-moon*. (2010).

[12] *Aviation & Emissions A Primer*. Federal Aviation Administration, 2005.

[13] *Aviation Emissions, Impacts & Mitigation: A Primer*. Federal Aviation Administration, Jan. 2015.

[14] *Air transport, passengers carried*. `http://data.worldbank.org/indicator/IS.AIR.PSGR/countries/1W?display=default`. ICAO, 2016.

[15] *Boeing Current Market Outlook 2008-2027*. Tech. rep. Chicago, IL: Boeing, 2008.

[16] *Aircraft technology improvements*. ICAO Secretariat, 2010.

[17] ICAO. *Airport Air Quality Manual*. 1st. Quebec, Canada, 2011.

[18] ICAO. *ICAO Annex 16: Environmental Protection, Volume II – Aircraft Engine Emissions*. Tech. rep. ICAO, 20108.

[19] *New ICAO Aircraft CO2 Standard One Step Closer To Final Adoption*. online. ICAO Newsroom, Feb. 2016.

[20] *ICAO Aircraft Engine Emissions Databank*. online. ICAO Committee on Aviation Environmental Protection, Jan. 2015.

[21] *New Emission Standards for New Commercial Aircraft Engines*. Office of Transportation and Air Quality, 2005.

[22] R. J. Heinsohn and R. L. Kabel. "Sources and control of air pollution: Engineering principles" (1998).

[23] A. Russell, J. Milford, M. Bergin, S. McBride, *et al.* "Urban ozone control and atmospheric reactivity of organic gases". *Science*. 269 (5223) (1995), p. 491.

[24] *What are Hazardous Air Pollutants?* US Environmental Protection Agency, 2015.

[25] *Home | IONICON Analytik - The World's Leading PTR-MS Company*. `http://www.ionicon.com/`. 2016.

[26] C. E. Kolb, J. McManus, D. D. Nelson, and M. S. Zahniser. "Tunable infrared laser differential absorption spectroscopy (TILDAS) monitors for atmospheric trace gases". In: *Lasers and Electro-Optics Society Annual Meeting, 1996. LEOS 96., IEEE*. Vol. 2. IEEE. 1996, 92–vol.

[27] *Infrared Cameras | OEM Thermal Camera Modules & Detectors | DRS Infrared*. `http://www.drsinfrared.com/`. 2014.

[28] *Infrared Cameras from FLIR*. `http://www.flir.com/instruments/display/?id=56784`. 2016.

[29] C. Spicer, M. Holdren, T. Lyon, and R. Riggin. *Composition and photochemical reactivity of turbine engine exhaust*. Tech. rep. DTIC Document, 1984.

[30] W. Knighton, S. Herndon, and R. Miake-Lye. "Aircraft engine speciated organic gases: Speciation of unburned organic gases in aircraft exhaust". *Environmental Protection Agency, Office of Transportation and Air Quality*. (2009).

[31] C. W. Spicer, M. Holdren, S. Miller, D. L. Smith, and R. N. Smith. *Aircraft Emissions Characterization: TF41-A2, TF30-P103, and TF30-P109 Engines*. Tech. rep. DTIC Document, 1987.

[32] C. Spicer, M. Holdren, S. Miller, D. Smith, R. Smith, and D. Hughes. *Aircraft Emissions Characterization*. Tech. rep. ESL-TR-87-63, Tyndall AFB, Florida, 1988.

[33] C. Spicer, M. Holdren, D. Smith, S. Miller, R. Smith, and D. Hughes. *Aircraft Emissions Characterization: F101 and FiIO Engines*. Tech. rep. ESL-TR-89-13, Tyndall AFB, Florida, 1989.

[34] C. W. Spicer, M. W. Holdren, D. L. Smith, D. P. Hughes, and M. D. Smith. "Chemical composition of exhaust from aircraft turbine engines". *Journal of Engineering for gas turbines and power*. 114 (1) (1992), pp. 111–117.

[35] C. Spicer, M. Holdren, R. Riggin, and T. Lyon. "Chemical composition and photochemical reactivity of exhaust from aircraft turbine engines". In: *Annales Geophysicae*. Vol. 12. 10-11. Springer. 1994, pp. 944–955.

[36] S. C. Herndon, T. Rogers, E. J. Dunlea, J. T. Jayne, R. Miake-Lye, and B. Knighton. "Hydrocarbon emissions from in-use commercial aircraft during airport operations". *Environmental science & technology*. 40 (14) (2006), pp. 4406–4413.

[37] G. McInnes. *Atmospheric Emission Inventory Guidebook: A Joint EMEP/CORINAIR Production*. EC, 1996.

[38] G. Schürmann, K. Schäfer, C. Jahn, H. Hoffmann, M. Bauerfeind, E. Fleuti, and B. Rappenglück. "The impact of NOx, CO and VOC emissions on the air quality of Zurich airport". *Atmospheric Environment*. 41 (1) (2007), pp. 103–118.

[39] H. Agrawal, A. A. Sawant, K. Jansen, J. W. Miller, and D. R. Cocker. "Characterization of chemical and particulate emissions from aircraft engines". *Atmospheric Environment*. 42 (18) (2008), pp. 4380–4392.

[40] S. C. Herndon, J. T. Jayne, P. Lobo, T. B. Onasch, G. Fleming, D. E. Hagen, P. D. Whitefield, and R. C. Miake-Lye. "Commercial aircraft engine emissions characterization of in-use aircraft at Hartsfield-Jackson Atlanta International Airport". *Environmental science & technology*. 42 (6) (2008), pp. 1877–1883.

[41] B. E. Anderson, G. Chen, and D. R. Blake. "Hydrocarbon emissions from a modern commercial airliner". *Atmospheric Environment*. 40 (19) (2006), pp. 3601–3612.

[42] J. Kinsey. *Characterization of Emissions from Commercial Aircraft Engines during the Aircraft Particle Emissions EXperiment (APEX) 1 to 3, EPA-600/R-09/130*. Tech. rep. Technical Report, 2009.

[43] P. E. Yelvington, S. C. Herndon, J. C. Wormhoudt, J. T. Jayne, R. C. Miake-Lye, W. B. Knighton, and C. Wey. "Chemical speciation of hydrocarbon emissions from a commercial aircraft engine". *Journal of Propulsion and Power*. 23 (5) (2007), pp. 912–918.

[44] W. B. Knighton, T. M. Rogers, B. E. Anderson, S. C. Herndon, P. E. Yelvington, and R. C. Miake-Lye. "Quantification of aircraft engine hydrocarbon emissions using proton transfer reaction mass spectrometry". *Journal of Propulsion and Power*. 23 (5) (2007), pp. 949–958.

[45] S. C. Herndon, E. C. Wood, M. J. Northway, R. Miake-Lye, L. Thornhill, A. Beyersdorf, B. E. Anderson, R. Dowlin, W. Dodds, and W. B. Knighton. "Aircraft hydrocarbon emissions at Oakland international airport". *Environmental science & technology*. 43 (6) (2009), pp. 1730–1736.

[46] E. Wood. *Aircraft and Airport-related Hazardous Air Pollutants: Research Needs and Analysis*. 7. Transportation Research Board, 2008.

[47] G. W. Santoni, B. H. Lee, E. C. Wood, S. C. Herndon, R. C. Miake-Lye, S. C. Wofsy, J. B. McManus, D. D. Nelson, and M. S. Zahniser. "Aircraft emissions of methane and nitrous oxide during the alternative aviation fuel experiment". *Environmental science & technology*. 45 (16) (2011), pp. 7075–7082.

[48] J. Cain, M. J. DeWitt, D. Blunck, E. Corporan, R. Striebich, D. Anneken, C. Klingshirn, W. Roquemore, and R. Vander Wal. "Characterization of gaseous and particulate emissions from a turboshaft

engine burning conventional, alternative, and surrogate fuels". *Energy & Fuels*. 27 (4) (2013), pp. 2290–2302.

[49] *Improving Plant Safety through IR Gas Cloud Imaging*. General Monitors.

[50] M. Kastek, T. Sosnowski, T. Piątkowski, and H. Polakowski. "Methane detection in far infrared using multispectral IR camera". In: *9th International Conference on Quantitative Infrared Thermography, Krakow, Poland*. 2008, pp. 1–4.

[51] M. Kastek, T. Sosnowski, T. Orżanowski, K. Kopczyński, and M. Kwaśny. "Multispectral gas detection method". *WIT Transactions on Ecology and the Environment*. 123 (2009), pp. 227–236.

[52] M. T. Eismann. *Hyperspectral remote sensing*. SPIE Bellingham, 2012.

[53] J. R. Schott. *Remote sensing*. Oxford University Press, 2007.

[54] S. W. Sharpe, R. L. Sams, T. J. Johnson, P. M. Chu, G. C. Rhoderick, and F. R. Guenther. "Creation of 0.10-cm-1 resolution quantitative infrared spectral libraries for gas samples". In: *Environmental and Industrial Sensing*. International Society for Optics and Photonics. 2002, pp. 12–24.

[55] L. S. Rothman, I. E. Gordon, Y. Babikov, A. Barbe, D. C. Benner, P. F. Bernath, M. Birk, L. Bizzocchi, V. Boudon, L. R. Brown, *et al.* "The HITRAN2012 molecular spectroscopic database". *Journal of Quantitative Spectroscopy and Radiative Transfer*. 130 (2013), pp. 4–50.

[56] P. Chu, F. Guenther, G. Rhoderick, and W. Lafferty. "The NIST quantitative infrared database". *Journal of research of the National Institute of Standards and Technology*. 104 (1) (1999), p. 59.

[57] J. D. Mattingly. *Aircraft engine design*. Aiaa, 2002.

[58] Boeing. *737 Airplane Characteristics for Airport Planning*. Tech. rep. Seattle, WA: Boeing, 2013, pp. 414–415.

[59] J. H. Seinfeld and S. N. Pandis. *Atmospheric chemistry and physics: from air pollution to climate change*. John Wiley & Sons, 2012.

[60] J. M. Stockie. "The mathematics of atmospheric dispersion modeling". *Siam Review*. 53 (2) (2011), pp. 349–372.

[61] D. Turner. *Workbook of Atmospheric Diffusion Estimates*. U.S. Environmental Protection Agency, 1969.

[62] D. O. Martin. "Comment On" The Change of Concentration Standard Deviations with Distance"". *Journal of the air pollution control association*. 26 (2) (1976), pp. 145–147.

[63] S. R. Hanna, G. Briggs, J. Deardorff, B. Egan, F. Gifford, and F. Pasquill. *AMS workshop on stability classification schemes and sigma curves-summary of recommendations*. 1977.

[64] W. Klug. "A method for determining diffusion conditions from synoptic observations". *Staub-Reinhalt. Luft*. 29 (4) (1969), pp. 14–20.

[65] F. Pasquill. "The estimation of the dispersion of windborne material". *Meteorol. Mag*. 90 (1063) (1961), pp. 33–49.

[66] C. Wey, B. Anderson, C. Hudgins, C. Wey, X. Li-Jones, E. Winstead, L. Thornhill, P. Lobo, D. Hagen, and P. Whitefield. "Aircraft particle emissions experiment (APEX)" (2006).

[67] T. Gibbs. personal communication. Nov. 1, 2016.

[68] A. Berk, P. Conforti, R. Kennett, T. Perkins, F. Hawes, and J. van den Bosch. "MODTRAN6: a major upgrade of the MODTRAN radiative transfer code". In: *SPIE Defense+ Security*. International Society for Optics and Photonics. 2014, 90880H–90880H.

[69] *About MODTRAN®*. `http://modtran.spectral.com/modtran_about`. 2016.

[70] D. H. Titterton. *Military laser technology and systems*. Artech House, 2015.

[71] *Tau® 2 Uncooled Cores*. `http://www.flir.com/cores/display/?id=54717`. 2016.